SANDIA REPORT
SAND2010-4633
Unlimited Release
Printed July 2010

Measurement and interpretation of threshold stress intensity factors for steels in high-pressure hydrogen gas

Kevin A. Nibur
Brian P. Somerday
Chris San Marchi
James W. Foulk, III
Mohsen Dadfarnia
Petros Sofronis
Gary A. Hayden

Prepared by
Sandia National Laboratories
Albuquerque, New Mexico 87185 and Livermore, California 94550

Sandia National Laboratories is a multi-program laboratory managed and operated by Sandia Corporation, a wholly owned subsidiary of Lockheed Martin Corporation, for the U.S. Department of Energy's National Nuclear Security Administration under contract DE-AC04-94AL85000.

Issued by Sandia National Laboratories, operated for the United States Department of Energy by Sandia Corporation.

Available to DOE and DOE contractors from
U.S. Department of Energy
Office of Scientific and Technical Information
P.O. Box 62
Oak Ridge, TN 37831

Telephone: (865) 576-8401
Facsimile: (865) 576-5728
E-Mail: reports@adonis.osti.gov
Online ordering: http://www.osti.gov/bridge

Available to the public from
U.S. Department of Commerce
National Technical Information Service
5285 Port Royal Rd.
Springfield, VA 22161

Telephone: (800) 553-6847
Facsimile: (703) 605-6900
E-Mail: orders@ntis.fedworld.gov
Online order: http://www.ntis.gov/help/ordermethods.asp?loc=7-4-0#online

SAND2010-4633
Unlimited Release
Printed July 2010

Measurement and interpretation of threshold stress intensity factors for steels in high-pressure hydrogen gas

Kevin A. Nibur, Brian P. Somerday, Chris San Marchi
Hydrogen and Metallurgy Science Department
James W. Foulk, III
Mechanics of Materials Department
Sandia National Laboratories
P.O. Box 969
Livermore, California 94551

Mohsen Dadfarnia, Petros Sofronis
Department of Mechanical Science and Engineering
University of Illinois at Urbana-Champaign
1206 West Green St., Urbana, Illinois 61801

Gary A. Hayden, PE
Chief Metallurgist and Director – Quality Assurance
CP Industries
2214 Walnut St., McKeesport, Pennsylvania 15132-7098

Abstract

Threshold stress intensity factors were measured in high-pressure hydrogen gas for a variety of low alloy ferritic steels using both constant crack opening displacement and rising crack opening displacement procedures. The sustained load cracking procedures are generally consistent with those in ASME Article KD-10 of Section VIII Division 3 of the Boiler and Pressure Vessel Code, which was recently published to guide design of high-pressure hydrogen vessels. Three definitions of threshold were established for the two test methods: K_{THi}^{*} is the maximum applied stress intensity factor for which no crack extension was observed under constant displacement;

K_{THa} is the stress intensity factor at the arrest position for a crack that extended under constant displacement; and K_{JH} is the stress intensity factor at the onset of crack extension under rising displacement. The apparent crack initiation threshold under constant displacement, K_{THi}*, and the crack arrest threshold, K_{THa}, were both found to be non-conservative due to the hydrogen exposure and crack-tip deformation histories associated with typical procedures for sustained-load cracking tests under constant displacement. In contrast, K_{JH}, which is measured under concurrent rising displacement and hydrogen gas exposure, provides a more conservative hydrogen-assisted fracture threshold that is relevant to structural components in which sub-critical crack extension is driven by internal hydrogen gas pressure.

ACKNOWLEDGMENTS

Sandia National Laboratories is a multi-program laboratory managed and operated by Sandia Corporation, a wholly owned subsidiary of Lockheed Martin Corporation, for the U.S. Department of Energy's National Nuclear Security Administration under contract DE-AC04-94AL85000. The work presented in this report has been funded by the US DOE Fuel Cells Technology program through the Safety, Codes and Standards program element. The assistance of Ken Lee and Jeff Campbell in the experimental work as well as Andy Gardea, Jeff Chames and Ryan Nishimoto in metallography and microscopy is gratefully acknowledged.

THIS PAGE INTENTIONALLY LEFT BLANK

CONTENTS

LIST OF TABLES

LIST OF FIGURES

NOMENCLATURE

J_i	Elastic-plastic J-Integral value at precise point of crack initiation; subscript H refers to measurements in hydrogen gas
J_{Ic}	Elastic-plastic J-Integral value for crack initiation defined at the intersection of the J versus crack extension curve and the 0.2mm offset blunting line; subscript H refers to measurements in hydrogen gas
K_{app}	Stress intensity factor applied to the fixed displacement WOL specimen
K_{Ic}	Critical linear-elastic plane-strain stress intensity factor measured in a inert or non-embrittling environment
K_{JH}	Crack initiation toughness determined from rising-displacement elastic-plastic fracture mechanics experiments
K_R	Crack growth resistance, defined as the remotely measured stress intensity factor required for crack extension
K_{TH}	Threshold stress intensity factor for hydrogen assisted cracking
K_{THa}	Threshold stress intensity factor for crack arrest at fixed displacement
K_{THi}^*	Apparent threshold stress intensity factor for crack initiation at fixed displacement
r_p	Crack tip plastic zone radius
WOL	Wedge Opening Loading bolt loaded compact fracture mechanics specimen
ε^*	critical fracture strain
ε^*_H	critical fracture strain for hydrogen assisted cracking

THIS PAGE INTENTIONALLY LEFT BLANK

1 INTRODUCTION

Implementation of a fracture mechanics-based design approach for hydrogen containment and transport components could greatly reduce concerns about catastrophic failures due to sub-critical crack propagation. Hydrogen reduces the cracking resistance of most metal alloys, as documented over many decades, e.g. [1,2,3,4,5,6,7,8]. Reliable and conservative methods for measuring fracture thresholds in high pressure hydrogen gas are necessary to ensure effective fracture mechanics based component design. As the range of applications and performance requirements for high-pressure hydrogen containment structures expands beyond the current technology space, fracture mechanics design approaches become increasingly important to ensure the safety of hydrogen containment structures.

Laboratory test methods for measuring fracture thresholds in hydrogen gas must properly simulate the mechanical and environmental conditions of actual service components, i.e., the concept of similitude must be considered for both the mechanical and environmental conditions at the crack tip. The mechanical conditions around a crack-like flaw in a structure pressurized by hydrogen are no different than they would be in another environment. Therefore, established fracture mechanics methods designed to measure either the linear-elastic stress intensity factor, K, or the elastic-plastic J-integral, J, can be directly applied in a hydrogen environment. Achieving the second condition, that of environmental similitude, adds complexity to the problem. Convincing evidence does not yet exist that environmental similitude under high pressure hydrogen uptake can be accurately reproduced in ferritic steels by means such as thermal precharging in hydrogen gas or any electrochemical method. Thus, the most consistent method to assure environmental similitude is to replicate the conditions of the intended service environment by conducting tests in high pressure gaseous hydrogen.

Establishing environmental similitude between a test specimen and a component involves more than just considering hydrogen gas pressure. The uptake of hydrogen into the metal may be affected by variables such as gas purity, specimen surface cleanliness, and specimen loading rate and loading history. Additionally, oxide films on the metal surface may impede the dissociation and adsorption of hydrogen at the metal surface [7]. As little as 100 vppm (parts per million by volume) oxygen mixed with 7 MPa hydrogen gas has been shown to eliminate effects of hydrogen on fatigue crack growth of X42 linepipe steel [9] and 0.7 volume % oxygen added

to hydrogen gas at atmospheric pressure was sufficient to halt sustained load cracking in a high strength tool steel [10]. Similar results have also been demonstrated for impurities of CO and SO_2 in hydrogen gas [9]. Since the benefit of such impurities has not yet been demonstrated over the full service life of a structure and because many applications will not tolerate such impurities, gaseous impurities in the hydrogen have been kept as low as possible in this study. This also yields conservative measurements.

Hydrogen-assisted cracking is a form of environment-assisted cracking (EAC). EAC broadly refers to any interaction between a metal and the external environment which facilitates crack extension at stress intensity factors less than K_{Ic}, the critical stress intensity factor at which a crack will extend in normal conditions. Due to the kinetic nature of the reactions that must occur between the metal and the environment, all forms of EAC are limited by the reaction kinetics and EAC is therefore sensitive to kinetic factors, such as the applied loading rate. If the rate at which load is applied to the specimen is such that the crack is driven faster than the kinetics of hydrogen uptake and transport from the external environment to the crack tip process zone, the effect of hydrogen on crack growth will be diminished. For this reason, many of the test methods that have been developed for measuring environment-assisted cracking thresholds, K_{IEAC}, employ constant load or constant displacement, such as those outlined in ASTM Standard E1681 [11].

The wedge opening load (WOL) specimen is a compact geometry described in ASTM E1681 that is well suited for constant displacement EAC tests and is the geometry that was used in this study for constant displacement tests. It can be self-loaded by tightening a bolt which is threaded through the top of the specimen and reacts against a load pin in the bottom of the specimen. Following procedures similar to those outlined in E1681, this specimen has been used to assess hydrogen-assisted fracture by measuring the stress intensity factor at crack arrest, K_{THa}, in iron-nickel alloys and austenitic stainless steel [12], and ferritic steels [13]. This test method has been incorporated into ASME's hydrogen specific design code for pressure vessels, Article KD-10 "Special requirements for vessels in high pressure gaseous hydrogen transport and storage service" which was approved for inclusion into Section VIII Division 3 of the Boiler and Pressure Vessel Code in 2006 [14,15].

The resistance to hydrogen assisted fracture can also be evaluated using rising-load experimental methods such as those conventionally used for fracture toughness measurements. A study by Clark and Landes compared the results of fixed-displacement and rising-load testing

methods using high-strength (1100-1240 MPa yield strength) 4340 steel [16]. A strong dependency on loading rate was observed in the rising-load experiments in hydrogen gas; fracture thresholds increased as loading rate increased. As loading rate was decreased to very slow rates, the measured fracture thresholds approached the value measured from the fixed-displacement tests suggesting that the fixed displacement test provided a conservative measurement for the high-strength steels employed in that study.

Gangloff subsequently published data taken from multiple sources and showed that, for lower strength steels, threshold values measured under constant displacement were as much as four times larger than those measured under rising load conditions [1]. The difference diminished as the strength increased up to about 1000 MPa, at which point results from the two test methods converged. Although the data were compiled from different studies, the same alloy was used and the starting hydrogen concentrations were similar. The specimens were precharged with hydrogen, however, and tested in air. It is expected that the actual hydrogen concentration in the static loaded specimens was less than that in the rising load specimens due to the much longer duration of the test and the propensity for hydrogen to off-gas from ferritic steels. Nonetheless, the data demonstrate a potentially important difference between static and dynamic loading conditions that indicated a need for further study.

The objective of this study is to measure a set of benchmark hydrogen-assisted fracture thresholds, K_{TH}, in 103 MPa hydrogen gas for a variety of steels focusing on the lower strength levels that are technologically relevant to hydrogen storage and delivery components. Steels with ultimate tensile strengths less than 950 MPa are of particular interest since higher strength steels are generally considered inappropriate for high-pressure gaseous hydrogen service [17]. The effects of initial stress intensity factor, loading environment, and loading method (constant displacement versus rising displacement) are explored. Various methods of defining K_{TH} are explored including crack initiation and crack arrest threshold from constant displacement tests as well as crack initiation threshold from rising displacement tests.

2 EXPERIMENTAL PROCEDURES

2.1 Steels tested

A range of Cr-Mo and Ni-Cr-Mo steels were acquired for testing consisting of seven commercially produced low-alloy pressure vessel steels. In addition, an ultra-high purity laboratory heat of HY130 steel was tested with three different heat treatments: as quenched with no temper, tempered at 200°C and tempered at 400°C. This last steel has been the subject of much prior research (e.g. [18]). The alloy composition, yield strength (S_y), and tensile strength (S_u) for each steel are summarized in Table 1 and Table 2.

The commercially produced low alloy pressure vessel steels each conform to one of four different specifications: DOT-3AAX (4130X), DOT-3T, SA372 grade J and SA372 grade L. The first three are Cr-Mo steels comparable to AISI 41xx grades and the SA372 grade L is a Ni-Cr-Mo steel comparable to AISI 4340. These pressure vessel steels were acquired as curved panels cut from seamless pipe test-rings, which are heat treated alongside commercial pressure vessels, and thus receive identical processing. The heat treatment of the steel test-rings followed a proprietary commercial sequence consisting of austenitizing, one-sided quenching, and tempering to achieve the desired strength. The yield and tensile strengths shown in Table 1 and Table 2 were reported by the manufacturer. Two fracture toughness specimens machined from the DOT-3T (a heat later refered to in this report as heat B) were tested in laboratory air following similar procedures to those described in Section 2.3. The elastic-plastic fracture toughness of this alloy, J_{Ic}, was approximately 120 kJ/m^2 (K_J = 165 MPa m$^{1/2}$). The other alloys in this study are expected to have comparable (or perhaps greater) values of fracture toughness. Five different heats of SA372 grade J and two different heats each of SA372 grade L, DOT-3T and DOT-3AAX were tested with variations in chemistry and/or strength. The tempered microstructures contain varying amounts of ferrite, bainite and tempered martensite. Representative microstructures of the various pressure vessel steels are shown in Figure 1.

2.2 Sustained load cracking tests

2.2.1 Threshold stress intensity factor measurements

Specimens for fixed-displacement, sustained load cracking experiments were machined in accordance with ASTM E1681-03 and the bolt loaded compact WOL geometry, shown in Figure

2. For the steels acquired from tubular products, the crack plane was normal to the circumferential direction and crack propagation was parallel to the longitudinal direction. All of the pressure vessel steel specimens had the same in-plane geometry with width, W, equal to 56.9 mm, however the thickness was determined by the wall thickness of the as-received product. Due to size limitation of the as-received material, both specimens machined from HY130 tempered at 200°C were machined such that the W dimension was 43 mm and all other in-plane dimensions scaled accordingly. The SA372 grade J and grade L products had a nominal outer diameter of 510 mm and nominal wall thickness of 38 mm which was sufficient to remove 22.2 mm thick specimens from the mid-radius position of the tube wall. The DOT-3AAX and DOT-3T steels had nominal wall thicknesses of approximately 17 and 14 mm respectively. For these steels, the full wall thickness was utilized for the specimen such that the specimen sides were curved. The degree of curvature in the specimen varies with the respective diameter of the tubular product, e.g., the outer diameter was approximately 560 mm for the DOT-3T and 630 mm for the DOT-3AAX. Side grooves were machined along the broad faces of the WOL specimens prior to pre-cracking which combined for a total depth of 16% of the specimen thickness, B. Specimens were cleaned using a sequence of degreaser and isopropyl alcohol to remove machining oils, and subsequent handling of specimens was done with care (e.g., personnel used rubber gloves) to prevent contamination.

Pre-cracking was accomplished via cyclic loading in air using a servo-hydraulic load frame to create starting crack lengths of 0.55 W at a final stress intensity factor of 27 MPa $m^{1/2}$, which resulted in approximately 3 mm of fatigue crack growth from the starter notch. Specimens were mounted into the load frame such that the top of the specimen was connected to a universal joint via a rigid, threaded stud and the bottom of the specimen was pinned to a clevis, which in turn was connected to a second universal joint (Figure 3). Upon completion of pre-cracking, the final compliance of each specimen was recorded and the specimen was then placed into a glovebox filled with approximately 0.1 MPa purified argon containing oxygen and moisture levels controlled to below 2 vppm O_2 and 8 vppm H_2O to minimize further formation of surface oxide at the crack tip.

The crack opening displacement was applied to the pre-cracked specimens inside the glovebox (Figure 4) using either A-286 stainless steel bolts or Cu-Be bolts reacting against Cu-Be load tups. The load tups were instrumented with strain gages and act as load sensors (Figure

5). Crack opening displacement was monitored during loading of the bolts using a clip gauge on the front face. This displacement measurement and the expected compliance of the specimen was used to determine the actual load applied to the specimen since this method proved more consistently accurate than estimating load from the output of the load tup.* The load tups did, however, provide a very sensitive means for detecting crack initiation and arrest and were used for calculations of crack growth velocity.

These sustained load fracture mechanics experiments differ from rising load tests in that a displacement is initially applied to the specimen and then held constant throughout the duration of the test. It must also be noted that the fixed displacement is applied prior to hydrogen gas exposure. Once the fixed-displacement specimen is exposed to hydrogen gas, time-dependent hydrogen uptake reduces the fracture resistance and causes the crack to grow. The stress intensity factor, K, continuously decreases as the crack extends until the crack arrests at the threshold stress intensity factor, K_{THa}.

The load applied to each specimen correlates to an initial stress intensity factor, K_{app}. While K_{app} must be greater than K_{THa}, it must not be so great that the crack extends through the entire width of the specimen during testing in hydrogen gas. Once an initial value of K_{THa} was measured for a steel, K_{app} and the associated loads on subsequent specimens were selected in an attempt to have a range of final crack lengths at crack arrest.

The bolt-loaded specimens were placed into a pressure vessel and the vessel was sealed while still inside the glovebox. The pressure vessel was then removed from the glovebox, placed inside of a secondary containment vessel, and connected to the gas distribution manifold. All manifold tubing leading up to the pressure vessel valve was purged using three consecutive sequences of vacuum followed by backfilling with 21 MPa helium gas and then an additional three consecutive sequences of vacuum followed by backfilling with 21 MPa hydrogen gas. Immediately following these purging cycles on the manifold, the pressure vessel valve was opened and the residual argon was removed using vacuum. 99.9999% pure hydrogen gas was used for manifold purging as well as for the final fill to the test pressure, which varied from 41 to 138 MPa. Signals from the load tups were recorded continuously via electrical feed-throughs in

* Anomalous, non-linear trends were sometimes observed in the response signals from these load tups during load application, particularly when smaller diameter loading bolts (necessary for the thinner specimens) were used. These anomalies are believed to result from the mixed mode (normal and rotational) displacement imparted to the load tup from the rotating bolt as the crack opens. When calibrated in a load frame using purely normal force, the output of the load tup was quite linear and repeatable.

the pressure vessel. The pressure vessels and load tups are the same hardware as reported in ref.[12].

A predictable fluctuation of the load cell signal occurred upon exposure of the strain gages to hydrogen gas. The fluctuation occurred slowly from strain gages which had not been previously used in hydrogen and would reach a steady value after a period of several hours to as long as one day. Strain gages which had been previously exposed to hydrogen exhibited a shift in output signal as well, however the change in signal coincided with the changing hydrogen pressure. Very little further change in the signal occurred once the final hydrogen pressure was reached. In both cases, once the load cell signal stabilized, it remained constant until the hydrogen gas pressure was removed or a specimen cracked.

After the pressure vessels were filled with hydrogen gas to the test pressure, crack propagation was detected as a drop in the measured load from the instrumented load tups. The incubation time, i.e., the duration of hydrogen gas exposure prior to the onset of crack growth, varied greatly among specimens, as will be discussed further in the sections 3 and 4. As such, some pressure vessels were vented and specimens removed after extended times ranging from 170 hours to more than 3800 hours. Some specimens did not exhibit crack extension in hydrogen gas; many of these were removed from the pressure vessel while inside the glovebox, reloaded to higher K_{app} values, then retested in hydrogen gas.

At the completion of each test, hydrogen was vented from the pressure vessel. Gas samples were collected at the end of selected tests and sent to a commercial laboratory for compositional analysis. In total, gas was sampled from 8 pressure vessels, each of which contained up to eight WOL specimens. The results from these eight samples found water vapor was typically 0.5 to 0.8 vppm (one vessel containing DOT-3T at 41 MPa H_2 had 1.4 vppm water vapor), oxygen was always less than 0.5 vppm and CO_2 was always less than 0.6 vppm. Hydrocarbons, CO, or NO were less than the detection limit of 0.1 vppm. Up to 5 vppm nitrogen and 18 vppm argon were detected; high argon levels were expected since the vessels were initially filled with argon while in the glovebox. Due to the consistency of these results and the purging procedures used, the gas was not sampled from all tests.

Specimens that exhibited hydrogen-assisted fracture were heat tinted for 20 minutes at 280^{o}C to mark the extent of crack propagation and then broken apart. Pre-crack and final crack lengths were measured from digital images using the procedure outlined in ASTM E1820 [19]. The

standard procedure for measurement of crack length given in ASTM E1681 recommends an average of five measurements across the crack front whereas that in ASTM E1820 recommends an average of nine measurements. Fracture surfaces were examined using standard electron microscopy techniques.

2.2.2 Threshold stress intensity factor calculation method

The stress intensity factor, K, for the WOL specimen was calculated using the relationship in ASTM E1681, where K is a function of the initial front face crack opening displacement, V_{FF}, specimen width, W, elastic modulus, E' (207 GPa was used for all steels), and crack length-to-width ratio, a/W:

$$K = \left[V_{FF} E' / W^{1/2}\right]\left[1 - a/W\right]^{1/2} f(a/W)$$
$$f(a/W) = 0.654 - 1.88(a/W) + 2.66(a/W)^2 - 1.233(a/W)^3 \qquad (1)$$

This relationship is considered to be valid for all a/W from 0.3 to 1 [11].† The initial applied stress intensity factor, K_{app}, and the crack arrest threshold stress intensity factor, K_{THa}, were calculated using equation (1) and the physically measured values of the pre-crack and final crack length, respectively. The applied front face displacement during bolt loading, V_{FF}, was used in the calculations for both K_{app} and K_{THa}.

The form of equation (1) is such that K is independent of the specimen thickness; however, some consideration of thickness is necessary to account for the side grooves. In a report summarizing the WOL specimen, James [20] suggests two relationships for calculating effective thickness, B_{eff}, which account for side grooves and are a function of the gross thickness, B, and the net thickness, B_n, (between the side grooves). The first relationship,

$$B_{eff\,K} = \left(B\, B_n\right)^{1/2} \qquad (2)$$

† For all of the relationships in this report describing the specimen response to far-field loads or displacement (i.e. formula for K and compliance), E' is assumed to be equal to the plane stress elastic modulus, E. As described in Appendix A, this assumption provides a better correlation with actual specimen behavior relative to use of the plane strain elastic modulus, $E/(1-\nu^2)$, but has no relationship to local conditions at the crack tip.

was first proposed by Freed and Krafft [21] and is suggested by James for use when calculating K. The second relationship,

$$B_{eff_C} = B/\left[2.48 - 2.89(B_n/B) + 1.41(B_n/B)^2\right] \quad (3)$$

was proposed by Neale et al [22], and is recommended by James for use when calculating compliance.

Equation (1) was developed by combining relationships for the stress-intensity factor and for compliance, which were dependant on load, crack-length and thickness, into a solution which is independent of thickness and dependant only on crack opening displacement and crack-length. In order to account for the effect of the side-grooves, a correction factor for equation (1) was determined using the two relationships for B_{eff} in equations (2) and (3). The rationale for this correction factor is as follows. K is directly proportional to the applied load, thus $K \propto P/B$ where P is the load and B, in the case of a side grooved specimen, is replaced by B_{eff_K}. Since this specimen is assumed to be linear elastic, the load required to achieve a given displacement, V_{FF}, must be proportional to the effective specimen thickness, B_{eff_C}, thus $P \propto B_{eff_C}$. Combining these proportionalities, it follows that $K \propto B_{eff_C}/B_{eff_K}$. For this study, equation (1) was multiplied by a correction factor of B_{eff_C}/B_{eff_K} to account for the side grooves. The result for 16% side grooves is that K increases by about 4% relative to the value determined if the side grooves are ignored.

The effects of the curved side faces of the DOT-3T and -3AAX WOL specimens were ignored for all calculations of K and compliance. A method for correcting the K solution of a curved double cantilever beam (DCB) specimen is provided in ANSI/NACE Standard TM0177-96 [23]. While this correction factor is intended for the DCB specimen, the solution is quite generic and can be applied to the different aspect ratio of the WOL specimen and should provide at least an estimate of the effect of side-face curvature for the WOL specimen. The NACE standard correction suggests that the true K value would be increased, due to the curvature, by 0.16% for the geometry of the DOT-3T specimens and by 0.12% for the 3AAX specimens. This correction is sufficiently small to justify the omission of a correction for curvature.

2.2.3 Crack growth rate measurement

The use of individual load cells in the WOL specimens allowed for quantifying the crack growth rate in addition to detecting the onset and arrest of crack growth. ASTM E 1681 Annex A1 outlines the method for determination of the crack velocity (da/dt) and was used as general guidance for the data analysis presented here. Despite careful calibration of each individual load cell in air, the output values fluctuate upon exposure to hydrogen gas. The strain gauge output exhibits time dependant variability with hydrogen gas pressure at the commencement of testing, which settles to a constant value after a period of several hours. During calibration in air, it was noted that the output from the load cells was linear. Although hydrogen did cause an offset in the load tup signal, the linearity of the gage was assumed to be unaffected by hydrogen gas, so a *post-facto* calibration was used rather than the initial calibration generated in air.‡ The initial applied load and the final load, after crack arrest, were determined using the initial and final measured crack lengths, respectively, and the compliance relationship for the modified WOL specimen (equation 4, below). The initial and final loads were then associated with the maximum and minimum values of the load cell output and all intermediate loads were calculated assuming linear load cell output.

Once the applied loads were calculated from the load cell voltage, crack lengths were inferred from these applied loads using the compliance relationship. The relationship between crack length and load (at fixed V_{FF}) provided in ASTM E1681 was found to be inaccurate based on physical measurements of the pre-crack length. The error was typically in the range of 6-8 mm, an error of 25% or greater. The relationship provided by Lisagor [24] and summarized by James [20] was found to be more accurate. As published by James the relationship is

$$\frac{BE'V_{FF}}{P} = \exp(1.830 + 4.307(a/W) + 5.871(a/W)^2 - 17.53(a/W)^3 + 14.57(a/W)^4) \qquad (4)$$

where P is the applied load. Refitting this relationship to the form used in ASTM E 1681, a/W can be expressed as a function of load:

$$a/W = 1.0827 - 8.9294Z + 101.1864Z^2 - 886.7455Z^3 + 2799.366Z^4 \qquad (5)$$

‡ Although non-linear anomalies in the load tup signal were observed while applying the initial crack opening due to rotation of the bolt, unloading during crack growth should impart only a normal force change on the load tup since the opening displacement is fixed. Consequently, the load tup signal change associated with crack growth is assumed to be linear with the change in load.

$$Z=1/(V_{FF}E'B/P)^{1/2}$$

For side grooved specimens, as were used in this study, B was replaced with the effective thickness, B_{eff_C}, given in equation (3). Use of equation (5), when the load is determined using equation (4) is somewhat of a circular calculation which forces agreement between the calculated final crack length and the physically measured value. Since the load cell output was calibrated to match the physical measurements of the initial and final crack-lengths, equation (5) was used in this study only for the purpose of tracking the progression of the crack with time rather than as a quantitative measurement of crack-length from the load cell outputs. Any remaining discrepancy between the measured and calculated crack lengths (as a result of small fitting errors, rounding, etc) were then adjusted so that the endpoints exactly matched the physically measured initial and final crack lengths by applying a linear correction factor.

The crack velocity is often relatively large immediately following the onset of crack propagation, with gradual deceleration leading to eventual crack arrest (e.g. Figure 6); additionally, crack velocity is typically greater for the higher strength materials. In order to capture all of the kinetics of this process, data acquisition rates as fast as one data point every five seconds were needed. This resulted in large and cumbersome data files for typical test durations of hundreds of hours. Polynomial curve fitting methods which maintained the integrity of the data during the fast crack growth region were not effective in diminishing the pronounced noise in the data during the slow crack velocity region. To solve this problem, the crack length vs. time data were selectively thinned such that all data points during the fast velocity region were retained while data were increasingly thinned as the crack decelerated. In some cases, when the crack velocity was very low, as few as 1 data point per 100 was retained. A point to point secant method was used to calculate crack velocity, da/dt, in which the change in crack length was divided by the change in time between successive data points.

2.2.4 Chevron notched specimens

Additional specimens were machined from DOT-3AAX (607 MPa), DOT-3T (900 MPa A) and one heat of SA372 grade J (736 MPa) which were modified to replace the standard straight-through crack starter notch with a chevron notch. SA372 grade J specimens were first machined with a chevron notch having an included angle of about 45 degrees. This chevron notch

geometry was subsequently modified before machining specimens from the DOT-3T and -3AAX such that the chevron included angle was approximately 30 degrees. The chevron notch geometry used for each of these materials is shown in Figure 2.

The initial stress intensity factor, K_{app}, was calculated for these chevron notch specimens in the same manner as the straight-notch specimens (i.e. equation 1 in which no correction was added to account for the chevron notch). This assumption would not be valid if K were calculated based on applied load, however all K values were calculated directly from the crack mouth opening displacement. Nonetheless, it is expected that the actual stress intensity factor near the tip of the chevron notch may be amplified by the geometry. Values of K_{app} presented here may under-predict actual crack tip stress fields at the beginning of the test, however the values of K_{THa} are directly comparable with the straight notch specimens since the cracks arrested beyond the chevron notch region of the specimen.

2.3 Rising displacement threshold stress intensity factor measurements

Compact tension (CT) specimens for rising displacement fracture mechanics experiments were designed according to ASTM Standard E1737-96 [25]. Conventional rectilinear specimens were extracted from the mid-plane of panels of DOT-3T (900 MPa A), DOT-3AAX (607 MPa), SA372 grade J (641, 730, 736 and 783 MPa) and SA372 grade L (1053 MPa). Each specimen had a gross thickness, B, of 12.7 mm and a width, W, of 26 mm (Figure 2). Sidegrooves were machined along the faces of the specimens in the same plane as the pre-crack starter notch, which reduced the specimen thickness in this plane by 25%. Pre-cracking was performed in laboratory air at 10 Hz and an R-ratio (K_{min}/K_{max}) of 0.1. A K-shedding routine was used in which final K_{max} values equaled 20 MPa $m^{1/2}$ for all specimens except the DOT-3T and the high strength SA372 grade L in which final K_{max} values equaled 15 MPa $m^{1/2}$ and 10 MPa $m^{1/2}$ respectively. Final pre-crack lengths varied from 0.58W to 0.65 W.

Specimens were tested inside a custom designed pressure vessel which is mounted in the load train of a commercial servo-hydraulic test frame. A purging procedure of three pressurization and venting cycles with helium to 21 MPa followed by three more cycles using hydrogen to 21 MPa was used to remove impurity gases from the pressure vessel and gas manifold. These purging procedures were similar to those used for the sustained load cracking experiments except without evacuating. The vessel was then filled to the test pressure using

99.9999% pure research grade hydrogen. Hydrogen samples taken at the completion of several tests were sent to an independent testing laboratory for analysis; these results were similar to those reported above for the sustained load cracking tests (Sec. 2.2); oxygen was less than 1 vppm although water vapor was observed to be as great as 6 vppm.

Load was applied to the specimens via a pull rod which penetrates the pressure vessel through a series of sliding seals. A secondary, pressure-balancing chamber ensures that the net force acting on the pull rod is zero so that the load applied to the specimen is not affected by the pressure. Crack length was continuously monitored using the direct current potential difference (DCPD) method as described in ASTM E 1737 using constant current values between 3 and 3.6 amperes with the current leads positioned at the W/2 position.

Load line displacement was inferred from a linear variable differential transformer (LVDT) displacement gage attached to the front face of the specimen. The measurement position of the LVDT was at a distance X_M=-14.2mm from the load line. Calibration curves from ref. [26] were used to determine the position of the axis of rotation (X_0/W), relative to the load line, as a function of crack position (a/W)

$$\frac{X_o}{W} = -0.0995314 + 3.02437\left(\frac{a}{W}\right) - 7.95768\left(\frac{a}{W}\right)^2 + 13.546\left(\frac{a}{W}\right)^3 - 10.6274\left(\frac{a}{W}\right)^4 + 3.1133\left(\frac{a}{W}\right)^5 \qquad (6)$$

The crack opening displacement, COD, measured by the LVDT (V_M) can then be translated to an equivalent COD measured at the load line position (V_{LL}) according to

$$V_{LL} = \left[\frac{X_o/W}{X_o/W - X_M/W}\right] V_M \qquad (7)$$

For the compact geometry used, X_M/W is 0.54. The relationship in equation (7) gives a similar result as the relationship in ref. [27], which considers the effect of plasticity on the position of the axis of rotation.

Load was measured using both the external load cell integrated into the test-frame and a second load cell mounted in series with the specimen inside the pressure vessel. This internal load cell consists of an LVDT in an elastically deforming aluminum ring. While loads measured on the external load cell will be affected by friction imparted by the sliding seals in contact with

the pull rod, the internal load cell indicates only the load sustained by the specimen. LVDT based transducers were used to eliminate the uncertainties surrounding the effect of pressurized hydrogen on strain gages in conventional transducers.

Most of the specimens were tested with a constant displacement rate of 0.051mm/min applied by the test frame actuator outside the pressure vessel. One specimen of DOT-3AAX was tested using a rate of 0.0051mm/min to assess the effect of loading rate. These displacement rates yield initial stress intensity factor increase rates of approximately 3 MPa $m^{1/2}$/min and 0.3 MPa $m^{1/2}$/min, respectively.

Upon completion of testing, the specimens were heat tinted in air at 280^0C for about 20 minutes to mark the extent of crack propagation. The specimens were then cooled by submersing in liquid nitrogen and broken apart to reveal the fractured surfaces. Physical pre-crack and final crack positions were measured optically following the procedures outlined in ASTM E1820. J versus Δa crack growth resistance curves (R-curves) were generated using the procedures described in ASTM E1737. Crack position was calculated from DCPD voltage measurements using the relationship described by equation A5.1 in ASTM E1737-96. Crack initiation was determined from the DCPD data as the first change in slope of the DCPD versus COD plot. Fracture thresholds are reported both as the value of J at the onset of crack extension, J_i, as well as at the value of J corresponding to the intersection of the R-curve with the 0.2mm offset blunting line, J_{Ic}.

2.4 Modeling methodology

2.4.1 Verification of K and Compliance solutions

Finite element modeling was used to verify the accuracy of solutions for K and specimen compliance (equations (1) and (5)). Two geometries were examined to understand how solutions may vary for a specimen loaded with a bolt (Figure 5), as the sustained load experiments are carried out, and for a specimen fixtured into the servo-hydraulic load frame (Figure 3), representing the pre-cracking configuration. To be consistent with past work and linear elastic fracture mechanics, all analysis of elastic bodies was regulated to infinitesimal deformations. Simulations were conducted in Abaqus Standard [28] using fully-integrated, four-node quadrilateral elements in plane strain and plane stress. The material was chosen to be isotropic with a Young's modulus E of 207 GPa and a Poisson's ratio ν of 0.3.

The discretizations for the standard WOL and the WOL clevis geometries are illustrated in Figure 7 and Figure 8. For the symmetric, bolt-loaded WOL geometry, a displacement Δ was applied at the load line and the front face displacement $V_{FF,1}$ and reaction load P were recorded. Note that due to symmetry, the total front face displacement V_{FF} is $2V_{FF,1}$. In addition to the load and front-face displacement, the applied stress intensity K_{app} (calculated through a domain integral) was also noted at 20 contours. Because K rapidly converged with increasing radius, we assert K-dominance and consider the finite element solution to be valid.

Solutions were calculated in both plane stress and plane strain. Although the solutions will be different, the normalized parameters presented in later sections will be valid for either plane stress or plane strain provided we normalize by the appropriate modulus, E'; i.e., $E' = E$ for plane stress and $E' = E/(1-\nu^2)$ for plane strain. Because homogeneity holds for the linear theory (i.e. stress scales with displacement), only one analysis step is required.

Simulations were also conducted assuming that displacements were applied to the WOL specimen using a clevis as shown in Figure 3. Equivalent (and opposite) displacements, Δ, were applied to the clevis loading pin and to the loading pin in the lower specimen beam (Figure 8). The front face displacement V_{FF} was the difference between the upper and lower beams of the specimen, $V_{FF,1} - V_{FF,2}$. For each crack length, the load and applied stress intensity factor were also noted. We note that in this specific configuration, we have assumed that the clevis, while bolted, is bonded to the upper beam. While we believe that this assumption provides a bound for the clevis geometry, we did not investigate other representative geometries/boundary conditions. Other element types (eight-node quadrilateral) were also utilized. The differences were found to be minimal and lower-order (bi-linear quadrilateral) elements were found to be sufficient if the domain was properly discretized.

Additional elastic-plastic analyses were conducted for specific configurations. To be consistent, the analysis employed infinitesimal deformations. The hardening was isotropic and given via a piece-wise linear function. Eight-node quadrilateral elements were employed and the loading was resolved over 100 steps. The focus of the analysis was to examine deviations from elasticity and quantify J-dominance. For this work, we define J-dominance to be convergence in the J-integral for increasing radii. Because Abaqus [28] employs a domain integral with a plateau **q** function, increasing contours (frequently 60) translate into increasing radii. Unlike an elastic analysis which usually converges in a few contours, an elastic-plastic analysis frequently

asymptotes to the solution. We considered driving forces which changed by less than 0.1% over the last 5 contours to be converged.

2.4.2 Verification of K-dominance at crack arrest

The stress intensity factor for the WOL specimen was numerically calculated using Abaqus Standard [28] in order to determine whether the proximity of the back face of the specimen to the arrested crack tip would compromise the presumption of K-dominance. Two scenarios were considered, each of which assessed the crack tip condition of an arrested crack near the back face of the specimen. Crack propagation history was not considered.

Finite strain elasto-plastic deformation was considered. In the elastic regime, the material was assumed to be linear and isotropic and in the plastic regime to obey normality, with von Mises yielding and isotropic hardening. Data from uniaxial tension tests were used to construct the flow stress as a function of plastic strain. The specimen was discretized with eight-noded isoparametric plane-strain elements. Deep cracks (a/W=0.81 and 0.94) were loaded to crack mouth opening displacement values comparable to those used in the experiments. It is noted that the contour plots of the effective plastic strain in the neighborhood of the crack tip can be used to discern whether plasticity is confined to the crack tip.

The domain integral approach on contours around the crack tip was utilized to calculate the value of the J-integral. The stress intensity factor associated with the J-integral was then determined through

$$K_J = \sqrt{\frac{EJ}{1-\upsilon^2}} \tag{8}$$

and compared with the stress intensity factor calculated under the assumption of purely elastic specimen response.

Whether K-dominance was the case upon crack arrest was examined by comparing the stress profiles as calculated ahead of the blunting crack tip in the WOL specimen with those prevailing at the crack tip under small scale yielding (SSY) conditions. Figure 9 shows the geometry and boundary conditions used for the SSY calculations. The SSY domain was loaded under plane strain by remote displacements associated with the stress intensity factor K_I obtained from the elastic analysis of the WOL specimen at crack arrest. Thus, the asymptotic displacements of the Irwin singular linear elastic field [29] were prescribed remotely from the crack tip (L is much

larger than the plastic zone size). These displacements were imposed incrementally at a constant stress intensity factor rate toward the final value of K_I which was selected to be consistent with experimentally measured values of K_{THa}.

3 RESULTS

Table 2 is a comprehensive summary of all the fracture threshold tests (both constant and increasing displacement) conducted as part of this study. Specimen identification numbers are provided for each measurement; many specimen IDs, e.g., SA372 grade J (717 MPa), are listed more than once indicating that the specimen was tested at successively increasing values of K_{app}. In these cases, cracks did not propagate at the initial values of K_{app} so the specimens were reloaded to larger displacements and retested. The following subsections will explore the various categories of information from Table 2 in depth.

3.1 Sustained load cracking

3.1.1 Measurements of K_{THa}

Crack arrest threshold stress intensity factors, K_{THa}, were measured for all steels tested with the exception of one heat of SA372 grade J (641 MPa) from which only two specimens were tested and no crack propagation occurred. A trend exists between K_{THa} and yield strength such that K_{THa} values decrease with increasing strength, as has been observed in other studies, e.g. [13]. This trend flattens to a near constant value of K_{THa} for steels with yield strength greater than about 900 MPa; only a small further decrease in K_{THa} is seen as yield strength increases between 900 and 1050 MPa. The values of K_{THa}, measured in 103 MPa H_2 gas, are plotted versus yield strength in Figure 10.

A second trend is recognized between K_{THa} and hydrogen gas pressure. All of the materials were tested in 103 MPa hydrogen gas. Two specimens from DOT-3T (900 MPa B) were also tested in 41 MPa hydrogen gas. These were the only specimens tested at a pressure other than 103 MPa, but the generalities of the trend are evident in Figure 11. K_{THa} increased by nearly 50% when the DOT-3T was tested in H_2 pressure equal to 41 MPa relative to tests at 103 MPa pressure. This trend of decreasing K_{THa} with increasing H_2 pressure is consistent with published data [13].

One values of K_{THa} shown in Table 2 may be of questionable accuracy due to irregular conditions at crack arrest, but is included for completeness. The crack deviated out of the plane defined by the side grooves in DOT-3T specimen #11. K_{THa} for this specimen (50 MPa $m^{1/2}$) is substantially larger than values for the other specimens, most likely due to this crack-front anomaly.

3.1.2 Incubation time

Once the pressure vessel containing the bolt-loaded specimens was filled with hydrogen, some period of time, defined as the incubation time, elapsed before hydrogen induced cracking began. Values of incubation time are given for all specimens in Table 2. If crack propagation occurred, this value refers to the true incubation time, i.e. the time in hydrogen prior to the first indication of crack propagation. For those tests in which the crack did not extend, this value refers to the entire length of time the specimen was exposed to hydrogen gas before being removed from the pressure vessel. Figure 12 shows representative plots of incubation time versus K_{app} for both heats of DOT-3T and two heats of SA372 grade J (717 and 736 MPa). In all materials, the incubation time generally decreased as K_{app} was increased. Of the materials in which crack propagation did occur, the incubation time could always be reduced to only a few hours or less with the application of K_{app} greater than about two times K_{THa}. The longest incubation time for any specimen that exhibited crack extension in 103 MPa hydrogen gas was 1015 hours (SA372 grade J (717MPa), specimen #1 loaded to K_{app} = 140 MPa $m^{1/2}$; Table 2).

Figure 12 shows that there was a minimum value of K_{app} which was greater than K_{THa}, but below which crack extension was never observed. This apparent crack initiation threshold value, K_{THi}^*, varies among the steels tested but was up to two times greater than K_{THa}. Values of K_{THi}^* are shown in Table 3 along with the minimum value of K_{THa} measured for representative heats of each steel specification. The values tabulated for K_{THi}^* in Table 3 are based on the lowest value of K_{app} for which crack extension did occur, with the exception of the DOT-3AAX (641 MPa). Sufficient data were generated for this steel to determine K_{THi}^* as the value midway between the largest value of K_{app} for which no crack extension was observed and the lowest value for which crack extension did occur. Specifically, a K_{app} value of 162 MPa $m^{1/2}$ applied to the DOT-3AAX resulted in an incubation time of 400 hours prior to crack extension (specimen #1), however K_{app}=144 MPa $m^{1/2}$ did not lead to crack extension during an exposure time of almost 4000 hours

(specimen #2). K_{THi}^{*} is thus between 144 and 162 MPa $m^{1/2}$ for this steel in 103 MPa hydrogen gas.

3.1.3 Effect of loading environment

Bolt loading of a majority of the specimens took place within a glovebox containing Ar and less than 2 vppm O_2 and less than 8 vppm H_2O. Specimens from two heats of SA372 grade J and one heat of DOT-3T were bolt loaded in laboratory air in order to compare the effects of loading environment and the possibility that incubation time was a function of the extent of oxide formation on the freshly exposed crack tip. No significant change was observed in K_{THa} or crack growth rates; however, there appears to be a small increase in incubation time for these specimens prepared in air (Table 2). The incubation times for the DOT-3T and SA 372 grade J specimens loaded in air are included in Figure 12. Further tests would be required to determine if this small increase has statistical significance.

3.1.4 Alternate WOL geometries

The crack opening displacements required to exceed K_{THi}^{*} (Figure 12) and ultimately measure K_{THa} led to crack arrest positions that were generally at a/W=0.8 or longer (Table 2). To achieve short incubation times, even larger K_{app} values were required which resulted in even longer arrested cracks. Due to concerns about the proximity of the arrested crack tip to the back face of the specimen, the WOL specimen was modified in such a way as to allow for large values of K_{app} to keep the incubation time short while also ensuring crack arrest further from the back face of the specimen. Unsuccessful attempts to limit the final crack length at K_{THa} by modifying the height to width ratio of the WOL specimen are described in Appendix C.

The final crack length depends on both K_{THa} and the crack opening displacement applied to the specimen (equation (1)). Without changing the length-to-height aspect ratio of the specimen, the applied displacement, V_{FF}, must be smaller in order to achieve shorter final crack lengths, a_f, at a fixed value of K_{THa}. If the crack opening displacement is reduced, a shorter starting crack length, a_0, will be required to maintain sufficiently large K_{app}. The difficulty in this approach lies in the fact that increasingly larger bolt loads become necessary as a_0 becomes shorter. For example, a crack opening displacement of 1.25 mm applied to a 22.2 mm thick conventional WOL specimen with an initial crack length of 0.55W results in K_{app} ~165 MPa $m^{1/2}$ and requires

that the loading bolt sustain a load of nearly 66.7 kN. To achieve this same K_{app} value at a_0=0.3W, the displacement could be reduced to 0.74 mm, but would require that the bolt sustain a load of more than 200 kN. Practical experiences of the authors of this study found that load values around 70 kN represent a physical limit of the load-train used, including loading fixtures in the glove box, the threads cut in the specimen and the loading bolt itself. One or all of these components may fail at higher load values.

A balance between high K_{app} and relatively low load for crack lengths as short as 0.3W was achieved using the chevron notched specimens. The reduced net thickness near the tip of the chevron notch increases the specimen compliance and consequently reduces the load sustained by the loading bolt. Specimens of SA372 grade J (736 MPa) were machined with a chevron notch such that the tip of the notch was at the a/W=0.43 position and merged with the face side-grooves at a/W=0.60 (Figure 2). After pre-cracking, the initial crack lengths were between 0.46W and 0.5W. Final crack lengths at K_{THa} were ~0.03W to 0.06W less for these specimens relative to the conventional WOL specimens loaded to the same values of K_{app} (Table 2). Based on these results, specimens from the DOT-3AAX (607 MPa) and DOT-3T (900 MPa B) were machined with a more acute chevron notch, in which the tip was located at 0.265W and merged with the sidegrooves at 0.7W (Figure 2). This chevron notch geometry lead to a reduction of the final crack length at K_{THa} of 0.05W for the DOT-3T specimens (Figure 13) and 0.20W for the DOT-3AAX specimens in comparison to their straight notch versions (Table 2).

3.1.5 Validity of plane-strain linear elastic fracture mechanics

All values of K_{app} and K_{THa} presented in this paper are calculated using linear-elastic fracture mechanics, however very few of the specimens tested in this study met the specimen size requirements specified by ASTM E1681 for small-scale yielding and plane strain, which requires

$$B, a, b \geq 2.5\left(\frac{K_I}{\sigma_{YS}}\right)^2 \qquad (9)$$

where B, a, and b refer to the specimen thickness, crack length and remaining ligament (W-a), respectively. At the initial load conditions (when K_{app} is applied to the specimen) only the high strength SA372 grade L (1053MPa) specimens meet the criteria in equation (9). At crack arrest, the SA372 grade L (1053 MPa) and DOT-3T specimens also meet the specimen size criteria. None of the other, lower strength steels meet the criteria at either initial loading or crack arrest.

While satisfying equation (9) will generally ensure both plane strain and small-scale yielding, there is no physical reason that failure to satisfy equation (9) necessarily establishes the loss of either plane strain or small-scale yielding.

It has been well documented that the specimen size criterion for plane strain is overly conservative for the B dimension when appropriate side grooves are designed into the specimens [30]. Sidegrooves enhance constraint, effectively creating plane strain conditions along the entire crack front, except near the end points where the presence of the free surfaces relaxes the constraint. In the absence of sidegrooves, the region of reduced constraint extends further from the surfaces and fracture within this region occurs as 45^o shear fracture (forming "shear lips"), whereas fracture within the constrained, plane-strain region appears flat. When the region of shear fracture contributes to a significant portion of the total crack front, non-conservative fracture measurements will result. However, if the regions of shear fracture are small compared to the total crack front, plane-strain fracture can be assumed [30]. The enhanced constraint induced by sidegrooves leads to crack fronts dominated by flat, plane-strain fracture even in relatively thin specimens [30]. Shear lips were either very small or non-existent on the fracture surfaces of all of the specimens tested in this study, suggesting that plane strain conditions dominate our measurements.

It has been argued that the dimensional requirements for small-scale yielding, i.e., limits on a and b in equation (9), were extended to ASTM E1681 and other standards from ASTM E399 [31], in which these criteria were intended to apply only to the use of the 95% secant method for measurement of K_{Ic}. Consequently, failure to satisfy the criteria was not indicative of a loss of small-scale yielding [32]. Rather, it has been suggested that the relative contributions of the elastic and plastic components of the J-integral is a better means to assess small-scale yielding. If the plastic component of J is small relative to the elastic portion, then linear elastic fracture mechanics should be a valid assumption. The in-plane dimensional requirements for J-dominance provided by ASTM E1820 are less strict than those of equation (9)

$$b, B \geq 10\left(\frac{J}{\sigma_{YS}}\right) \tag{10}$$

If the uncracked ligament (b) criterion of equation (10) is met, then J-dominance prevails. Furthermore, K can then be calculated from this J using equation (8).

Elastic plastic J-integral analyses were performed based on the loading conditions for all four of the DOT-3AAX (641MPa) specimens to calculate J at initial loading. Load versus crack opening displacement data measured from the load tup and clip gage during bolt loading revealed deviations from linear loading behavior. The deviation was most pronounced for the lower strength steels loaded to high values of K_{app} and did not occur for the higher strength steels. Actual load versus displacement data during initial loading for DOT-3AAX-4 is shown in Figure 14. The difference in the value of load that would be inferred from the final displacement measurement assuming linear elastic loading is nearly 40% larger than the load measured from the load tup (for these calculations, a *post facto* load tup calibration was applied such that the initial linear loading slope matched the previously measured compliance of the specimen). J was calculated using the procedures described in ASTM E1820; the plastic component of J was calculated assuming the WOL behaves as a CT specimen, which should be a close approximation for the WOL specimen. Using specimen #4 of the DOT-3AAX for example, K_{app} was calculated using the measured applied displacement and equation (1) to be 199 MPa $m^{1/2}$. The elastic-plastic analysis yields J_{app} to be 199 kJ/m^2 from which an equivalent K_{Japp} value of 212 MPa $m^{1/2}$ was calculated. The elastic component of J was 87 kJ/m^2 and the plastic component was 112 kJ/m^2. This plastic component is very large, suggesting elastic behavior is not dominant (as is evident by the load vs. displacement curve in Figure 14); however, the specimen crack tip is expected to be highly constrained since the size requirement of equation (10) requires B only equal 3.1 mm, a condition this specimen easily satisfies.

Although linear elastic fracture mechanics does not apply to specimens with a large plastic component of J, the K_{app} value calculated assuming linear elastic behavior should provide a lower bound on the true crack driving force since it neglects plasticity; however at the same time K_{app} is artificially inflated due to the fact that the assumption of linear elastic loading behavior significantly overestimates the true load on the specimen (Figure 14 shows the load which would be experience by a purely elastic specimen). Nonetheless, the *value* of K_{app} is fortuitously a good representation of the true crack tip conditions (i.e., $K_{app} \sim K_{Japp}$) even though significant plasticity at the crack tip implies the *method* is not rigorously valid. This same scenario was also modeled using finite element methods (section 2.4.1) using the elastic-plastic response behavior of the DOT-3AAX (641 MPa). For the same applied front-face displacement, J was calculated to be 183 kJ/m^2 or K_J=204 MPa $m^{1/2}$.

The above calculations were applied to the DOT-3AAX specimens, since these tests represent an extreme combination of low yield strength and large K_{app}, and thus exhibit the most severe plastic deformation during load application. In fact, few other specimens exhibited any noticeable deviation of linearity of the load versus displacement trace. However, the interface between the loading bolt and the instrumented load tup involved both normal and rotational displacements which, in some cases, led to irregular non-linear loading traces which may have masked small amounts of plasticity in these other specimens. Regardless of the ability to detect small amounts of plasticity during loading, none of those specimen would have exhibited more plasticity than was observed in the DOT-3AAX.

For the higher strength specimens and those with lower values of K_{app}, the assumption of linear elastic loading is valid. For those cases in which plasticity caused deviations from linear elastic loading, the calculation method overestimated the actual load applied by the bolt, but this appears to be offset by an underestimation in the driving force due to neglecting the plastic component of J. *Therefore, it appears that K_{app}, calculated using equation (1), provides a meaningful representation of crack driving force for all specimens in this study*. It should be noted that this result is not expected to be a general conclusion, and should be verified before assuming that it applies to lower strength steels or to different specimen geometries.

It has been suggested that crack tip blunting occurs in low strength steels under large values of K_{app} and that this crack blunting may reduce the effective driving force and lead to non-propagating cracks [13]. Clearly, significant blunting took place in the DOT-3AAX specimen #4 as a result of large crack tip strains. Accounting for these large strains through the use of the elastic-plastic analysis reveals an increase of the effective crack driving force. The presence of crack tip blunting is therefore nothing more than a manifestation of the large crack tip strains and large strains increase the crack driving force.

An elastic-plastic analysis cannot be easily conducted to assess the validity of linear elastic fracture mechanics at crack arrest since the unloading which occurs as the cracks propagate through the fixed displacement specimen invalidates the proportional loading assumption that underlies the validity of the J-integral. Instead, finite element methods (described in section 2.4.2) were used to assess the validity of K at the arrested crack tip. Two scenarios were considered: one assumed a steel with yield strength of 786 MPa and flow properties taken from an X100 C-Mn linepipe steel and the second assumed a steel with properties of the SA 372 grade

J (717 MPa). Simulations of the crack tip stress and strain fields (section 2.4.2) were conducted on WOL specimens having stationary cracks, in which the specimens had a/W values and front-face displacements consistent with experiments at the crack arrest position. In the case of the 786 MPa steel, a front face displacement of V_{FF} =1.2 mm was applied with a crack at the a/W =0.94 position. This modeled a crack which would have arrested at K_{THa} =58 MPa $m^{1/2}$. Both elastic and elastic-plastic analyses were conducted for this scenario. The elastic analysis determined K to be 64 MPa $m^{1/2}$ whereas the elastic-plastic analysis determined K_J to be 62 MPa $m^{1/2}$. In the case of the SA372 grade J steel, the front face displacement was V_{FF} =1.26 mm with the crack at the a/W=0.81 position which corresponds to K_{THa} =109 MPa $m^{1/2}$ (specimen #6 in Table 2). The elastic finite element analysis gave K =119 MPa $m^{1/2}$ while K_J from elastic-plastic analysis was 116 MPa $m^{1/2}$. Figure 15 shows the crack opening stress, σ_{yy}, for the WOL specimen representative of the SA 372 grade J specimen along the axis of symmetry ahead of the crack tip. Superposed on the same figure is the opening stress as furnished by the SSY solution. The strong agreement between these two solutions confirms that there is K-dominance (and also J-dominance) at the crack arrest condition. In summary, the FEM analysis suggests that K appears to accurately describe the crack tip fields even at these long final crack lengths.

3.1.6 Crack growth rates

The measured crack growth rate, da/dt, vs. K relationships for the steels are consistent with the general form commonly observed for many different metals in gaseous hydrogen environments as well as other corrosive environments, e.g. refs. [13,30,33,34]. Environmental cracking is often described as having three stages, in which each stage has a different relationship between crack velocity and applied K. Stage I occurs at K values near K_{TH} and da/dt exhibits a strong dependence on K. Stage II behavior is observed with further increase in K. Crack growth rates during stage II can be either K-independent or may have a mild K-dependence. Stage III crack growth occurs as K approaches K_{Ic} and is characterized by another region in which da/dt exhibits a strong dependence on K.

Crack growth rates were measured for all of the steels that exhibited crack extension in hydrogen gas and representative curves of crack growth rate, da/dt, vs. K for each material are plotted in Figure 16. Since these are decreasing-K tests, the terminal points at low K represent K_{THa}. All of the specimens showed stage I and stage II behavior, with no evidence of stage III

crack growth. Alternately, most of the steels show a brief region of crack acceleration at the highest K values before settling into stage II behavior. The elevated crack growth rates are observed during the first increment of crack growth regardless of the applied K, so this is considered to be an artifact of the test, perhaps due to the crack moving through material immediately ahead of the pre-crack tip that was deformed during bolt loading. These first data points are not shown in Figure 16 for clarity.

Stage II crack growth rates were consistently larger among steels with higher strength and associated lower values of K_{THa}. K independent stage II behavior was only observed in the higher strength steels including the SA372 grade L (1053 MPa), the HY130 and the DOT-3T. K-dependant stage II crack growth behavior was observed for all of the other, lower strength steels as well as for the DOT-3T (900 MPa B) specimens tested in 41 MPa H_2 gas.

The measured K_{THa} values appear to be true thresholds since the crack has effectively arrested rather than continuing to propagate at progressively slower rates. Crack growth rates less than about 10^{-8} m/s could not be consistently measured due to the sensitivity of the data acquisition system and thermal variations in the strain gage outputs, however many of the specimens remained exposed to hydrogen for hundreds of hours after the apparent crack arrest and no systematic change in the load cell output could be detected during this period.

3.2 Rising displacement fracture thresholds

Rising displacement fracture threshold tests were conducted to measure the critical stress intensity factor at crack initiation using specimens from the DOT-3T (900 MPa A), DOT-3AAX (607 MPa), SA 372 grade J (641, 730, 736 and 783 MPa), and SA372 Grade L (1053 MPa). Unlike K_{THa}, which is measured from the crack arrest positions under fixed displacement, these tests were intended to measure crack initiation under conditions of monotonically increasing displacement (Figure 17). Elastic-plastic fracture toughness methods were used to measure J as a function of crack growth. These data were used to generate crack growth resistance curves (R-curves) and to determine J_{IcH}, the elastic-plastic fracture toughness at crack initiation. Representative R-curves are plotted in Figure 18. The DCPD technique used to measure crack length is sensitive enough to detect the point of initial crack extension. The J value at this point of initial crack extension will be referred to as J_{iH} whereas J_{IcH} is determined using the ASTM standard methods (E1737, E1820) which define crack initiation as the intersection of a 0.2 mm

offset blunting line with the R-curve (Figure 18). J_{IcH} is a useful engineering value in that it describes resistance to both crack initiation and to a small amount of crack extension. J_{iH}, however, may be of greater value for comparison with crack arrest thresholds and mechanistic models attempting to predict the onset of cracking. Both J_{iH} and J_{IcH} are tabulated in Table 2 along with dJ_H/da, the slope of the R-curve measured as the average slope between J_{iH} and J_{IcH}.

To facilitate comparison between the two fracture threshold test methods it is useful to convert J_{IcH} to K_{JH} using equation (8). A column of K_{JH} values can be found in Table 2. K_{JH} is less than K_{THa} for all of the steels tested. Figure 19 plots K_{THa} and K_{JH} as a function of yield strength. Although both K_{JH} and K_{THa} generally increase as yield strength decreases, the difference between K_{THa} and K_{JH} increases with decreasing yield strength. Values of dJ_H/da also decrease as the yield strength increases.

3.3 Fracture Surfaces

The HY 130 steels exhibited intergranular fracture. All of the other steels tested in hydrogen gas using both constant displacement and rising displacement methods exhibited similar transgranular fracture surface appearances that were consistent with what has been referred to as plasticity related hydrogen induced cracking (PRHIC) [35]. This fracture mechanism is characterized by complex fracture surfaces with very fine features that are likely related to the tempered martensite microstructure. Increasing amounts of intergranular secondary cracking were observed on the fracture surfaces of the higher strength steels such as the DOT-3T and SA372 grade L. Secondary electron microscopy images of representative fracture surfaces of WOL specimens are shown in Figure 20. Fracture surfaces from the CT specimens tested under rising displacement conditions were qualitatively similar to those from the WOL specimens of the same steel (Figure 21). Fracture surfaces from DOT-3T specimens tested under rising displacement in hydrogen gas and in air are shown in Figure 22. Microvoid coalescence (MVC) was the dominant fracture mechanism for the DOT-3T specimens tested in air.

Several WOL specimens were cross sectioned along a plane parallel to both the crack propagation direction and the crack plane normal. One or more crack bifurcations were typically observed emanating from the pre-crack tip at angles of 45 to 90 degrees from the fracture plane in those specimens that exhibited hydrogen-assisted crack extension. In the most severe case, specimen DOT-3T-1, a crack branch at ~45^o to the primary fracture plane extended 4 mm from

the pre-crack tip (Figure 23a). Crack branches observed in the SA372 grade J (717 MPa) and DOT 3AAX (641 MPa) were much shorter; between 100 and 200 μm (Figure 23(b) and (c)). Such crack bifurcations were not observed in specimens that were loaded to K_{app} values less than K_{THi}^{*} and which therefore did not exhibit hydrogen-assisted crack extension. For example, two specimens (DOT-3T-8 and SA372 grade J K236-1A) that were loaded to K_{app} values greater than K_{THa} but less than K_{THi}* (58 and 200 MPa $m^{1/2}$, respectively) and did not exhibit crack extension were sectioned and examined using electron microscopy. Four sections, evenly spaced through the thickness, from the DOT-3T specimen and five evenly spaced sections from the SA 372 grade J specimen revealed no hydrogen-assisted crack extension beyond the end of the pre-crack (Figure 24). While 40 to 100 μm of crack extension occurred beyond the blunted pre-crack tip in the SA372 grade J specimen (Figure 24(c)), spherical voids were also observed in this region suggesting that this small amount of crack extension may have resulted from bolt loading in the glovebox; 200 MPa $m^{1/2}$ is likely near, or perhaps greater than, K_{Ic} for this alloy.

4 DISCUSSION

4.1 K_{THa} values compared with published values

Loginow and Phelps published the only other known set of data for comparable conditions of steel type and strength, hydrogen pressure, and test method [13]. These data are well known to most pressure vessel and gas cylinder manufacturers and users and are often used as guidance for design of hydrogen containment vessels (e.g. [17]). It seems necessary, therefore, to address the differences and similarities between K_{THa} values measured by Loginow and Phelps and those in this study. The general trends between K_{THa} and yield strength or hydrogen pressure are consistent between both studies, however the magnitudes of K_{THa} for otherwise similar steels are consistently larger in this study relative to the values reported by Loginow and Phelps, as shown in Figure 25.

These differences in K_{THa} values must reflect either properties of the steels or the methods used to measure the properties in each study. It is plausible that the modern steels in this study have improved resistance to hydrogen assisted cracking; steelmaking advances during the 30+

years separating these studies have resulted in steels with generally better mechanical properties including increased fracture toughness (e.g. [36]). Alternately, although the experimental procedures used in this study were very similar to those used by Loginow and Phelps, one potentially significant difference involves the analytical solution used to calculate K for the WOL specimen. The K solution referenced by Loginow and Phelps is that by Novak and Rolfe [37] which was likely the best available solution at that time. The deviation between this solution and that presented in equation (1), however, is evident over all crack lengths and is especially notable at crack lengths greater than a/W=0.8 (Figure 26). As the crack length approaches a/W=0.9 the stress intensity factor calculated from equation (1) is nearly twice that predicted by the Novak and Rolfe solution. Loginow and Phelps did not report the final crack-lengths associated with their K_{THa} measurements, however it can be inferred that at least some of their measurements were made from specimens having final crack lengths of a/W=0.85 or greater[§].

The different K-solutions combined with long final crack lengths may explain much of the differences in K_{THa} between the two studies. With the exception of the high strength steel SA 372 grade L (1052 MPa), we were unable to achieve any arrested crack lengths in straight notch specimens that were less than a/W=0.77 and for most materials the minimum final crack length was closer to a/W=0.9 as shown in Table 2 (further discussion of this testing challenge is presented in the next section). There is little reason to doubt that Loginow and Phelps would have had similar difficulties maintaining a/W<0.8; therefore nearly all of the reported values in both studies may be from specimens with crack-lengths, a/W, greater than 0.8.

Figure 25 includes values of threshold stress intensity factors calculated from the data in Table 2 (crack opening displacement, final crack length, etc.), but using the formula for the calculation of the stress intensity factor as employed by Loginow and Phelps. In addition, these threshold values are calculated assuming an elastic modulus (E) of 186 GPa, as used by Loginow and Phelps, whereas K_{THa} values listed in Table 2 assume E=207 GPa. This alternate set of K_{THa}

[§] A plot of stress intensity factor versus crack growth rate in Ref. 13 shows that K_{app} values for some of the specimens were as large as three times K_{THa} suggesting that the final cracks lengths must have been quite long. In addition, Ref. 13 describes a modification to the stress intensity factor solution that was used for cracks greater than a/W=.85; presumably, this modification would not have been necessary unless there were specimens with long cracks. The modification that was used is not well explained, but is attributed to ref. 38. Our attempts to use the information in this reference to modify Novak and Rolfe's stress intensity factor solution accounted for only a small amount of the difference between Novak and Rolfe's solution and that in ASTM E1681 shown in Figure 26.

values corresponds more closely with the Loginow and Phelps data further suggesting that the formulae used to calculate the threshold, rather than different material properties, may explain much of the difference in K_{THa} results between the two studies. The remainder of the difference shown in Figure 25 may result from differences in the metallurgy of the steels or it may be a result of somewhat larger specimens used by Loginow and Phelps, as will be discussed in Section 4.3.2.

4.2 Fracture mechanisms

The fracture modes observed in the intermediate-strength, tempered low-alloy steels from this study are complex and difficult to interpret from fracture surface evidence but are similar to most other observations of hydrogen-assisted fracture in quenched and tempered steels with similar strength levels. Considering the four "classical" fracture modes being intergranular, microvoid coalescence, cleavage and quasi-cleavage [39,40], the fracture surfaces from this study (Figure 20 and Figure 21) suggest that the fracture mode is quasi-cleavage. Indeed, other studies have described fracture surfaces of hydrogen-assisted crack growth in martensitic steels as reflecting quasi-cleavage, e.g. [41,42,43]. For those attempting to use fractography to understand fracture mechanisms, however, quasi-cleavage is a rather unsatisfying term due to the fact that it is generally invoked only to describe a fracture surface *appearance* [44,45,46] whereas the other common fracture mode descriptions (i.e., intergranular, microvoid coalescence, and cleavage) pertain to specific fracture *mechanisms* that have unequivocal fracture surface appearances [30].

Attempting to assign a name to a fracture appearance without an associated fracture mechanism has likely caused confusion about hydrogen-assisted fracture of lower strength steels. The term quasi-cleavage was originally derived by Beachem to describe cleavage-like fracture of martensitic steels in which the complex fracture surfaces did not allow the fracture plane to be positively identified as a cleavage plane [44]. In a following publication, Beachem identified the quasi-cleavage fracture plane to be, in fact, consistent with (001) ferrite cleavage planes and thus determined that the modifier "quasi… appears to be unnecessary for quenched and tempered steels" [47]. The primary difference in appearance between classical cleavage fracture and those cases initially described as quasi-cleavage in appearance was related to the nucleation sites of the

cleavage cracks; for those surfaces previously identified as quasi-cleavage, the cracks nucleated at dispersed sites leading to many small, isolated cleavage facets connected by tear ridges [44].

Fracture surfaces have continued to be described as quasi-cleavage based on surface appearance similar to those originally described by Beachem, although in some cases the actual fracture mechanism may be different. The fracture plane of some fracture surfaces produced by hydrogen-assisted fracture have since been identified as (110) types [48] indicating true ferrite cleavage is not the active fracture mechanism. Fracture surfaces that are often referred to as evidence of "quasi-cleavage" generally reflect the martensitic lath structure based on visual similarities between the fracture surface and the microstructure [41,42] and most proposed mechanisms of "quasi-cleavage" involve either fracture along martensite lath interfaces [48,49], cleavage along $(110)_{\alpha'}$ in martensite [50] or glide plane decohesion [51,52]. Thompson adopted a literal interpretation of the original descriptions of quasi-cleavage, namely that it should exhibit flat facets with linear tear-ridge features emanating from within the facet and that these tear ridges should match with similar features on the opposite fracture surface [46]. Based on this interpretation, Thompson determined that another fracture mode description was required based on fracture surface features, often associated with hydrogen-assisted fracture, which did not precisely match the features associated with the strict definition of quasi-cleavage. This new fracture mode is called tearing topography surface, or TTS [53], which is described as a fracture surface characterized by "ductile or microplastic tearing on a very fine scale," thus defining another fracture mode based on surface appearance rather than by mechanism. TTS has been invoked in other studies and described as "poorly defined dimples" [54] and has also been used to characterize fatigue fracture [55].

Based only on fracture surface appearance, the fracture modes exhibited in Figure 20 and Figure 21 might easily be identified as either "quasi-cleavage" or TTS. Ultimately, the hydrogen-assisted fracture mechanisms which lead to these imprecisely defined fracture surface appearances are not known. It is clear, however, that the fracture modes reflected by the fracture surfaces are neither true cleavage nor intergranular fracture but they do reflect significant contributions from plasticity.

Recognizing the consequence of describing a fracture surface appearance that does not consider the fracture mechanism, Takeda and McMahon chose to refer to the fracture modes they observed in a low alloy martensitic steel tested in hydrogen gas as plasticity related hydrogen

induced cracking (PRHIC) [35] so as to direct attention to the role of plasticity in the fracture process. This mechanism-based term avoids misleading inferences associated with terms derived based on fracture surface appearance. The term PRHIC is preferred here until specifics of the fracture mechanism are better understood; regardless of the term used, e.g., "quasi-cleavage", TTS, or PRHIC, it is generally accepted that these fracture appearances all indicate a role for plasticity in the fracture process [53,56]. The general fracture appearance of PRHIC is arguably similar to all of the above references to either "quasi-cleavage" or TTS as well as to the fracture surfaces shown in Figure 20 and Figure 21.

With the exception of the HY-130, which exhibited primarily intergranular fracture, all the other steels tested in this study exhibited PRHIC in both constant displacement and rising displacement tests. It can be speculated that PRHIC involves some combination of stress-controlled micro-cracking events, such as martensite lath interface decohesion or cleavage within martensite laths, combined with strain-controlled ductile rupture of the remaining material. This general mechanism remains consistent with the original intent of the term quasicleavage [44], i.e., some combination of stress- and strain-controlled fracture modes, as well as the original explanation of PRHIC , e.g. [35]. In this sense, PRHIC is similar to microvoid coalescence, the conventional ductile fracture mode, in that the crack propagates macroscopically as a result of many stress-controlled nucleation events that ultimately coalesce as a result of accumulated plastic deformation. Perhaps the most important point to emphasize is that PRHIC, as pointed out by Takeda [35], is a strain-controlled fracture mechanism.

The mechanism for hydrogen-assisted fracture of these steels is strain controlled, meaning that local processes are governed by the continuum crack-tip plastic strain. Quantitatively, such failures are described by a criterion in which the continuum crack-tip strain exceeds a critical value, ε^*, over a characteristic distance, l^*, ahead of the crack tip [57,58]. This characteristic distance is generally the distance spanned by a microstructural crack emanating from the main crack. Based on the Hutchinson-Rice-Rosengren (HRR) crack-tip field solutions, the critical stress intensity factor for crack extension can be related to the critical strain and the characteristic distance as [57,58]

$$K_{Ic} \propto 6\sqrt{E\sigma_0 l^* \varepsilon^*} \tag{10}$$

The hydrogen gas environment degrades the critical stress-intensity factor and so, according to this strain controlled fracture criterion, must reduce either ε^*, l^* or both. Full consideration of

both ε^* and l^* is required to describe the failure condition for strain controlled fracture, however for the qualitative purposes of this paper, we will consider the role of hydrogen primarily to reduce the critical strain from ε^* to ε^*_H.

Hydrogen is presumed to decrease fracture resistance by altering the relationship between the continuum crack-tip strain and local processes leading to fracture. Specifically, hydrogen is known to alter deformation in a wide range of metals, primarily by enhancing localized deformation (e.g. [59,60]), leading to fracture at lower values of K (and thus at lower values of the continuum strain, ε) (e.g. [61]). We therefore postulate that the following general sequence of events describes the fracture process of hydrogen assisted crack growth in low alloy steels:

- Hydrogen promotes localized deformation in material near the crack tip. The localized deformation evolves in proportion to the continuum crack-tip strain.
- Microcrack formation results from the strain incompatibilities associated with localized deformation.
- Microcrack formation and ensuing crack extension preempt accumulation of strain to ε^*.
- $\varepsilon^*_H < \varepsilon^*$, where ε^*_H is the critical continuum crack-tip strain for hydrogen assisted fracture.

Strain controlled fracture is strongly dependant on the local distribution of strain, which in turn can depend on plastic strain history [62]. The local distribution of strain and its interactions with the local microstructure governs the levels of continuum strain that can be sustained at the crack tip prior to fracture. This is evidenced by the observations that low alloy steels fracture via microvoid coalescence (MVC) in the absence of hydrogen but fracture via PRHIC in the presence of hydrogen. Both are fracture processes that can be modeled by considering the continuum crack-tip strain, however the micromechanisms of the fracture processes are quite different. In the absence of hydrogen, strain incompatibilities between the matrix and rigid, non-metallic inclusions lead to the development of local dislocation structures at the particles. This produces large stress concentrations which lead to void nucleation at the particles [63]. Further strain accumulation results in growth and eventual coalescence of the voids. Without changing the distribution of non-metallic inclusions, however, the MVC process is conspicuously absent when fracture specimens are tested in hydrogen. The presence of hydrogen must therefore substantially alter the plastic strain distribution such that damage nucleation occurs at different

microstructural initiation sites, possibly including shear band intersections [64], martensite lath boundaries [65] or fine cementite particles within martensite laths [65]. Since the local strain distributions leading to microvoid fracture and hydrogen-assisted fracture are so different, we assert that any continuum strain that accumulates prior to hydrogen exposure does not contribute to hydrogen-assisted fracture, i.e., ε^*_H only reflects continuum strain accumulated during hydrogen exposure.

The two fracture threshold test methods in this study differ rather significantly in terms of the strain history at the crack tip. During measurement of K_{JH}, loading and hydrogen exposure are concurrent, thus crack-tip strain accumulates during hydrogen exposure throughout the entire loading history such that the total accumulated strain, $\varepsilon = \varepsilon_H$. In contrast, when loading and hydrogen exposure are sequential, e.g., during measurement of K_{THa}, much of the crack-tip strain accumulates prior to exposure to hydrogen and therefore does not contribute to ε_H. Only the strain that accumulates under static loading conditions after the specimen is exposed to hydrogen contributes to ε_H.

The strain which accumulates during static loading at $K=K_{app}$ is supplied by crack tip creep. Creep occurs at room temperature as a result of thermally activated dislocation glide [66,67,68]. The schematic shown in Figure 27 is a common representation of the energy barrier to dislocation glide past an obstacle. Application of stress alters the energy versus distance profile resulting in a lower energy state for a dislocation on the far side of the barrier relative to the near side, and thus increases the probability that the dislocation will pass the barrier via thermal activation. Increasing the stress on a dislocation (i.e. by increasing K_{app}, Figure 27b) reduces the amount of thermal energy needed to activate the dislocation past the obstacle [69].

Hydrogen will enhance crack tip creep strain under static loading conditions by reducing the activation barrier for dislocation motion [5,60,70,71,72] as demonstrated by the dashed curves in Figure 27. Direct evidence of such hydrogen-activated crack-tip strain has been provided by Chu *et al* [73,74]. In their studies, WOL specimens made from low alloy steels with tensile strengths ranging from 780 MPa to 1810 MPa were loaded to various K_{app} levels and then exposed to hydrogen-containing environments (H_2S gas, H_2S solutions and water). Evolution of the crack tip plastic zone was observed using metallographic shadowing techniques; the initial plastic zone did not enlarge with time while exposed to air, however in all cases substantial growth of the plastic zone was observed to precede cracking in the hydrogen environments. This

process was observed for steels which eventually exhibited either intergranular or PRHIC fracture modes [74].

Crack extension in the bolt loaded WOL specimens is therefore expected to occur only when the hydrogen-activated crack-tip strain accumulation exceeds ε^*_H. The displacement applied by the loading bolt induces the crack-tip stress needed to enable hydrogen-activated dislocation motion; if this far-field displacement and associated crack-tip stress are not sufficient for the accumulated crack-tip strain, ε_H, to exceed ε^*_H, crack extension will not occur.

4.3 Challenges associated with sustained load cracking tests

4.3.1 Incubation time

For those specimens loaded to $K_{app}>K_{THi}^*$ there existed an incubation period between the time the specimen was exposed to hydrogen gas and the onset of crack extension (Figure 12). The cause of this incubation period has been previously attributed to oxides on the crack tip surface impeding hydrogen adsorption and/or dissociation [13]. This assumed role of oxides on the crack surfaces is based primarily on observations of high strength steels, in which crack extension in low pressure hydrogen was arrested by introducing oxygen to the gas and was subsequently restarted by removing the contaminant [10,75]. A delay in the resumption of hydrogen-assisted crack extension after removal of oxygen was attributed to the time necessary for hydrogen to reduce the remaining oxygen on the metal surface [75]. The incubation times reported by Loginow and Phelps were attributed to oxides that formed on the surface of the crack tip following loading of the specimen in air which then impeded the ingress of hydrogen [13].

In the present work, bolt loading of specimens was conducted in air as well as in a glovebox containing 0.1 MPa argon with only ~1 vppm oxygen. Since the glovebox was intended to minimize oxide formation on fresh metal exposed at the deformed crack tip, significantly smaller incubation times from those specimens loaded in argon would have been strong evidence that an oxide layer was responsible for the incubation time for specimens loaded in air, however, such notable differences were not observed. The plots in Figure 12 suggest that bolt-loading specimens in argon may decrease the incubation time slightly, however, data from this study are too limited to make definitive conclusions about the effect of applying load to the specimens in air versus in argon.

The lack of significant variation in the incubation times between the specimens loaded in air and those loaded in argon does not imply that formation of oxides on the crack surfaces have no role in limiting hydrogen uptake. The kinetics of oxide growth suggest that there may actually be little difference between the oxide layers formed in the two loading environments. At room temperature, oxide films on iron are found to grow quickly to a limiting thickness, with little or no further growth occurring regardless of exposure time [76,77]. The limiting (or saturation) thickness of oxide layers grown on pure iron crystals at room temperature is reported to be 1.0-2.5 nm [78] while measurements on Cr-Mo low alloy steels indicate a saturation thickness of 2.5-6.5 nm which developed after less than 5 minutes of exposure to air at atmospheric pressure [79]. Various studies of pure iron in room temperature vacuum environments suggest that this limiting film thickness is reached very quickly even with very low oxygen partial pressure. One such study found this saturation time to be around 1 hour for iron exposed to 10^{-4} Pa oxygen [80], while another measured saturation to occur after about 7 minutes for iron exposed to $5x10^{-4}$ Pa oxygen [76]. The environment inside the glovebox used to prepare specimens for the current work contained a partial pressure of oxygen equal to about 0.1 Pa (1 vppm oxygen in argon at a pressure of 0.1 MPa). Considering that the WOL specimens were exposed to the loading environment (air or argon) for a period of typically two to five hours between load application and exposure to hydrogen, it is reasonable to assume that all specimens, regardless of loading environment, had similarly thick oxide layers on the crack surfaces. If the observed slight differences in incubation time between specimens loaded in air and those loaded in Ar are related to the oxide layer, it may be due either to very small differences in oxide layer thickness or to different oxide morphologies, which may result from differences in humidity and other impurity gases present (e.g. small differences in lattice parameter have been observed for oxides grown in atmospheric air and vacuum [78]).

The relationship between incubation time and K_{app} (e.g. Figure 12) demonstrates that the initial mechanical condition (K_{app}) is the most significant variable affecting the incubation time. Three possible contributions of K_{app} to the incubation time can be postulated. Firstly, large values of K_{app} will increase crack tip creep strain rates which could lead to the fracture of crack-tip surface oxides. Secondly, crack tip creep enhanced by hydrogen will facilitate strain accumulation in the presence of hydrogen. Thirdly, the critical concentration of hydrogen

needed for crack extension may decrease as K_{app} is increased; at large K_{app}, these smaller critical concentrations will develop more quickly than would larger concentrations.

Crack tip creep deformation is presumed to fracture protective oxide layers and enable stress corrosion cracking in aqueous environments [81]. If an oxide film inhibits the uptake of hydrogen at the crack tip in constant displacement specimens used in this study, then the variable governing incubation time may not be oxide thickness but rather the creep strain rate at the crack tip. This notion is consistent with the observed strong correlation between incubation time and K_{app} such that the incubation time is greatest at K_{app} just above K_{THi}^{*} and decreases rapidly as K_{app} is increased since larger creep strain will develop from larger values of K_{app} [82,83]. Similar correlation between incubation time and K_{app} has often been observed in stress corrosion cracking experiments of ferritic steels in aqueous solutions, e.g. refs. [84,85,86].

In addition to fracturing surface oxides on the crack surfaces, crack tip creep contributes to the accumulated strain that must reach a critical value (ε^{*}_{H}) before strain-controlled, hydrogen-assisted fracture can occur. As discussed in Section 4.2 (and as will be further discussed in Section 4.3.2) hydrogen alters the accumulation of deformation. Deformation accumulated prior to exposure to hydrogen may not directly contribute to ε^{*}_{H}. The incubation time may be reflecting the time required for hydrogen-activated crack-tip strain accumulation to reach ε^{*}_{H}.

The third possible explanation for the contribution of K_{app} to the incubation time relates to the reduced value of critical hydrogen concentration necessary for crack extension at larger K values. Early models assumed that the incubation time reflected the time required for the crack-tip hydrogen concentration to reach the critical level for crack extension at a fixed K level, e.g. [87,88]. These models appear to match the data then available from high strength steel specimens. These high strength steel specimens were loaded while exposed to hydrogen, so surface oxides were not an impediment to hydrogen uptake and, since the fracture mode was presumably stress-controlled, intergranular fracture, there would not be any requirement for strain accumulation while exposed to hydrogen. The agreement between these models and experimental results suggest that the time required for hydrogen transport to the crack tip should not be ignored in regards to its contribution to incubation time.

Assuming that the incubation time reflects the time required for the crack-tip hydrogen concentration to reach a critical level, a reduced incubation time indicates a lower crack-tip hydrogen concentration for crack extension. Numerous data have demonstrated a relationship

between the K level for crack extension and crack-tip hydrogen concentration [89,90], including the data in Figure 11, such that a reduction in one variable requires an increase in the other. For example, when K_{app} is large, crack propagation occurs at a smaller crack tip hydrogen concentration. Since smaller hydrogen concentrations develop in less time than larger concentrations, it follows that the incubation time decreases as K_{app} increases. In the limiting case that the critical concentration equals the local equilibrium concentration of the material, the transient time to reach the critical concentration may become quite extended [91] since diffusion rates will slow in response to the decreasing concentration gradient.

4.3.2 Threshold measurements from constant displacement specimens

Standardized test methods, such as ASTM E1681, the standard referenced for most of the procedures in this study, and ISO 11114-4, the ISO test method for selecting metallic materials for transportable hydrogen gas cylinders, allow the threshold stress intensity factor to be determined based upon the minimum value of K_{app} for which minimal or no crack extension occurs (i.e. K_{THi}^*). In the current study, specimens loaded to stress intensity factor values just below K_{THi}^* were exposed to hydrogen gas for over 18,000 hours with no indication of crack propagation (e.g., SA372 grade J specimens 7 and 8 in Table 2). K_{THi}^* appears to be a practical minimum K_{app} value below which crack extension will not occur regardless of how long the constant-displacement specimen is exposed to hydrogen.

The apparent threshold, K_{THi}^*, can easily be identified in Figure 12 as the value of K_{app} below which cracking did not occur and is represented approximately by the right edge of the shaded area. However, the left edge of the shaded area of Figure 12 represents the approximate values of the crack arrest threshold, K_{THa}, which are clearly much less than K_{THi}^*. Thus it becomes important to consider the meaning of a fracture threshold. In structural design, the threshold stress-intensity factor is typically assumed to be the K level below which sub-critical crack extension will not occur. K_{THi}^* should not be used as a threshold value in the engineering design and analysis of hydrogen containment structures since it only appears to describe threshold behavior of fracture mechanics specimens loaded in an inert environment and then subsequently exposed to hydrogen, a condition which is not representative of a flaw on the internal wall of a structure internally pressurized with hydrogen gas.

In previous publications [35,92], it was suggested that in studies in which cracks did not propagate at $K_{app}>K_{THa}$, the phenomenon could be attributed to hydrogen-induced bifurcation of the primary crack tip during the initial stages of crack extension, since crack bifurcation could lead to shielding of the K-field and inhibit macroscopic crack extension [93]. However, it is now evident that this does not explain the apparent threshold behavior at K_{THi}^*. While crack bifurcation at the pre-crack tip in specimens with $K_{app}>K_{THi}^*$ has been observed (Figure 23), there was no evidence of such crack bifurcation in specimens loaded to K_{app} that is greater than K_{THa}, but less than K_{THi}^* (Figure 24). It appears that the bifurcation occurs simultaneously with extension of the primary crack in hydrogen gas when $K_{app} > K_{THi}^*$ and does not account for the absence of crack extension when $K_{app} < K_{THi}^*$ Rather, we now postulate that K_{THi}^* represents the critical, static value of K_{app} necessary to drive hydrogen-activated straining to a critical value, ε^*_H, as discussed in section 4.2.**

This crack-tip mechanics interpretation of K_{THi}^* underscores that strain-controlled, hydrogen-assisted fracture is dependant on both the mechanical and environmental histories. Figure 28 illustrates three possible scenarios for load history relative to hydrogen exposure history pertinent to the threshold tests in this study and indicates why K_{THi}^* should not be viewed as a true threshold for hydrogen-assisted cracking. When load is applied concurrent with hydrogen exposure (K_{JH} measurements, Figure 28 (a)), all of the strain accumulated at the crack tip contributes to ε_H and crack initiation occurs when $\varepsilon_H = \varepsilon^*_H$.†† Mechanistically, the hydrogen-induced localized deformation is active throughout the entire loading history.

Figure 28(b) and (c) depict how the scenarios change when load is applied prior to hydrogen exposure (K_{THi}^* and K_{THa} measurements). In these cases, strain which is accumulated during load application does not contribute to attaining ε^*_H, i.e., localized deformation is not induced by hydrogen during loading. Only the hydrogen-activated creep strain which accumulates after hydrogen exposure (ε_H) contributes to the attainment of ε^*_H. Therefore, the final fixed-displacement loading condition (K_{app}) dictates whether crack extension occurs, since this driving force governs the hydrogen-activated crack-tip creep leading to crack extension at ε^*_H.

** This statement assumes that the loading rate in hydrogen gas is sufficiently slow, as will be discussed in section 4.5.

†† For simplicity, it is assumed that the critical strain at the fracture threshold is equal for both threshold measurements (i.e., K_{THa} and K_{JH}) and represented by ε^*_H.

The scenario in Figure 28(b) describes the conditions associated with tests having $K_{app}<K_{THi}^{*}$. In Figure 28 (b), $K = K_3$ is applied to the specimen prior to hydrogen exposure. As suggested by Figure 28(a), K_3 would be sufficient to cause crack initiation if loading and hydrogen exposure were concurrent. K is then maintained at K_3 as the specimen is exposed to hydrogen gas and hydrogen-activated strain accumulates at the crack-tip. The hydrogen-activated creep strain rate will decay with time since the remotely applied crack opening displacement (and K_{app}) remains static [81,82]. K_3 is insufficient in magnitude for ε_H to accumulate to ε^{*}_H so crack initiation will never occur, i.e., K_3 is less than K_{THi}^{*} in Figure 28(b).

The scenario in Figure 28(c) describes the conditions associated with tests having $K_{app}>K_{THi}^{*}$. When a larger displacement is applied to the specimen larger hydrogen-activated creep strain rates occur in response to the greater crack-tip stress [82] and thus the accumulated strain in hydrogen, ε_H, will be greater. If $\varepsilon_H \geq \varepsilon^{*}_H$ crack initiation will occur. In the example shown by Figure 28(c), sufficient strain has accumulated for crack extension to occur at K_4, which is greater than K_{THi}^{*}.

Following initial crack extension in hydrogen gas, the strain field will progress with the crack tip such that strain accumulated at successive crack positions will contribute to ε_H. When the crack tip has moved sufficiently far from the initial position, all of the strain accumulated at the crack tip will have developed during hydrogen exposure and contributes to ε_H such that the condition for crack arrest can be described by $\varepsilon = \varepsilon_H = \varepsilon^{*}_H$. Therefore, K_{THa} is a crack arrest threshold which may not be influenced by hydrogen exposure history, however its characteristics as a fracture threshold will still be influenced by deformation history.

A propagating crack experiences non-proportional deformation in the active plastic zone ahead of the crack tip as well as a region of elastic unloading behind the advancing crack tip [94,95]. This region of elastic unloading leaves behind a wake of residual plastic deformation and results in a different strain distribution at the propagating crack tip relative to a stationary crack tip [94,95]. Namely, strains decay with 1/r ahead of a stationary crack but only with ln(1/r) ahead of a propagating crack in steady state, where *r* refers to the distance from the crack tip [95]. Therefore, at a fixed value of K and at a given position ahead of a crack, the strain is lower for the propagating crack relative to the stationary crack.

This difference in crack tip strain magnitude between a stationary and a propagating crack leads to an apparent toughness increase in materials which fail via strain controlled fracture since

ε^* (or ε^*_H) remains unchanged [96]. This allows stable crack propagation to occur and is a source of extrinsic crack growth toughening in elastic-plastic materials. It is reasonable to presume that the magnitude of this toughening will scale with the volume of elastically unloading material in the crack wake which in turn scales with the size of the crack tip plastic zone. Under conditions of increasing crack opening displacement, a positive feedback loop is developed by which increasing crack growth toughness leads to larger values of applied K, and these larger values of K in turn lead to an increase in the plastic zone size which causes a further increase in crack growth toughness. This process will not continue indefinitely as a steady state condition will eventually be reached.

Most importantly, although the critical fracture strain ε^* or ε^*_H remains unchanged, the resistance to crack extension as measured by the far-field loading (e.g., K) is explicitly related to the deformation history at the crack tip. Consequently, the threshold stress intensity factor measured for the arrest of a propagating crack (e.g., K_{THa}) will not be equivalent to the threshold stress intensity factor measured for the initial extension of a stationary crack (e.g., K_{JH}). Although the deformation history at the crack tip in a specimen subject to a decreasing stress intensity factor (as is the case for the WOL specimens tested in this study) will vary from the more typical case of a specimen subjected to an increasing K, the concept of crack growth toughening nonetheless applies in both cases.

Figure 29 and Figure 30 qualitatively illustrate how crack-tip deformation history will affect the measurement of the crack arrest threshold, K_{THa}. In Figure 29 (a) and (b) the difference in deformation history for two different values of K_{app} (200 and 160 MPa $m^{1/2}$) is illustrated using circles to represent the sequence of plastic zone sizes as the crack propagates from its initial position to the arrest position, assuming in both cases that the initial crack position, a/W, is 0.55 and the yield strength is 641 MPa, e.g. DOT-3AAX (641 MPa) specimens 1 and 4. Figure 29(c) demonstrates the reduced influence of deformation history that is experienced by a specimen with yield strength of 900 MPa and K_{app} of 84 MPa $m^{1/2}$, e.g. DOT-3T (900 MPa A) specimen 2. Figure 29 is drawn to scale assuming W=56.9 mm and the plastic zone radius is calculated using Irwin's approximation for plane strain [30]

$$r_p = \frac{1}{3\pi}\left(\frac{K_I}{\sigma_Y}\right)^2 \tag{11}$$

The crack arrest threshold, K_{THa}, can be defined as the intersection between K_{app} and the specimen's resistance to crack growth, K_R, both of which vary with crack extension as shown in Figure 30. Work is consumed due to non-proportional plastic deformation ahead of the crack tip; as the crack propagates the deformed material unloads in the wake of the crack, but only the elastic component of the work is recovered. The crack-growth resistance, K_R, is proportional to the total work of fracture and includes the non-recoverable plastic work dissipated in the crack wake. The magnitude of the non-recoverable work dissipated in the crack wake during a given increment of crack extension is determined by the total strain that accumulated ahead of the crack. The plastic strain and plastic work attributed to the current crack position will scale with the volume of the plastic zone per unit thickness, r_p^2, however the total plastic strain will also include the strain which accumulated as the crack grew from prior positions. The size of the plastic zone at those prior positions, and the gradient by which the size of the plastic zone decreases as the crack grows, will affect the total plastic strain.

Given the above description of the relationship between K_R and crack growth history (i.e., plastic zone history), we expect K_R can be related to crack extension as depicted in Figure 30. The work dissipated in the crack wake is proportional to r_p^2; expressed in terms of the stress intensity factor, this dissipated work is proportional to K_R^2, or $K_R \alpha r_p$. From equation (11), it follows that $r_p \alpha (K_{app}/\sigma_{YS})^2$, and therefore Figure 30 depicts $K_R \alpha (K_{app}/\sigma_{YS})^2$. Although equation (11) should only be applied to a stationary crack, a similar proportionality between r_p and $(K_I/\sigma_{YS})^2$ has been determined for a crack propagating at steady state [97,98], thus we may be tempted to infer that this proportionality applies to crack propagation at non-steady state as well. The dashed lines representing K_{app} and K_{TH} in Figure 30 are defined by equation (1) and equation (10), respectively.

When the conditions are met for initial crack extension, as depicted in Figure 28(c), K_{app} must be greater than K_R. As the crack propagates, K_{app} decreases according to equation (1) while the plastic zone size diminishes according to equation (11) as shown schematically in Figure 29. Crack propagation will continue until K_{app} equals K_R, at which point the crack arrests and K_{THa} is established. In comparison, the criterion for the true fracture threshold (K_{TH}) is related to the critical fracture strain and the characteristic fracture distance, $(\varepsilon^*_H l^*)^{1/2}$, which is presumed to be independent of deformation history and crack length. As long as some amount of plastic work is dissipated in the crack wake, K_R must remain greater than K_{TH}.

The elevation of K_R above K_{TH} will depend on factors that affect the amount of plastic work that is dissipated in the crack wake. Higher strength steels, for example, will have a smaller plastic zone, not just due to the increased yield strength, but also as a consequence of the smaller K_{app} values that can be imposed on specimens with lower fracture thresholds. As a result, plastic work dissipation in the crack wake will impart a larger relative contribution to the total work of fracture for lower strength steels, leading to an elevation of the K_R vs. crack extension curve. Consequently, the difference between measurements of K_{THa} and K_{TH} will be larger for lower strength steels compared to higher strength steels, as illustrated in Figure 30.

A dependence of K_R on specimen size and applied stress intensity factor may be expected unless the plastic zone gradient (i.e. the rate of change in the plastic zone size as the crack extends) is small. This gradient will be small if the initial crack tip plastic zone size is very small relative to the specimen dimensions. Considering the WOL specimen geometry, the relationship between K_{app} and normalized crack position (a/W) is fixed (e.g., equation 1) as long as the specimen dimensions remain proportional. Because the magnitude of r_p does not depend on specimen size, the gradient in r_p with actual (non-normalized) crack extension will be a function of specimen size. This can be visualized using Figure 29; decreasing W, for example, would not change the size of the circles (r_p), but would decrease the spacing between them leading to a stronger influence of deformation history. Thus, K_R *vs* Δa may be elevated as W decreases, leading to larger measured values of K_{THa}.

Increasing K_{app} will result in a similar elevation of the K_R *vs* Δa curve. For a fixed displacement specimen, the load (and therefore K) must approach zero as the crack approaches the back face of the specimen. For a given initial crack position, the rate of change of K_{app} with actual crack extension, and therefore the rate of change of r_p and K_R, will be steeper for larger initial values of K_{app}. The effect of changing the initial value of K_{app} is shown schematically in Figure 29 (a) and (b), where the amount of overlap of the circles indicates the influence of deformation history as the crack propagates.

No experiments were performed using different size WOL specimens from the same material, so a specimen size effect on K_{THa} cannot be directly confirmed; however the results of Loginow and Phelps were produced from somewhat larger specimens with the W dimension likely closer to 75 mm [13]. It is expected that measurements from the larger WOL specimens would yield lower values of K_{THa} relative to measurements from specimens in this current study

and that this difference should be most pronounced for steels with lower yield strength. At least some of the differences in measured thresholds shown in Figure 25 and discussed in section 4.1 that could not be accounted for solely by the different K solutions may be due to this difference in specimen size. The largest difference between threshold measurements in this study and those reported by Loginow and Phelps was observed for steels with the lowest yield strength while closer agreement was found for higher strength steels. This observation is also consistent with the above described effect of specimen size on plastic zone gradient and the associated K_R *vs* Δa relationship.

An influence of K_{app} on K_{THa} was observed from the results in this study. A plot of K_{app} versus K_{THa} (Figure 31) reveals that K_{THa} increases with increasing K_{app} and that this trend is magnified among the lower strength steels. Variations in K_{app} led to differences in K_{THa} that were as great as 25%. This difference cannot be accounted for by systematic variations in the distance of the arrested crack tip from the back face of the specimen since the use of chevron notched specimens shortened the final crack arrest position (Figure 13), but did not significantly affect the relationship between K_{app} and K_{THa}. Rather, this relationship between K_{app} and K_{THa} is consistent with the postulated relationship between K_R *vs* Δa and the plastic zone gradient.

4.4 Crack growth rate measurements

Crack growth rates of the various low alloy steels tested at constant displacement spanned a range of nearly four orders of magnitude with the faster rates corresponding to higher strength steels with lower values of K_{THa} (Figure 16). All of the steels exhibited a transition from stage II to stage I crack growth behavior; this transition period occurred over a relatively narrow range of K for the steels with yield strength of 900 MPa or greater. The lower strength steels appear to exhibit K-dependant stage II behavior, however plotting da/dt versus K for those specimens with the largest values of K_{app} (Figure 32) suggests that *all the steels may in fact exhibit a K-independent region of stage II when K_{app} is large enough*.

The interpretation of plots of da/dt versus K generally assumes fracture mechanics similitude can be applied to crack growth rate [30]. In other words, for the given environment, equal crack growth rates are always expected for equal stress intensity factors. Rising load experiments using hydrogen pre-charged low alloy steel specimens [111] and low alloy steels in stress

corrosion cracking conditions [110] have shown that cracks can propagate while load is actively increasing but arrest quickly after loading is interrupted and either constant load [110] or constant displacement [111] is maintained. This behavior is not consistent with the general view that equal crack growth rates will always be observed for equal stress intensity factors, however it is consistent with the rising R-curve behavior observed for the similar steels tested in this study (Figure 18); the R-curve suggests that crack extension requires an increasing magnitude of K for continued propagation. Considering that K_{THa} and K_{THi}^{*} appear to be strongly influenced by plastic strain history (as discussed in the preceding sections) it seems reasonable to suggest that the crack growth rate curves may also be dependant on plastic strain history, and thus may not be indicative of the crack growth rates which may be observed for a crack in a structure containing a different strain history.

The arrows in Figure 32 show values of K_{THi}^{*} for each steel. Since all of the specimens from the SA372 grade L and SA 372 grade J (783 MPa) exhibited crack extension, a lower bound for K_{THi}^{*} could not be found, thus the arrows represent an upper bound for K_{THi}^{*}. A very strong correlation exists between K_{THi}^{*} and the limit of K-independent crack growth rate. This correlation has not been explained, however it may present an interesting topic for further research.

4.5 K_{JH} measurements

For all of the low alloy steels tested, K_{JH} measured under rising displacement was less than K_{THa} measured under fixed displacement. The difference between K_{JH} and K_{THa} increased as yield strength decreased (Figure 19), however the same general trend of fracture thresholds in hydrogen gas decreasing with increasing yield strength was maintained for both test methods.

Fracture threshold measurements made under rising displacement conditions in hydrogen gas have been shown to yield non-conservative values ($K_{rising\ disp} > K_{const\ disp}$) when loading rates are too fast. Clark and Landes [16] measured threshold values for a 4340 steel with a yield strength of 1235 MPa in 0.55 MPa H_2 gas using both rising load and constant displacement methods and found that when the applied loading rate was relatively fast, thresholds measured using rising load experiments were larger than fixed displacement crack arrest thresholds. When the loading rate was reduced sufficiently, the two methods yielded the same threshold. Similar results were reported for a lower strength X42 linepipe steel by Gutierrez-Solana and Elices [99] in 4 MPa

hydrogen gas as well as for a low alloy steel with yield strength of 693 MPa under cathodic hydrogen charging potentials by Dietzel *et al* [100].

Sufficiently slow loading rates are necessary to ensure conservative values are measured for environment-assisted cracking thresholds from rising load experiments otherwise kinetic limitations on the uptake of hydrogen into the specimen may affect the measured threshold value. A relatively simple approach for determining an appropriate loading rate has been suggested by Mayville *et al* [101]. They determined that the loading rate for a displacement controlled test suitable for environment-assisted cracking, $\dot{\delta}_{EAC}$ can be determined by

$$\dot{\delta}_{EAC} = (\dot{a}_{EAC} / \dot{a}_{air})\dot{\delta}_{air} \quad (13)$$

where $\dot{\delta}_{air}$ and $\dot{a}_{air}$ are the displacement rate and crack growth rate (i.e., da/dt) in air (or in an inert environment) and $\dot{a}_{EAC}$ is the environment-assisted crack growth rate. The crack growth rates must first be determined for environment-assisted cracking ($\dot{a}_{EAC}$) using sustained load cracking methods and from rising load tests in air ($\dot{a}_{air}$). In addition to validation by Mayville *et al*, this method of determining loading rate has also been demonstrated to be viable for AISI 4340 steel in seawater by Dietzel [102]. It was modified slightly by adding a safety factor multiplier of 0.5 to the right side of equation (13) and incorporated into ISO 7539-9, "Corrosion of metals and alloys -- Stress corrosion testing -- Part 9: Preparation and use of pre-cracked specimens for tests under rising load or rising displacement" [103]. This method, as presented in ISO 7539-9, would suggest loading rates of approximately 0.02 mm/min for the SA 372 grade J steels tested in this study, which is comparable to the 0.051 mm/min rate that was used. This method represented in ISO 7539-9 appears to provide a good starting point for selecting displacement rates for measuring K_{JH} in hydrogen gas. Until more data are available, additional tests performed at faster and slower loading rates should also be conducted to ensure that conservative values are attained.

Consideration should also be given to the possibility that loading rates which are too slow could lead to increasing values of K_{JH} if oxygen impurities in the hydrogen gas enable oxide growth on the crack surfaces that impede hydrogen uptake. Such a trend has not been demonstrated in gaseous hydrogen, however this repassivation phenomenon has been observed during rising displacement fracture threshold testing in aqueous stress corrosion cracking environments (e.g. [104]) and there is reason to believe that even small concentrations of oxygen

could lead to hydrogen-impeding oxide films on steel, as was discussed in section 4.3.1. J-Integral tests performed on a low alloy steel in gaseous hydrogen at pressure of 9 MPa and with additions of 10 and 150 vppm oxygen resulted in corresponding increases of the R-curve [105]. While only one displacement rate was used in that study (0.18 mm/min), it would be interesting to explore whether a rate effect at lower loading rates depends on oxygen content.

All of the rising load tests from this study were conducted under monotonically increasing displacement at 0.051 mm/min (~3 MPa $m^{1/2}$/min) with the exception of one of the DOT-3AAX specimens which was tested at 0.0051 mm/min. Therefore, only two data points are available for comparing the effect of loading rate. The two values for K_{JH} from these two tests were 52 and 53 MPa $m^{1/2}$ at loading rates of 0.051 and 0.0051 mm/min, respectively. These two K_{JH} values are essentially equal, demonstrating that hydrogen transport into the active crack tip process zone is not limited at the faster loading rate. Data generated on C-Mn steels of similar or lower yield strength by Xu [106], Gutierrez-Solana [99] and San Marchi [107] from tests under rising load conditions over a similar range of loading rates (0.1 to 10 MPa $m^{1/2}$/min) did not reveal any notable dependency of K_{JH} on loading rate. These data are plotted with the data from the current study and the data generated by Clark [16] using a high strength steel in Figure 33. A rate dependency is observed only for the high strength steel tested by Clark, which is easily rationalized by considering that those results were generated at much lower hydrogen pressures, where hydrogen uptake kinetics are more sensitive to pressure.

Rising load fracture threshold measurements (concurrent loading and hydrogen exposure) yield lower values than constant displacement tests (sequential loading and hydrogen exposure) for low alloy steels which fail by strain-controlled fracture mechanisms. Extending the discussion from section 4.3.2, the results of the rising load fracture experiments demonstrate the importance of concurrent straining and hydrogen exposure. The need for active straining in the hydrogen environment has been observed by Gangloff in comparing data from hydrogen precharged specimens tested using both constant displacement and rising load methods; steels with yield strength less than about 1000 MPa exhibited K_{THa} values which were larger than rising load thresholds [1]. Many studies of stress corrosion cracking have also reported the need for concurrent straining and exposure to the corrosive environment, particularly for lower strength materials, e.g. [102,108,109,110].

The rising R-curve suggests continually increasing load is needed for crack propagation. Other studies on rising load tests on hydrogen precharged specimens [111] and on low alloy steels in oxygenated water [109] have interrupted the test and found little or no continued crack growth. In the latter case this was demonstrated with the specimen interrupted and held at constant *load*, so load relaxation cannot account for the lack of continued crack extension. This observation corroborates the influence of crack tip deformation history on sustained-load crack arrest thresholds; crack extension will only occur while the applied stress intensity factor is greater than the resistance curve (Figure 30). During a rising load test under displacement control, the applied stress intensity factor and the resistance curve are equal after each increment of crack extension.

5 CLOSURE

Fracture mechanics provides a robust method for design of damage tolerant structures, however the application of data measured from laboratory specimens to engineered structures requires that similitude is maintained between specimen and structure with regard to both environmental and mechanical crack tip conditions. Lower strength, low alloy steels exhibit relatively high fracture thresholds and strain-controlled fracture modes when tested in 103 MPa hydrogen gas, and thus the plastic strain history at the crack tip must be considered with respect to fracture mechanics similitude. Available data suggest that most hydrogen-related failures of low alloy steel pressure vessels occurs during, or immediately following, filling of the vessel [112]. Hydrogen gas storage vessels, pipelines, etc are susceptible to subcritical crack growth during pressurization in which any existing crack is subjected to an increasing stress intensity factor while concurrently exposed to hydrogen gas. Use of constant displacement specimens, in which the load is applied prior to hydrogen exposure, will violate assumptions of similitude (e.g., crack tip strain history relative to hydrogen exposure history) with the intended structural application and should not be expected to yield conservative results. We contend that constant displacement test methods will yield conservative results only when the deformation associated with the crack propagation history has an insignificant contribution to the crack arrest threshold, a condition that is most likely to be encountered only for high strength steels that fail via intergranular fracture. Reliable and conservative measurement of fracture thresholds in lower strength and/or high toughness materials will most often necessitate rising load experiments. Elastic-plastic fracture measurements, such as the J-integral method, enable substantially smaller specimen sizes and therefore are of greater practical use for lower strength steels.

Rising load fracture threshold measurements will exhibit a dependency on the applied loading rate, and tests conducted at rates which are too fast will yield non-conservative results. A method for estimating the appropriate loading rate has been provided in ISO 7539-9 and appears to work reasonably well in high pressure hydrogen gas; however, multiple loading rates should still be explored to ensure a lower bound of fracture threshold has been identified.

6 CONCLUSIONS

- Hydrogen assisted fracture in commercially produced low alloy pressure vessel steels with yield strengths between 641 and 1053 MPa occurs via strain controlled fracture mechanisms in hydrogen gas with pressures up to 103 MPa. Gaseous hydrogen reduces the fracture resistance, implying that the critical accumulated fracture strain for a specimen exposed to hydrogen, ε^*_H, is reduced relative to that for a specimen which is not exposed to hydrogen, ε^*.
- Sub-critical crack extension will occur in constant-displacement fracture threshold tests only once the accumulated fracture strain in hydrogen, ε^*_H, has been achieved. If the fixed displacement is applied in an inert environment prior to hydrogen exposure, additional strain in hydrogen must accumulate to induce hydrogen assisted fracture. Crack-tip creep is enhanced by hydrogen and is responsible for additional, hydrogen-activated crack-tip strain accumulation, ε_H, leading to hydrogen-assisted fracture at ε^*_H .
- Strain accumulated at the crack tip prior to hydrogen exposure does not contribute significantly to attaining ε^*_H, however larger applied stress intensity factors lead to greater hydrogen-activated crack-tip strains in constant-displacement fracture threshold tests. Therefore, the apparent threshold stress intensity factor for crack initiation in a constant displacement specimen, K_{THi}^*, is a measure of the minimum stress intensity factor that is required for the accumulated crack-tip strain in hydrogen to exceed the critical strain: $\varepsilon_H > \varepsilon^*_H$.
- Strain accumulated ahead of a propagating crack is less than that ahead of a stationary crack due to non-proportional plastic deformation in the active plastic zone and elastic unloading in the crack wake. As a result, propagating cracks in constant-displacement fracture threshold tests arrest at larger threshold stress intensity factors, K_{THa}, relative to the threshold stress intensity factor at which a stationary crack will begin to propagate, K_{JH}, in rising-displacement fracture threshold tests.
- For steels with yield strengths between 600 and 700 MPa, K_{THi}^* measurements are as much as two times as large as measurements of K_{THa}, which in turn are about two times the value of K_{JH}.

7 REFERENCES

1 RP Gangloff "Hydrogen assisted cracking of high strength alloys" in *Comprehensive Structural Integrity*, Vol. 6, I. Milne, R.O. Ritchie and B. Karihaloo, Eds., Elsevier Science, New York, NY, (2003), pp. 31-101.

2 AW Thompson and IM Bernstein "The role of metallurgical variables in hydrogen assisted environmental fracture" in *Hydrogen-Assisted Environmental Fracture*. in: Fontana MG, Staehle RW, editors. Advances in Corrosion science and technology, vol. 7. New York: Plenum Publishing Corporation; 1980. p. 53–175.

3 HK Birnbaum, IM Roberston, P Sofronis, D Teter "Mechanisms of hydrogen related fracture – a review. In: Magnin T, editor. Proceedings of the Second International Conference on Corrosion–Deformation Interactions, CDI 96. Cambridge: Woodhead Publishing Limited; 1997.

4 IM Bernstein, "The role of hydrogen in the embrittlement of iron and steel" *Materials Science and Engineering* Vol. 6, 1970 pp. 1-19.

5 JP Hirth "Effects of hydrogen on the properties of iron and steel" *Met Trans* Vol 11A, 1980, pp. 861-890.

6 RA Oriani "Hydrogen embrittlement of steels" *Ann. Rev. Mater. Sci.* Vol. 8, 1978, pp. 327-357.

7 HG Nelson, "Testing for hydrogen environment embrittlement: Primary and secondary influences" in *Hydrogen Enbrittlement Testing, ASTM STP 543*, ASTM, Philadelphia PA, 1974, pp. 152-169.

8 P McIntyre, "Hydrogen Effects in high strength steels" in *Hydrogen Degradation in High Strength Steels*, RA Oriani, JP Hirth and M Smialowski, Eds., Noyes Publications, 1985, pp. 763-798.

9 HJ Cialone and JH Holbrook "Sensitivity of steels to degradation in gaseous hydrogen" *Hydrogen Embrittlement: Prevention and Control, ASTM STP 962* L Raymond, Ed., American Society for Testing and Materials, Philadelphia, 1988, pp. 134-152.

10 GG Hancock and HH Johnson "Hydrogen, Oxygen and subcritical crack growth in a high-strength steel" *Transactions of the Metallurgical Society of AIME*, Vol. 236, 1966, pp. 513-516.

11 ASTM E1681-03 "Standard test method for determining threshold stress intensity factor for environment-assisted cracking of metallic materials" *Annual Book of ASTM Standards*, ASTM International, West Conshohocken, PA.

12 MW Perra “Sustained-load cracking of austenitic steels in gaseous hydrogen” *Environmental Degradation of Engineering Materials in Hydrogen*, MR Louthan, RP McNitt, and RD Sisson, Eds., VPI Press, Blacksburg, VA 1981 pp. 321-333.

13 AW Loginow and EH Phelps “Steels for seamless hydrogen pressure vessels”, *Corrosion*, Vol, 31, No. 11, 1975, pp. 404-412.

14 ASME Section VIII, Division 3 Code, 2007 Edition, Article KD-10, “Special requirements for vessels in high pressure gaseous hydrogen delivery and storage service”, ASME, New York, NY

15 MD Rana, GB Rawls, JR Sims, and E Upitis “Technical basis and application of new rules on fracture control of high pressure hydrogen vessel in ASME Section VII, Division 3 Code” Proceedigs of PVP2007, PVP2007-26023, 2007.

16 WG Clark and JD Landes, “An Evaluation of Rising Load K_{Iscc} Testing”, in *Stress Corrosion – New Approaches, ASTM STP 610* , ASTM, Philadelphia PA, 1976, pp. 108-127.

17 EIGA Doc 100/03/E “Hydrogen Cylinders and Transport Vessels” European Industrial Gases Association, Brussels, Belgium, 2003.

18 CJ McMahon Jr, X Liu, J Kameda, and MJ Morgan “Recent Observations of Hydrogen – Induced Cracking of High-Strength Steels” in *Effects of Hydrogen on Materials*, Proceedings of the 2008 International Hydrogen Conference, B Somerday, P Sofronis, and R Jones, Eds., ASM International, Material Park, OH, 2009, p. 46-53.

19 ASTM E1820-09 “Standard test method for measurement of fracture toughness” *Annual Book of ASTM Standards*, ASTM International, West Conshohoken, PA

20 LA James “Compliance Relationships for the WOL Specimen Revisited,” prepared for ASTM Working Groups E24.01.05 and E24.04.02 July 1989.

21 CN Freed and JM Krafft “Effect of Side Grooving on Measurements of Fracture Toughness,” *Journal of Materials*, Vol. 1, No. 4, 1966, pp. 770-790.

22 BK Neale, DA Curry, G Green, JR Haigh, and KN Akhurst “A Procedure for the Determination of the Fracture Resistance of Ductile Steels”, Report TPRD/B0495/84, Central Electricity Generating Board, 1984.

23 ANSI/NACE Standard TM0177-96, Item No. 21212, “Standard Test Method: Laboratory Testing of Metals for Resistance to Sulfide Stress Cracking and Stress Corrosion Cracking in H_2S Environments” NACE International, Houston TX, 1996.

24 WB Lisagor "Influence of Precracked Specimen Configuration and Starting Stress Intensity on the Stress Corrosion Cracking of 4340 Steel," in *Environment-Assisted Fracture: Evaluation and Comparison of Test Methods, ASTM STP 821*, 1984, pp. 80-97.

25 ASTM E1737-96 "Standard test method for J-integral characterization of fracture toughness" *Annual Book of ASTM Standards*, ASTM International, West Conshohocken, PA.

26 A Saxena and SJ Hudak "Review and extension of compliance information for common crack growth specimens" *International Journal of Fracture*, Vol. 14' 1978, pp. 453-468.

27 JD Landes, "J calculation from front face displacement measurement on a compact specimen" *Int J Fracture*, Vol. 16, 1980, pp. R183-R186.

28 HKS. Abaqus Version 6.7, Theory Manual. Providence, RI: Hibbit, Karlsson, and Sorensen, 2007.

29 GR Irwin, "Fracture Mechanics", In Goodier, J. N. and Hoff, N. J. editors, *Structural Mechanics*, *Proceedings of the First Symposium of Naval Structural Mechanics*, Pergamon Press, pp. 557 – 594, 1960.

30 TL Anderson, *Fracture Mechanics Fundamentals and Applications*, Third Edition, Taylor and Francis, Boca Raton FL, 2005.

31 ASTM E399-06 "Standard test method for linear-elastic plane-strain fracture toughness K_{Ic} of metallic materials" *Annual Book of ASTM Standards*, ASTM International, West Conshohocken, PA.

32 JA Joyce and RL Tregoning, "Development of consistent size criteria for ASTM combined fracture mechanics standards" in *Fatigue and Fracture Mechanics: 30th Volume, ASTM STP 1360*, ASTM, West Conshohocken PA, 2000, pp. 357-376.

33 HG Nelson and DP Williams "Qualitative observations of hydrogen-induced, slow crack growth in a low alloy steel" in *Stress Corrosion Cracking and Hydrogen Embrittlement of Iron Based Alloys* Eds. RW Staehle, J Hochmann, RD McCright, and JE Slater NACE 1977 pp.390-404.

34 RP Gangloff and RP Wei "Gaseous hydrogen embrittlement of high strength steels" *Met. Trans.* Vol. 8A 1977 pp. 1043-1053.

35 Y Takeda and CJ McMahon Jr. "Strain controlled vs stress controlled hydrogen induced fracture in a quenched and tempered steel", *Metallurgical Transactions* Vol. 12A, 1981, pp. 1255-1266.

36 AJ DeArdom, MJ Hua, KG Cho and CI Garcia "On strength of microalloyed steels: an interpretive review" *Materials Science and Technology* Vol. 25 (2009) pp. 1074-1082.

37 SR Novak and ST Rolfe "Modified WOL specimen for K_{Iscc} environmental testing" *Journal of Materials*, Vol. 4, 1969, pp. 701-728.

38 WK Wilson "Stress intensity factors for deep cracks in bending and compact tension specimens" *Eng. Fract. Mech*, Vol. 2, 1970, pp. 169-171.

39 CD Beachem and RMN Pelloux, "Electron fractography – A tool for the study of micromechanisms of fracturing processes", in *Fracture Toughness Testing and its Applications* (STP 381), pp. 210-244, ASTM, Philadelphia PA, 1965.

40 *Electron Fractography*, *ASTM STP 436*, CD Beachem, Ed., ASTM International, Philadelphia PA, 1967.

41 JE Costa and AW Thompson, "Effect of hydrogen on fracture behavior of a quenched and tempered medium-carbon steel", *Met Trans A*, Vol. 12A, 1981, pp. 761-771.

42 M Gao, M Lu, and RP Wei, "Crack paths and hydrogen-assisted crack growth response in AISI Steel" *Met Trans A*, Vol. 15A, 1984, pp. 735-746.

43 TD Lee, T Goldenberg, and JP Hirth, "Effect of hydrogen on fracture of U-notched bend specimens of spheroidized AISI 1095 steel" *Met Trans A*, Vol. 10A, 1979, pp. 199-208.

44 CD Beachem, "Electron fractographic studies of mechanical processes in metals", *Journal of Basic Engineering (Trans ASME Series D)*, Vol. 8887, 1965, pp. 299-306.

45 HC Burghard, Jr., and NS Stoloff, "Cleavage phenomena and topographic features" in *Electron Fractography, ASTM STP 436*, ASTM, Philadelphia PA, 1968, pp. 32-58.

46 AW Thompson "Fractography and its role in fracture interpretation" *Fatigue Fract. Engng. Mater. Struct.*, Vol. 19, 1996, pp. 1307-1316.

47 CD Beachem, "Orientation of cleavage facets in tempered martensite (quasi-cleavage) by single surface trace analysis", *Met Trans*, Vol. 4, 1973, pp.1999-2000.

48 YH Kim and JW Morris, Jr., "The nature of quasicleavage fracture in tempered 5.5Ni steel after hydrogen charging", *Met Trans A*, Vol. 14A, 1983, pp. 1883-1888.

49 RM Horn and RO Ritchie, "Mechanisms of tempered martensite embrittlement in low alloy steels" *Met Trans A*, Vol. 9A, 1978, pp. 1039-1053.

50 Ming Gao and RP Wei, “Quasi-cleavage and martensite habit plane”, *Acta Metall.* Vol. 32, 1984, pp. 2115-2124.

51 CJ McMahon, Jr “Effects of hydrogen on plastic flow and fracture in iron and steel” in *Hydrogen Effects in Metals* IM Bernstein and AW Thompson, Eds. The Metallurgical Society of AIME, Warrendale, PA 1981 pp. 219-234.

52 F Nakasato and IM Bernstein “Crystallographic and fractographic studies of hydrogen-induced cracking in purified iron and iron-silicon alloys” *Metallurgical transactions* Vol. 9A, 1978, pp. 1317-1326.

53 AW Thompson and JC Chesnutt “Identification of a fracture mode: The tearing topography surface” *Met Trans A*, Vol. 10A, 1979, pp. 1193-1196.

54 WJ Mills “Effect of microstructural variations in the tensile and fracture properties of alloy 718 welds” in *Superalloys 718, 625, 706 and Various Derivatives*, ed. EA Loria, TMS, Pittsburgh PA, 1994. pp. 845-858.

55 GT Gray, III, JC Williams and AW Thompson “Roughness-induced crack closure: An explanation for microstructurally sensitive fatigue crack growth”, *Met Tans A*, Vol. 14A, 1983, pp. 421-433.

56 AW Thompson and IM Bernstein, “The role of plastic fracture processes in hydrogen embrittlement” In *Advances in Research on the Strength and Fracture of Materials*, Vol. 2A, Proceedings of the Fourth International Conference on Fracture Ed. DMR Taplin, Permagon Press, 1977, pp. 249-254.

57 RO Ritchie, WL Server, and RA Wullert “Critical fracture stress and fracture strain models for the prediction of lower and upper shelf toughness in nuclear pressure vessel steels” *Met Trans A*, Vol. 10A, 1979, pp. 1557-1570.

58 RO Ritchie and AW Thompson, “On macroscopic and microscopic analyses for crack initiation and crack growth toughness in ductile alloys” *Metall. Trans. A*, Vol. 16A, 1985, pp. 233-248.

59 KA Nibur, DF Bahr, BP Somerday, “Hydrogen effects on dislocation activity in austenitic stainless steel”, *Acta Mater.*, Vol. 54, 2006, pp. 2677-2684.

60 IM Robertson, “The effect of hydrogen on dislocation dynamics”, *Engineering Fracture Mechanics*, Vol. 64, 1999, pp. 649-673.

61 K.A. Nibur, B.P. Somerday, D.K. Balch, and C. San Marchi “The role of localized deformation in hydrogen-assisted crack propagation in 21Cr-6Ni-9Mn stainless steel” *Acta Mater.*, 2009, vol. 57, pp. 3795-3809.

62 FA McClintock “Plasticity aspects of fracture” in *Fracture an Advanced Treatise* Vol. III Engineering Fundamentals and Environmental Effects, Academic Press, London, 1971, pp. 47-225.

63 D Kwon and RJ Asaro “A study of void nucleation, growth and coalescence in spheroidized 1518 steel” *Met Trans*, Vol. 21A, 1990, pp. 117-134.

64 H Deve, S Harren, C McCullough, and RJ Asaro “Micro and macroscopic aspects of shear band formation in internally nitrided single crystals of Fe-Ti-Mn alloys” *Acta Metall.*, Vol. 36, 1988, pp. 341-365.

65 S Lee, DY Lee, and RJ Asaro “Correlation of microstructure and tempered martensite embrittlement in two 4340 steels” *Met Trans*¸Vol. 20A, 1989, pp. 1089-1103.

66 NF Mott and FRN Nabarro “Dislocation theory and transient creep” in Physical Society Bristol Conference Report, 1948, pp.1-19.

67 AH Cottrell “Thermally activated plastic glide” *Phil. Mag. Letters*, Vol. 82, 2002, pp. 65-70.

68 MM Hall, Jr. “Thermally activated low temperature creep and primary water stress corrosion cracking of NiCrFe alloys” report prepared for Alloy 600 Experts Meeting sponsored by the Electric Power Research Institute, 1993.

69 TH Courtney *Mechanical Behavior of Materials*, McGraw-Hill Publishing Company, New York, 1990, pp. 268-271.

70 CG Park, KS Shin, J Nagakawa and M Meshii “Effect of cathodic charging on creep and tesile deformation of pure iron” *Scripta Met.* Vol. 14, 1980, pp. 279-284.

71 A Barnoush, M Zamanzade, and H Vehoff, “Direct observation of hydrogen-enhanced plasticity in super duplex stainless steel by means of in situ electrochemical methods”, *Scripta Metall.* Vol. 62, 2010, pp. 242-245.

72 P Sofronis and HK Birnbaum “Mechanics of the hydrogen-dislocation-impurity interactions-I. Increasing shear modulus” *J Mech Phys Solids*, Vol. 43, pp. 49-90, 1995.

73 W-Y Chu, C-M Hsiao, and S-Q Li, “Hydrogen induced delayed plasticity and cracking” *Scripta Metall.* Vol. 13, 1979, pp. 1063-1068.

74 W-Y Chu, S-Q Li, C-M Haiao and J-Z Tien, “Mechanism of stress corrosion cracking of steels in H_2S”, *Corrosion*, Vol. 36, 1980, pp. 475-482.

75 RA Oriani and PH Josephic "Testing of the decohesion theory of hydrogen-induced crack propagation" *Scripta Metallurgica* Vol. 6, 1972, pp. 681-688.

76 TJ Vink, JM Der Kinderen, OLJ Gijzeman, JW Geus, and JM Van Zoest, "Oxidation of Fe(100): Reconstruction and oxide growth at elevated temperatures" *Applied Surface Science*, Vol. 26, 1986, pp. 357-366.

77 T Smith and LW Crane "Adsorption of Oxygen on Steel", *Transactions of the Metallurgical Society of AIME*, Vol. 236, April 1966, pp. 513-516.

78 PB Sewell, SD Stockbridge and M Cohen, "An electrometric and electron diffraction study of air-formed oxide films on iron", *Journal of the Electrochemical Society*, Vol. 108, 1961, pp. 933-941.

79 AM Brass, L Nevot, M Aucouturier, and R Berneron, "A contribution to the characterization of the surface oxide layers grown in natural conditions on chromium-molybdenum steels" *Corrosion Science*, Vol. 24, 1984, pp. 49-60.

80 PCJ Graat, MAJ Somers, AM Vredenberg, and EJ Mittemeijer, "On the initial oxidation of iron: Quantification of growth kinetics of the couple-currents approach", *J. Appl. Phys.*, Vol. 82, 1997, pp.1416-1422.

81 RM Rieck, A Atrens and IO Smith "The role of crack tip strain rate in the stress corrosion cracking of high strength steels in water" *Metallurgical Transactions A*, Vol. 20A, 1989, pp. 889-895.

82 A Oehlert and A Atrens "Room temperature creep of high strength steels" *Acta Metall. Mater.*, Vol. 42, 1994, pp. 1493-1508.

83 S Weng, Y Zhang, and W Chen, "Room temperature creep and strain-rate dependent stress-strain behavior of pipeline steels" *Journal of Materials Science*, Vol. 36, 2001, pp. 1931-1938.

84 SK Putatunda and V Venugopal "Influence of overload plastic zone size on stress corrosion crack growth behavior of a low alloy steel in 3.0% NaCl solution" *Journal of Testing and Evaluation*, Vol. 18, 1990 pp. 182-190.

85 RP Wei, SR Novak and DP Williams "Some important considerations in the development of stress corrosion cracking test methods" *Materials Research and Standards* Vol. 12 (1972) pp. 25-30.

86 RP Wei and SR Novak "Interlaboratory evaluation of K_{ISCC} and da/dt determination procedures for high-strength steels" *Journal of Testing and Evaluation*, Vol. 15 (1987), pp.38-75.

87 CF Barth and EA Steigerwald, “Evaluation of hydrogen embrittlement mechanisms” *Met Trans*, Vol. 1, 1970, pp. 3451-3455.

88 P Doig and GT Jones “A model for the initiation of hydrogen embrittlement cracking at notches in gaseous hydrogen environments” *Met Trans A*, Vol. 8A, 1977, pp. 1993-1998.

89 S Singh and C Altstetter “Effects of hydrogen concentration on slow crack growth in stainless steels” *Met Trans A*, Vol. 13A, 1982, pp. 1799-1808.

90 NR Moody, RE Stoltz and MW Perra “The effect of hydrogen on fracture toughness of the Fe-Ni-Co superalloy IN903” *Met Trans A*, Vol. 18A, 1987, pp. 1469-1482.

91 M Dadfarnia, BP Somerday, P Sofronis, IM Robertson,and D Stalheim, “Interaction of hydrogen transport and material elastoplasticity in pipeline steels”, *J. Pressure Vessel Technology*, Vol. 131, 2009, pp. 041404-1-12.

92 KA Nibur, BP Somerday, C SanMarchi and DK Balch “Measurement of sustained-load cracking thresholds for steels in hydrogen delivery and storage” in Proceedings of 2008 ASME Pressure Vessels and Piping Division Conference, PVP2008-61298, 2008.

93 V Vitek, “Plane strain stress intensity factors for branched cracks”, *International Journal of Fracture*, Vol. 13, 1977, pp. 481-501.

94 JW Hutchinson. “On steady quasi-static crack growth”, Harvard University Rep. Division of Applied Sciences, DEAP S-8, April 1974.

95 JR Rice and EP Sorensen “Continuing craci-tip deformation and fracture for plane-strain crack growth in elastic-plastic solids,” *J. Mech. Phys. Solids*, Vol. 26, 1978, pp. 163-186.

96 B Cotterell and AG Atkins “A review of J and I integrals and their implications for crack growth resistance and toughness in ductile fracture” *International Journal of Fracture*, Vol. 87, 1996, pp. 357-372.

97 TL Sham “A finite-element analysis of quasi-static crack growth in an elastic perfectly-plastic solid” Sc.M. Thesis, Brown University, 1979.

98 WJ Drugan, JR Rice and T-L Sham, “Asymptotic analysis of growing plane strain tensile cracks in elastic-ideally plastic solids” *J. Mech. Phys. Solids*, Vol. 30, 1982, pp. 447-473.

99 F Gutierrez-Solana and M Elices, “High-Pressure Hydrogen Behavior of a Pipeline Steel,” in *Current Solutions to Hydrogen Problems in Steels*, CG Interrante and GM Pressouyre, Eds., American Society for Metals, Metals Park, OH, 1976, pp. 690-694.

100 W Dietzel and K-H Schwalbe, "Application of the rising displacement test to SCC investigations", in *Slow Strain Rate Testing for the Evaluation of Environmentally Induced Cracking: Research and Engineering Applications, ASTM STP 1210*, RD Kane, Ed., ASTM, Philadelphia PA, 1993, pp. 134-148.

101 RA Mayville, TJ Warren and PD Hilton, "Determination of the loading rate needed to obtain environmentally assisted cracking in rising load tests", *Journal of Testing and Evaluation*, Vol. 17, 1989, pp. 203-211.

102 W Dietzel and J Mueller-Roos, "Experience with rising load/rising displacement stress corrosion cracking testing" *Materials Science*, Vol. 37, 2001, pp. 264-271.

103 ISO Standard 7539-9:2003 "Corrosion of metals and alloys -- Stress corrosion testing -- Part 9: Preparation and use of pre-cracked specimens for tests under rising load or rising displacement", 2003.

104 G Abramson, JT Evans, and RN Parkins, "Investigation of stress corrosion crack growth in Mg Alloys using J-integral estimations", *Met Trans A*, Vol. 16A, 1985, pp. 101-108.

105 K Kussmaul, P Deimel, H Fischer and E Sattler, "Fracture mechanical behaviour of the steel 15 MnNi 6 3 in argon and in high pressure hydrogen gas with admixtures of oxygen", *Int. J. Hydrogen Energy*, Vol. 23, 1998, pp. 577-582.

106 K Xu, "Properties of linepipe steels in high pressure hydrogen" presentation given at ASTM G1 H2 Workshop, Reno NV, May 17, 2005.

107 C SanMarchi unpublished results, 2009.

108 RN Parkins, "Development of strain-rate testing and its implications", in *Stress Corrosion Cracking – The Slow Strain-Rate Technique, ASTM STP 665*, GM Ugiansky and JH Payer, Eds., ASTM, Philadelphia PA, 1979, pp. 5-25.

109 HP Seifert and S Ritter, "Stress corrosion cracking of low-alloy reactor pressure vessel steels under boiling water reactor conditions" *Journal of Nuclear Materials*, Vol. 372, 2008, pp. 114-131.

110 J Heldt and HP Seifert, "Stress corrosion cracking of low-alloy reactor-pressure-vessel steels in oxygenated, high-temperature water", *Nuclear Engineering and Design*, Vol. 206, 2001, pp. 57-89.

111 RP Gangloff "Science-based prognosis to manage structural alloy performance in hydrogen" in *Effects of Hydrogen on Materials*, B Somerday, P Sofronis and R Jones, Eds., ASM International, Materials Park, OH, 2009, pp. 1-21.

112 R Irani, “Hydrogen embrittlement: How it was resolved in the 1980’s” presentation from ISO TC58/WG7, Gas Cylinder Compatibility, Atlanta GA, 29 Sept. 2008.

8 TABLES

Table 1 Yield strength and composition of the alloys tested.

Alloy	Yield strength (MPa)	C	Cr	Cu	Mo	Ni	Al	Mn	Si	P	S	Fe
DOT-3AAX	607	0.29	0.92	nr	0.19	nr	0.035	0.62	0.28	0.008	0.004	Bal
DOT-3AAX	641	0.30	0.95	nr	0.18	nr	0.030	0.63	0.28	0.008	0.005	Bal
SA372 grade J	641	0.46	0.94	nr	0.18	nr	nr	0.92	0.25	0.011	0.006	Bal
SA372 grade J	717	0.48	0.96	nr	0.18	nr	0.026	0.92	0.30	0.010	0.002	Bal
SA372 grade J	730	0.48	1.01	nr	0.19	nr	nr	0.98	0.27	0.013	0.005	Bal
SA372 grade J	736	0.47	0.96	nr	0.19	nr	0.032	0.92	0.30	0.012	0.003	Bal
SA372 grade J	783	0.49	0.99	nr	0.18	nr	nr	0.93	0.28	0.008	0.004	Bal
SA372 grade L	731	0.4	0.82	0.1	0.26	1.93	0.022	0.75	0.28	0.006	0.007	Bal
SA372 grade L	1053	0.4	0.82	0.1	0.26	1.93	0.022	0.75	0.28	0.006	0.007	Bal
DOT-3T	900 A	0.45	0.97	nr	0.18	nr	0.034	0.86	0.25	0.013	0.006	Bal
DOT-3T	900 B	0.44	0.99	nr	0.18	nr	0.031	0.85	0.26	0.007	0.003	Bal
HY130 400C	~1000	0.10	0.47	nr	0.50	5.12	nr	<0.01	<0.01	0.004	<0.001	Bal
HY130 200C	~1000	0.10	0.47	nr	0.50	5.12	nr	<0.01	<0.01	0.004	<0.001	Bal
HY130	1035	0.10	0.47	nr	0.50	5.12	nr	<0.01	<0.01	0.004	<0.001	Bal

nr = not reported

Table 2 Results from fixed displacement and rising displacement threshold tests.

Tensile Properties				Sustained Load									Rising Load						
Alloy	yield strength (MPa)	tensile strength (MPa)	Charpy energy (J (ft-lbs) @-20F)	id	H_2 gas pressure (MPa)	loading environment	applied disp (mm)	K_{app} (MPa $m^{1/2}$)	K_{TH_a} (MPa $m^{1/2}$)	Incubation time (hours)	final a/w	initial a/w	B (average, mm)	id	J_{IH} (kJ/m^2)	J_{cH} (kJ/m^2)	dJ_H/da ($kJ/m^2/mm$)	K_{IH} (MPa $m^{1/2}$)	loading rate (mm/min)
DOT 3AAX	641	786	na	3	103	Ar	0.86	115	NCP	1168	--	0.552	17.5						
				4	103	Ar	0.97	127	NCP	3864	--	0.558	17.5						
				2	103	Ar	1.09	144	NCP	3864	--	0.556	17.5						
				1	103	Ar	1.23	162	87	~400	0.87	0.552	17.5						
				2	103	Ar	1.35	178	99	5.4	0.86	0.556	17.5						
				3	103	Ar	1.40	185	97	5.1	0.88	0.552	17.5						
				4	103	Ar	1.51	199	110	5	0.87	0.558	17.5						
	607	765	69 (51)	CN4	103	Ar	0.76	162	NCP	161	--	0.318	18.3	101	7.8	11.9	19.5	52	0.051
				CN3	103	Ar	0.89	189	98	2.6	0.685	0.318	18.3	102	7	12.5	25.8	53	0.0051
SA372 grade J	717	852	96 (71)	1	103	Ar	?	49***	NCP	168	-	0.548	22.2						
				2	103	Ar	?	63***	NCP	168	-	0.551	22.2						
				6	103	Ar	?	73***	NCP	168	-	0.553	22.2						
				4	103	Ar	?	80***	NCP	168	-	0.557	22.2						
				3	103	Ar	?	81***	NCP	168	-	0.553	22.2						
				1	103	Ar	0.79	107	NCP	288	-	0.548	22.2						
				2	103	Ar	0.93	125	NCP	288	-	0.551	22.2						
				3	103	Ar	1.02	137	NCP	288	-	0.553	22.2						
				1	103	Ar	1.05	140	93	1015	0.81	0.548	22.2						
				4	103	Ar	1.12	148	108	12	0.77	0.557	22.2						
				2	103	Ar	1.21	160	96	3.7	0.84	0.551	22.2						
				6	103	Ar	1.26	167	109	1.5	0.81	0.553	22.2						
				3	103	Ar	1.34	177	99	na*	0.86	0.553	22.2						
				5	103	Ar	?	na*	na	1.6	0.82	0.558	22.2						
	736	861	94 (69)	7	103	Ar	0.69	94**	ncp	>18,000	--	0.542**	22.2	101	14.1	18.1	19.1	64	0.051
				8	103	Ar	0.76	105**	ncp	>18,000	--	0.539**	22.2	102	7.5	13.3	28.2	55	0.051
				10	103	air	1.17	153	100	62	0.82	0.561	22.2						
				9	103	air	1.33	174	97	1.7	0.87	0.563	22.2						
				CN2	103	Ar	1.04	151	97	1.6	0.78	0.496	22.2						
				CN3	103	Ar	1.02	156	105	1.6	0.73	0.462	22.2						
				CN1	103	Ar	1.19	169	104	5.7	0.81	0.51	22.2						
				CN4	103	Ar	1.02	167††	ncp	672	--	0.428	22.2						
	783	907	57 (66) (@-40F	K236-2C	103	Ar	0.99	131	80	147	0.84	0.552	22.2	K236-2B	6.1	9.6	16.9	47	0.051
				K236-2A	103	Ar	1.14	152	86	40	0.86	0.55	22.2						
				K236-2D	103	air	0.99	132	82	312	0.83	0.548	22.2						
				K236-3A	103	air	1.15	153	77	2.4	0.89	0.552	22.2						
	641	839	49 (36)	K236-1E	103	Ar	1.32	175	ncp	3384	--	0.552	22.2	K236-1C	6.1	10	19.1	48	0.051
				K236-1A	103	Ar	1.50	200	ncp	3384	--	0.546	22.2	K236-1B	9.4	16.3	32.3	61	0.051
	730	870	80 (59)	Y046-1	103	Ar	1.17	157	105	28	0.797	0.544	22.2	Y046-3	9.9	12.8	16.3	54	0.051
				Y046-2	103	Ar	1.30	174	115	4	0.801	0.544	22.2	Y046-4	8	11.5	16.3	51	0.051
DOT-3T	900 A	1001	62 (46)	4	103	Ar	0.53	70	35	85	0.89	0.551	14.0	102	1.5	2	2.1	21	0.051
				2	103	Ar	0.64	84	37	27	0.91	0.551	14.0	103	3.3	4.2	4.4	31	0.051
				3	103	Ar	0.65	86	36	3	0.92	0.549	14.0						
				1	103	Ar	0.89	118	40	0.8	0.95	0.553	14.0						
	900 B	1001	76 (56)	6	41	Ar	0.66	88	43	93	0.89	0.549	14.0						
				5	41	Ar	0.69	91	45	275	0.89	0.553	14.0						
				9	103	Ar	0.38	50**	ncp	>18,000	--	0.56**	14.0						
				7	103	Ar	0.43	58**	ncp	672	--	0.539**	14.0						
				8	103	Ar	0.43	58**	ncp	672	--	0.54**	14.0						
				10	103	Ar	0.46	60**	ncp	>18,000	--	0.557**	14.0						
				12	103	air	0.64	83	31	181	0.94	0.561	14.0						
				11	103	air	0.84	112	50	3	0.91	0.549	14.0						
				CN2	103	Ar	0.38	83	30	3.2	0.84	0.312	14.0						
				CN1	103	Ar	0.43	91	30	3.1	0.88	0.323	14.0						

Table 2. cond.

Tensile Properties					Sustained Load									Rising Load						
Alloy	yield strength (MPa)	tensile strength (MPa)	Charpy energy (J (ft-lbs) @-20F)	id	H_2 gas pressure (MPa)	loading environment	applied disp (mm)	K_{app} (MPa $m^{1/2}$)	K_{THa} (MPa $m^{1/2}$)	Incubation time (hours)	final a/w	initial a/w	B (average, mm)	id	J_{iH} (kJ/m^2)	J_{kH} (kJ/m^2)	dJ_H/da (kJ/m^2/mm)	K_{JH} (MPa $m^{1/2}$)	loading rate (mm/min)	
SA372 grade L	731	873		4	103	Ar	1.02	134	79	4.2	0.846	0.556	22.2							
				1	103	Ar	1.07	143	79	0.2	0.86	0.543	22.2							
				2	103	Ar	1.24	167	85	1.8	0.88	0.545	22.2							
				3	103	Ar	1.40	186	91	0.3	0.89	0.55	22.2							
	1053	1149	60 (44)	4	103	Ar	0.25	34	28	~144	0.689	0.548	22.2	102	0.26	0.86	2.8	14	0.051	
				1	103	Ar	0.48	64	21	1.3	0.95	0.549	22.2							
				3	103	Ar	0.64	85	22	0†	0.97	0.544	22.2							
				2	103	Ar	0.71	95	not meas.	0†	~.99	0.547	22.2							
HY130	1053			as quenched	138	Ar	0.71	98	34	0.7	0.94	0.525	15.2							
	>1000			T200C-1	103	Ar	0.36	41	23	12	0.92	0.747	15.2							
				T200C-2	103	Ar	0.64	95	28	7	0.96	0.562	15.2							
	~1000			T400C	103	Ar	0.74	96	38⁻	7	0.93	0.561	15.2							

* Instrumentation problems resulted in lost measurements

**K_{app} based on measured displacement and estimated precrack length

*** K_{app} calculated from instrumented load tup

† cracks initiated before test pressure was achieved

†† specimen tested with no precrack

+ quench crack through specimen along plane parallel to specimen side

Table 3 Approximate K_{THi}^{*} values for each steel specification.

Alloy	K_{THa} (MPa $m^{1/2}$)	K_{THi}* (MPa $m^{1/2}$)	
DOT-3AAX (641 MPa)	87	153	1.75 K_{THa}
SA 372 grade J (717 MPa)	93	< 140	<1.5 K_{THa}
SA372 grade L (731 MPa)	79	< 134	<1.7 K_{THa}
DOT 3T (900 MPa A)	35	< 70	< 2 K_{THa}
SA372 grade L (1053 MPa)	28	< 34	<1.2 K_{THa}

9 FIGURES

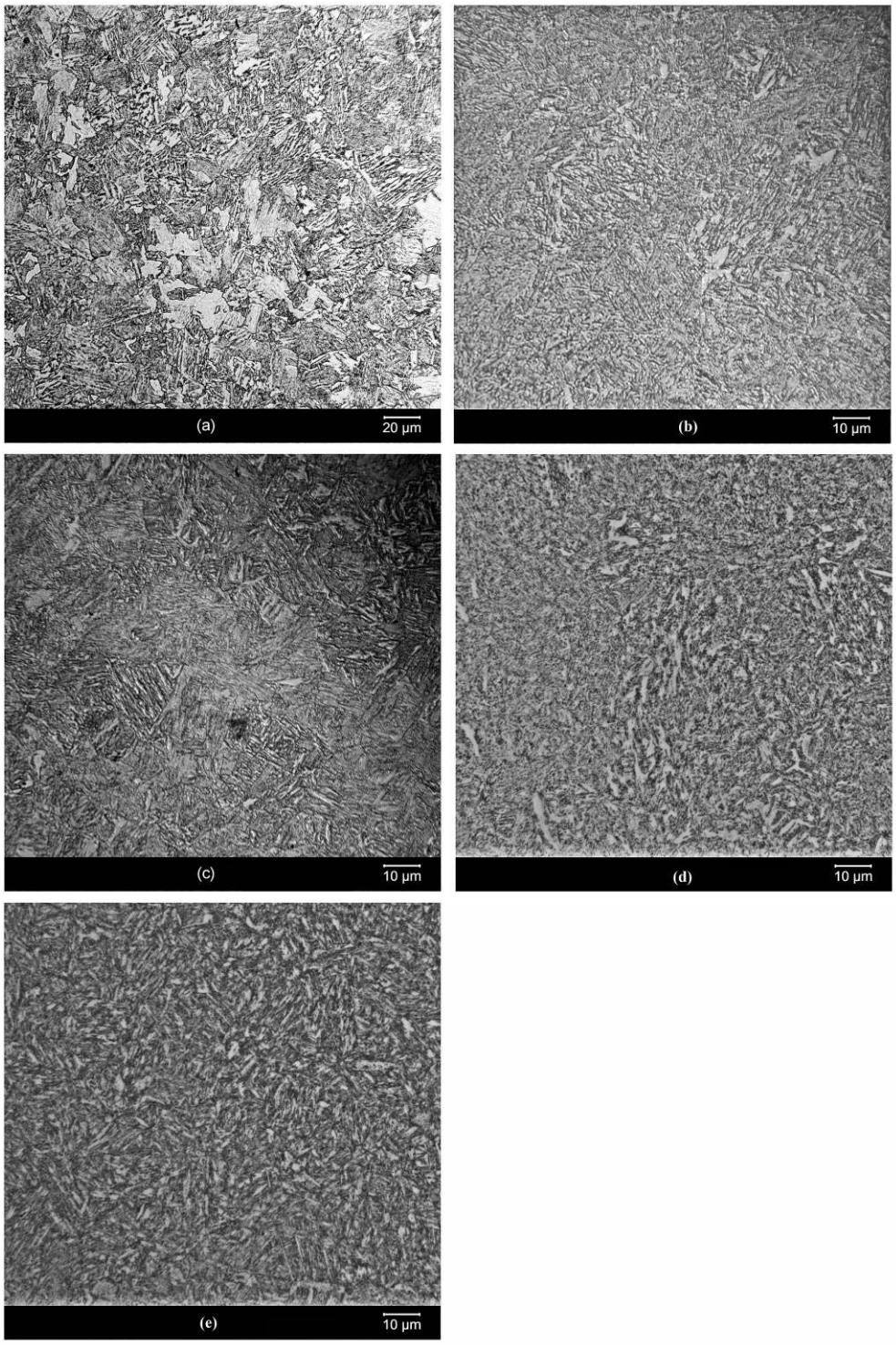

Figure 1 Microstructures of the (a) DOT-3AAX, (b) SA372 grade J (717 MPa), (c) DOT-3T, (d) SA372 grade L (731 MPa) and (e) SA372 grade L (1053 MPa). All specimens etched with Nital showing a surface normal to the radial direction of the original cylindrical product.

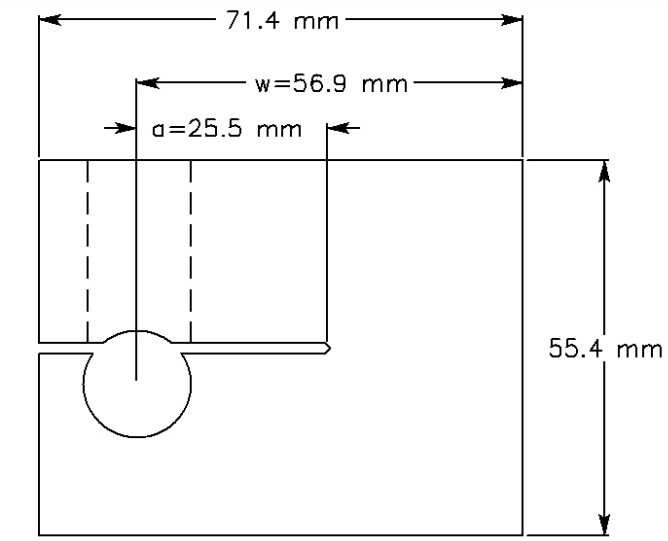

(a)

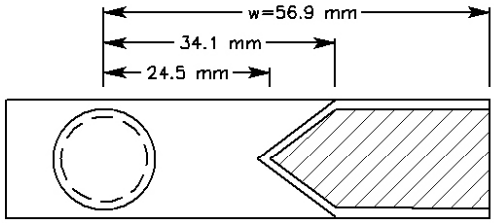

(b)

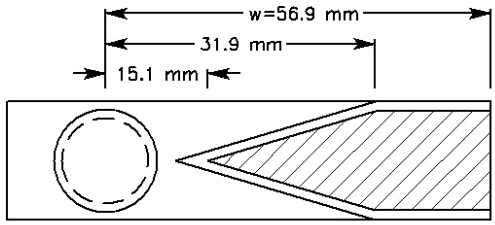

(c)

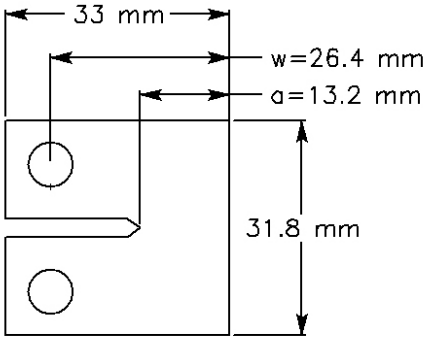

(d)

Figure 2 Specimen drawings showing important dimensions for (a) WOL specimen, (b) chevron notch dimensions for SA372 grade J chevron notched specimens, (c) chevron notch dimensions for the DOT-3T and DOT-3AAX chevron notched specimens, and (d) compact tension specimens.

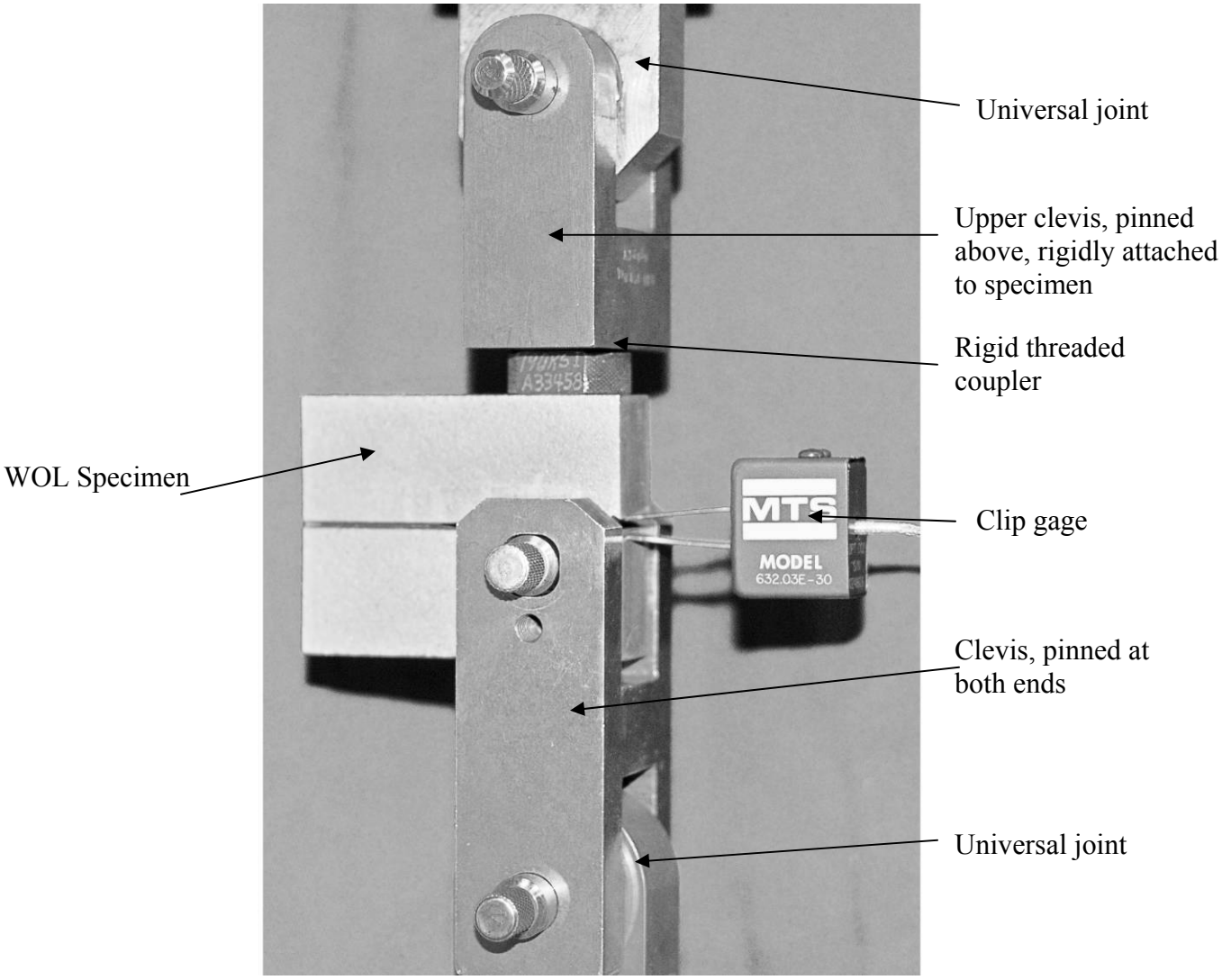

Figure 3 The specimen and the loading fixture used for pre-cracking and initial compliance measurements.

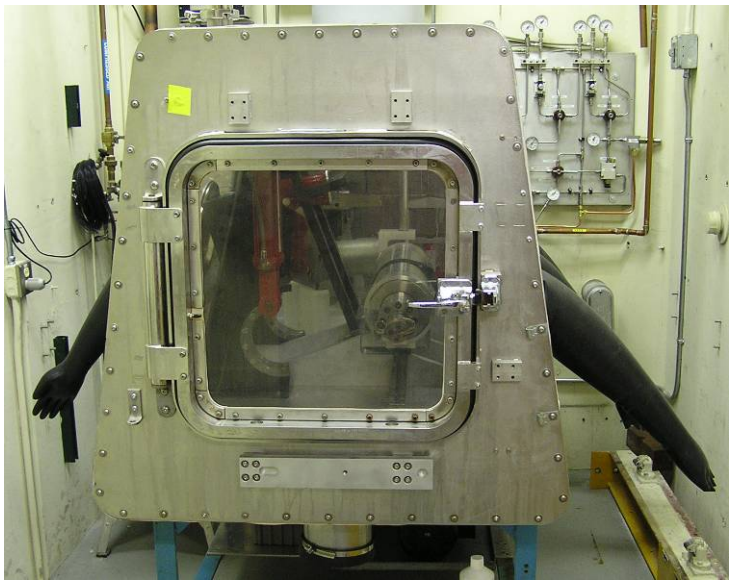

Figure 4 The glovebox which was used for bolt loading WOL specimens in a low oxygen (~1-2vppm) argon environment. The hydraulic manifold (upper right) controlled hydraulic actuators which tightened the loading bolt and the pressure vessel's Bridgman closure nut.

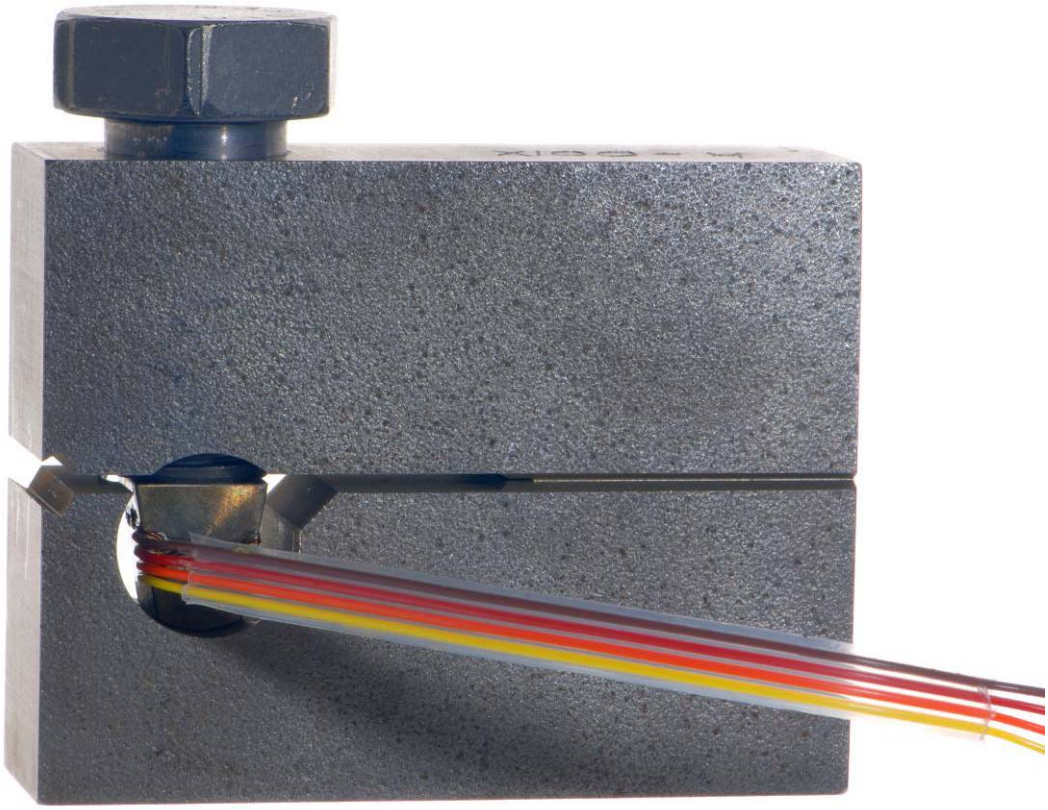

Figure 5 WOL specimen with A-286 loading bolt and strain-gage equipped Cu-Be load tup.

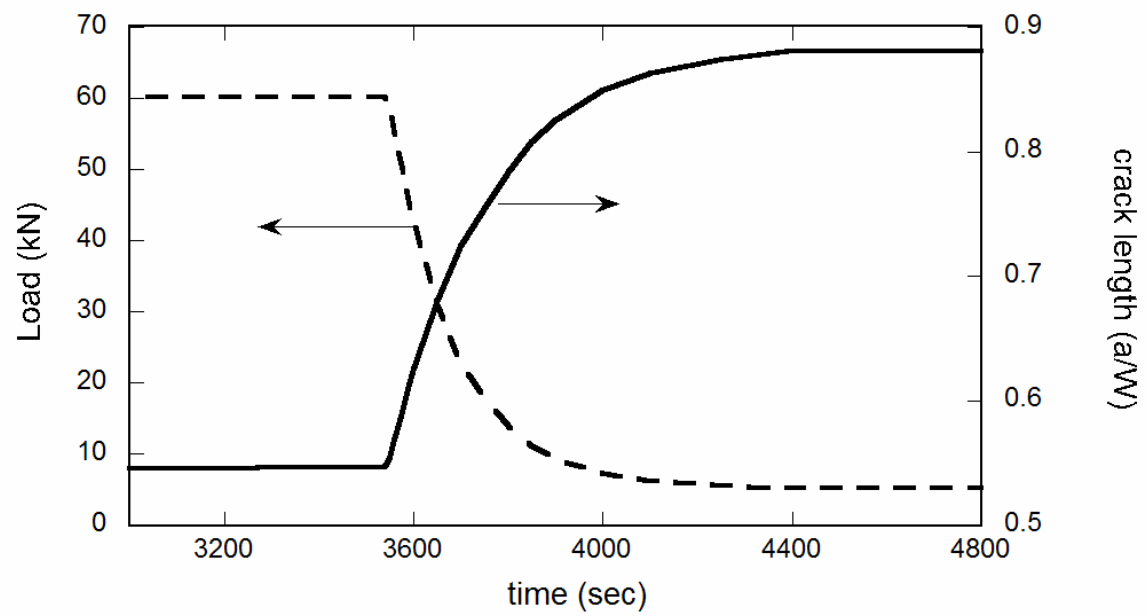

Figure 6 Crack length and load determined from load tup measurements during crack extension of an SA 372 grade L (731 MPa -2) specimen.

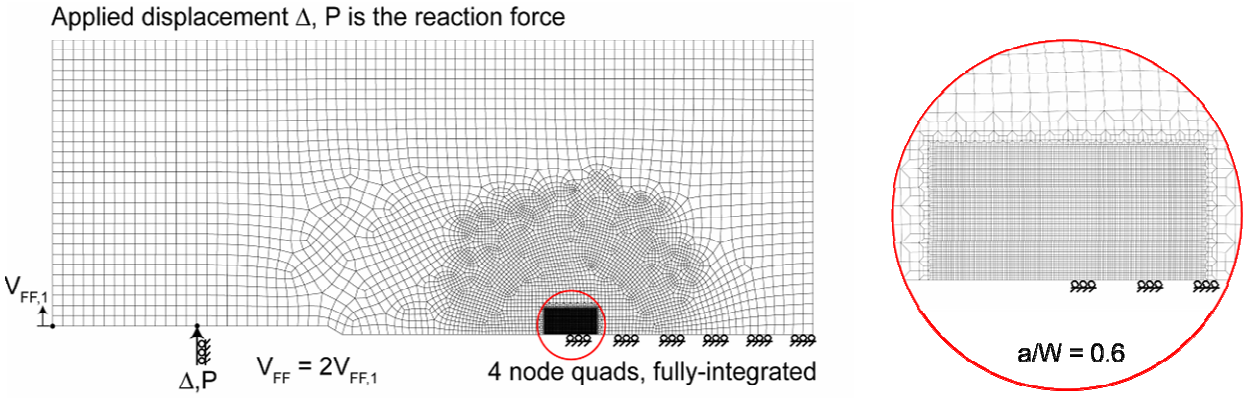

Figure 7 A representative finite element discretization for the symmetric, WOL geometry with a/W = 0.6. A displacement Δ is applied and the reaction force P and front face displacement V_{FF} are output.

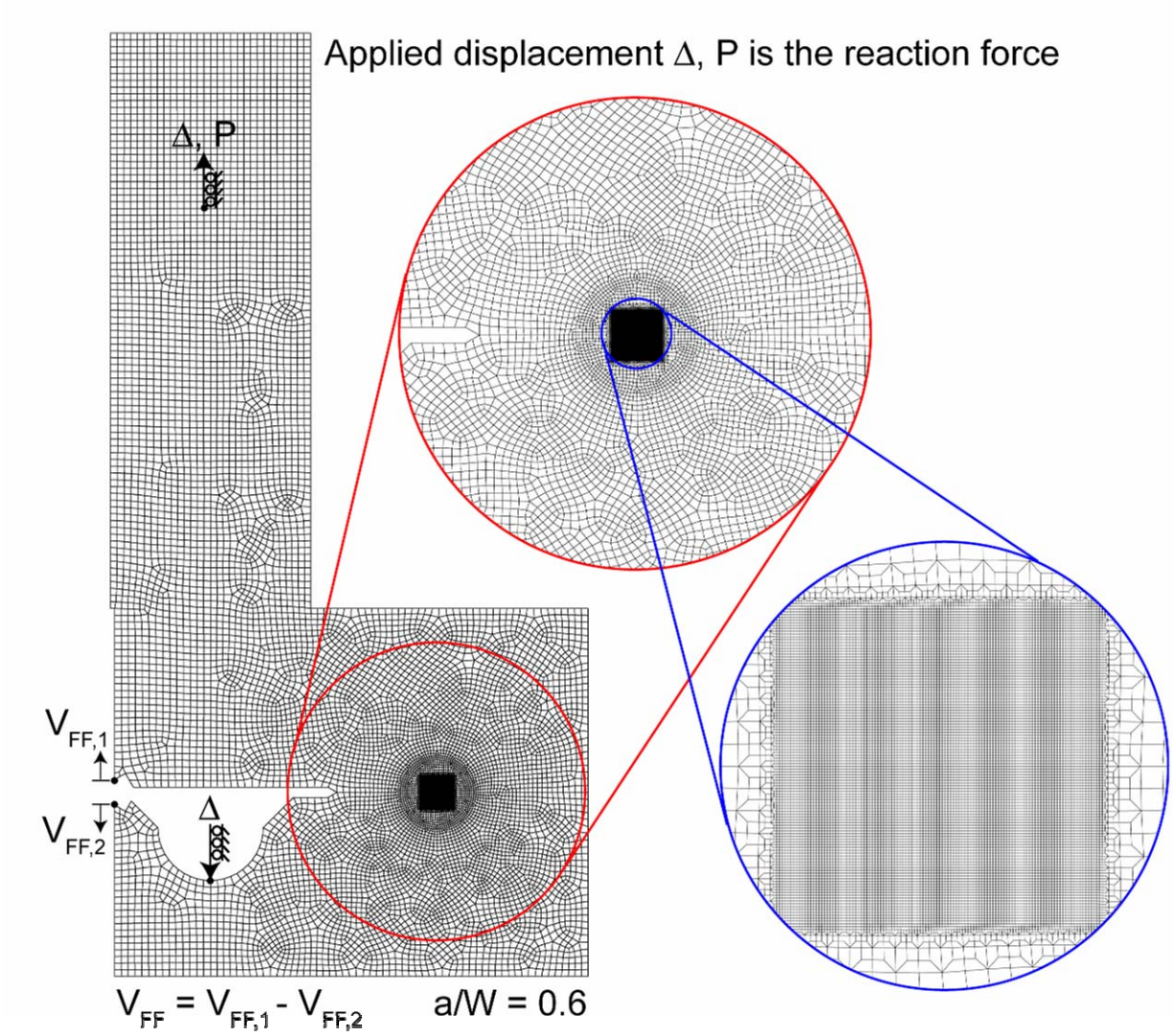

Figure 8 A representative finite element discretization for the geometry that represents the WOL specimen fixtured to a clevis with a/W = 0.6. A displacement Δ is applied and the reaction force P and front face displacement V_{FF} are output.

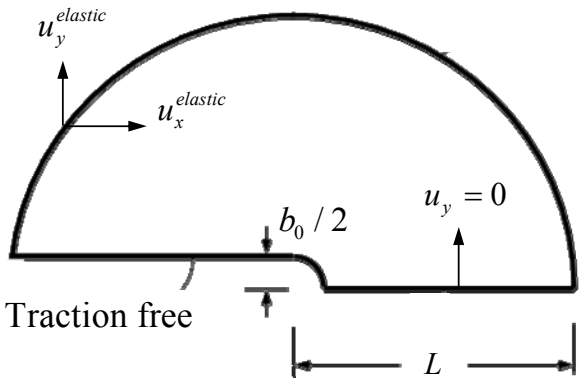

Figure 9 Boundary and loading conditions for the elasto-plastic problem at a blunting crack tip under small scale yielding conditions. The parameter b_0 is the crack opening displacement in the undeformed state and $u_x^{elastic}$ and $u_y^{elastic}$ are the asymptotic displacements of Irwin's singular field [29] in x- and y-directions, respectively.

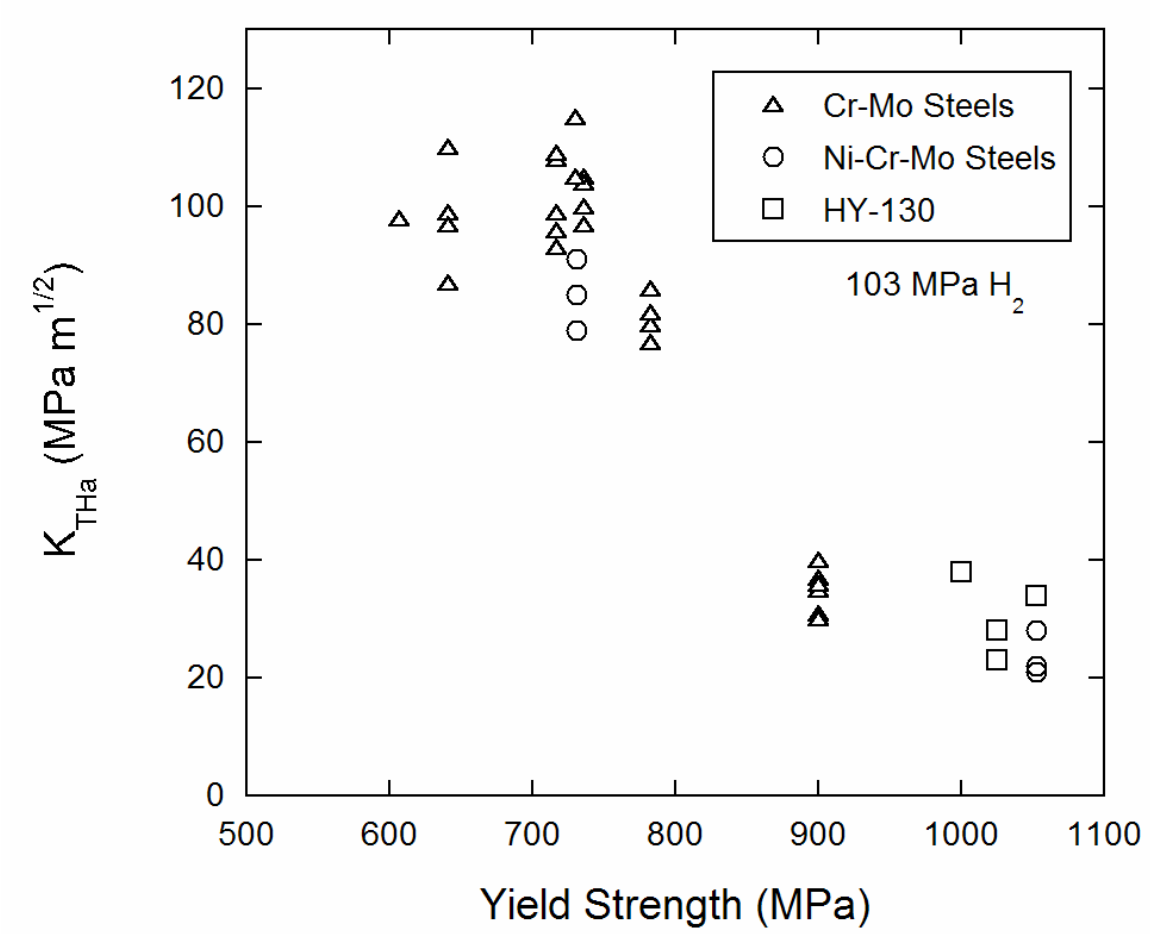

Figure 10 Crack arrest threshold stress intensity factors for all alloys tested in 103 MPa H_2 gas plotted as a function of yield strength.

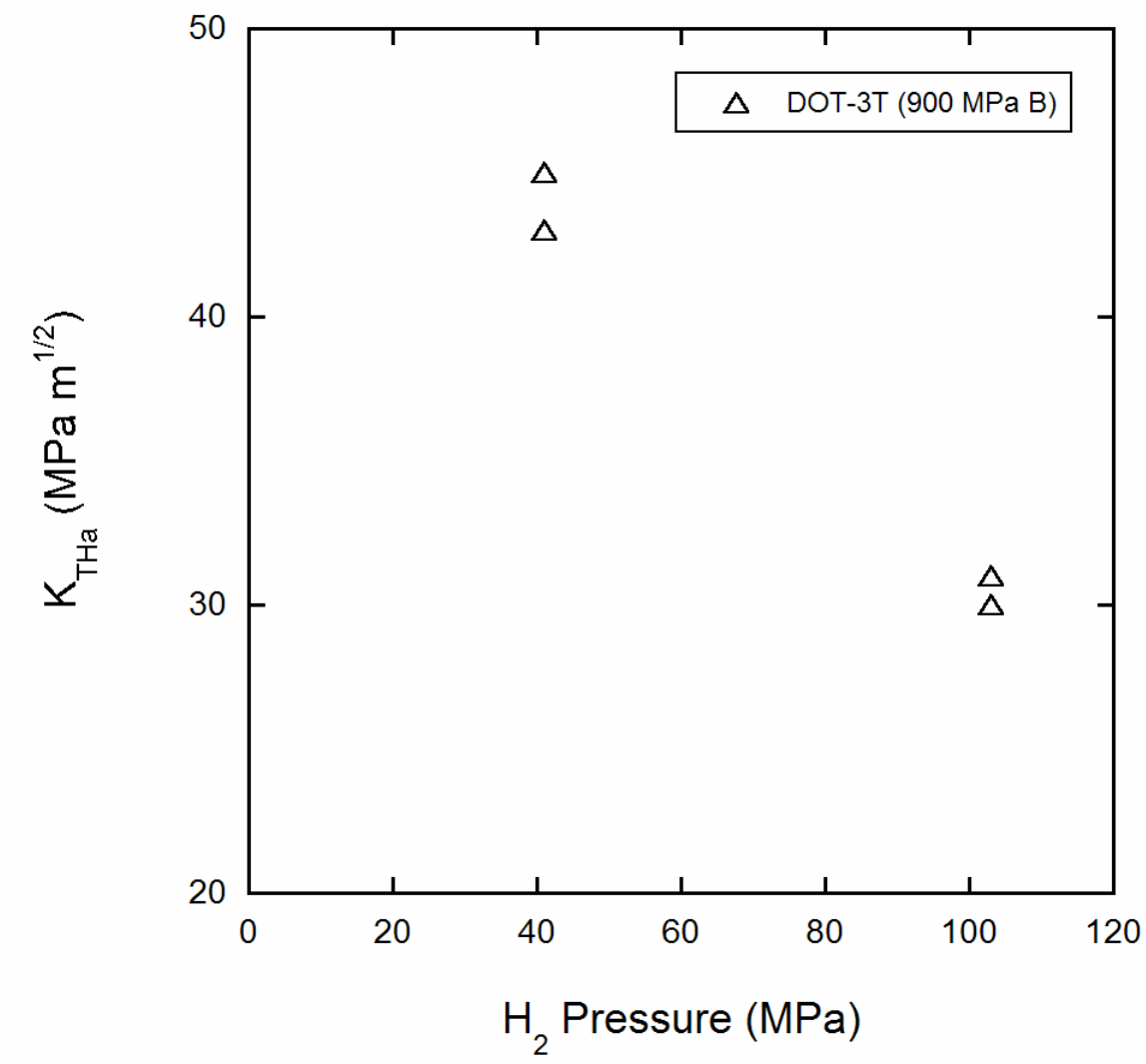

Figure 11 Crack arrest threshold stress intensity factors for DOT-3T tested in 103 and 41 MPa H_2 gas.

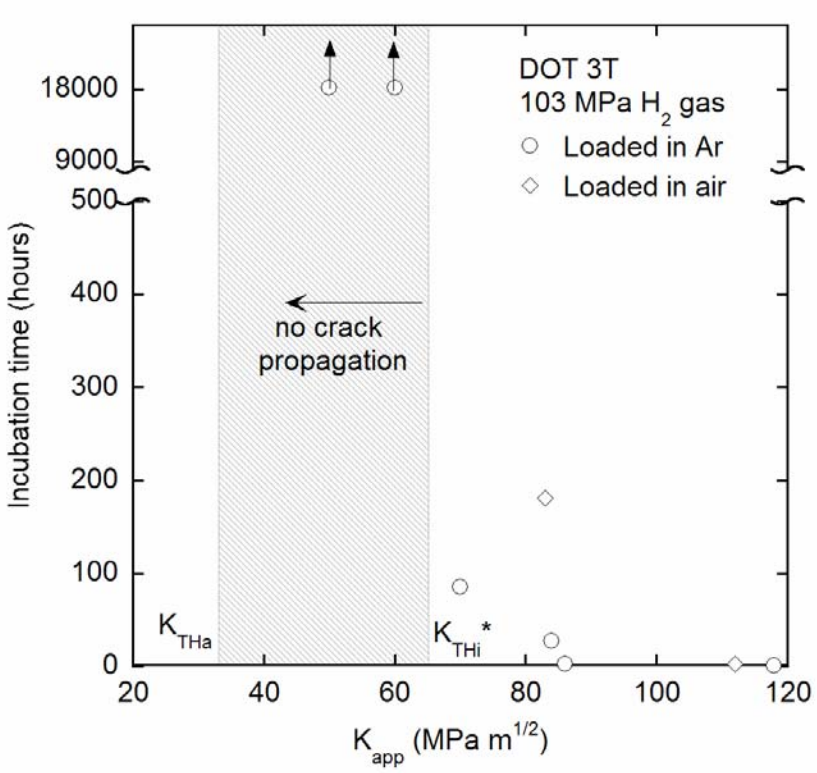

(a)

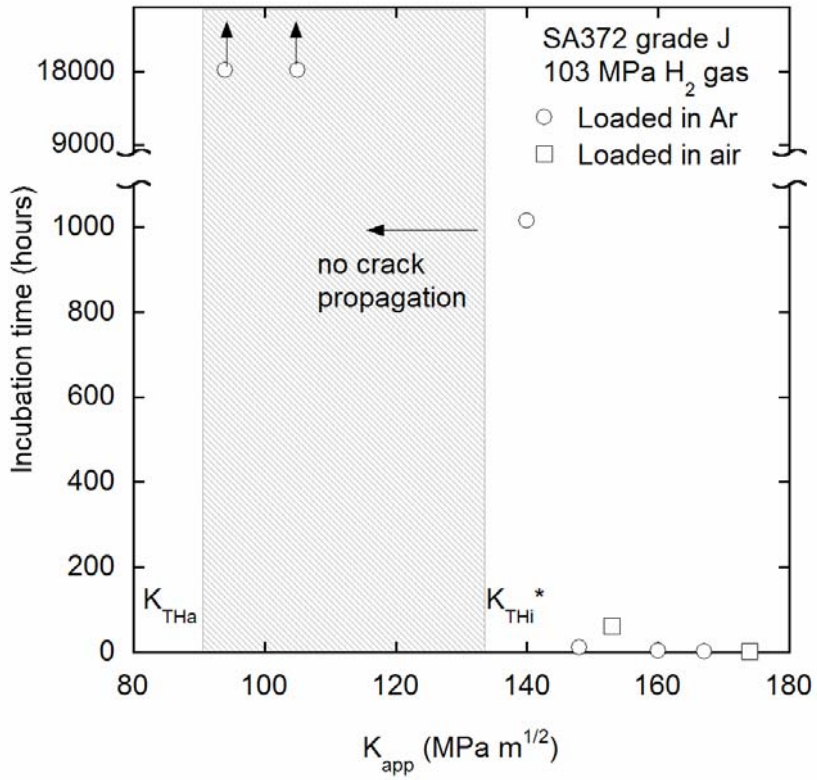

(b)

Figure 12 Plots of incubation time versus K_{app} for (a) DOT-3T and (b) SA372 grade J.

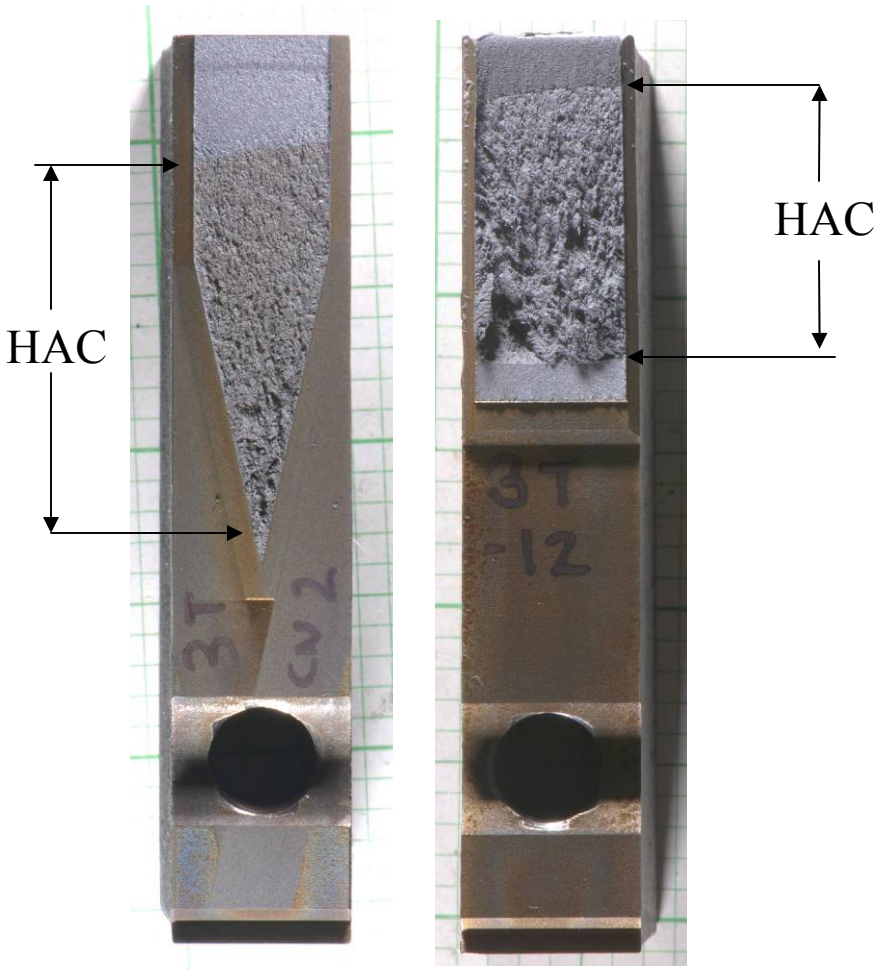

Figure 13 Fractured surfaces of chevron notched and straight notched specimens of DOT-3T 900B. These two specimens (CN2 and 12, respectively) were both loaded to K_{app}= 83 MPa $m^{1/2}$ (though the displacement, V_{FF}, varied) and both yielded very similar measurements of K_{THa} (30 and 31 MPa $m^{1/2}$, respectively).

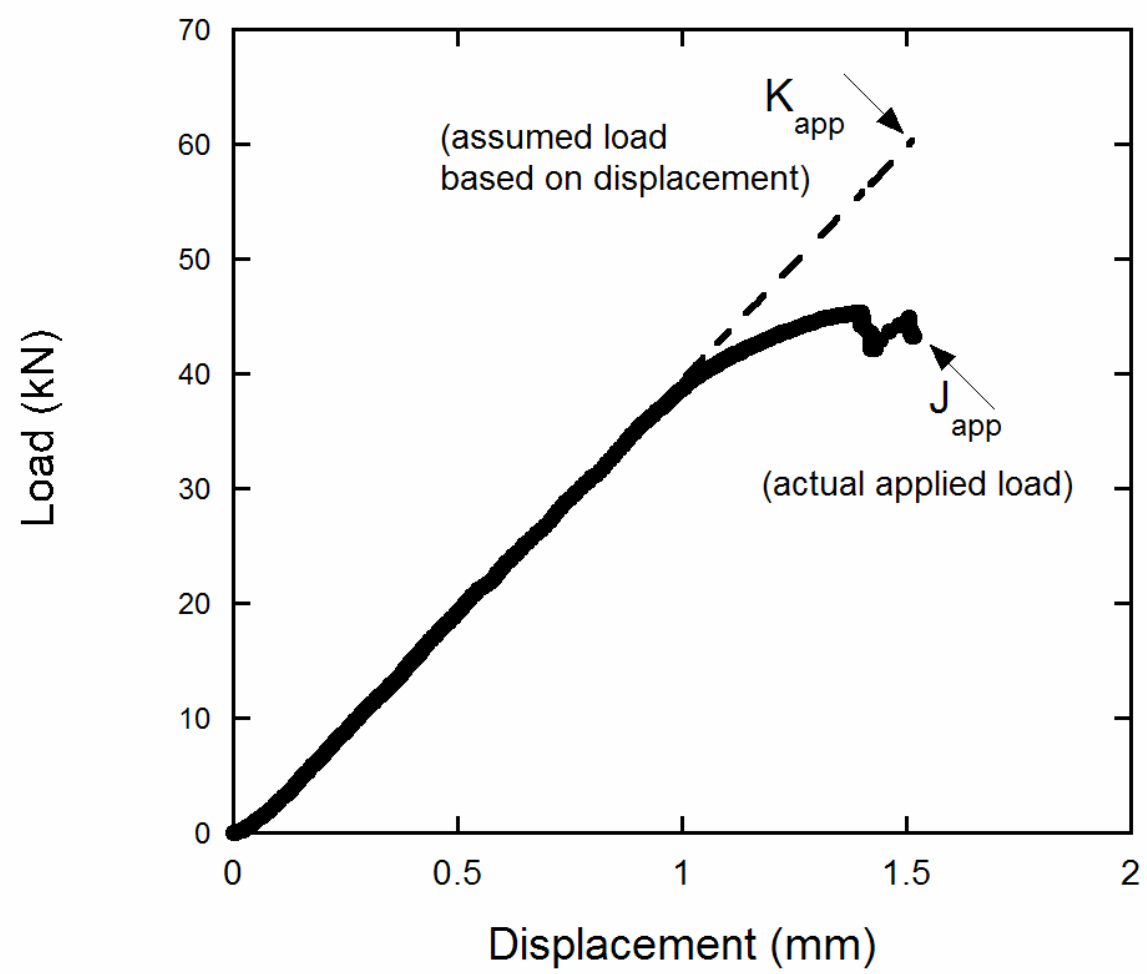

Figure 14 Load versus displacement recorded during load application to DOT-3AAX specimen 4. Dashed line shows the behavior assumed from linear elastic loading assumptions inherent to the calculation of K_{app}, whereas the solid line shows actual applied load which was used to calculate J_{app}. Fortuitously, $K_{app} \sim K_{Japp}$.

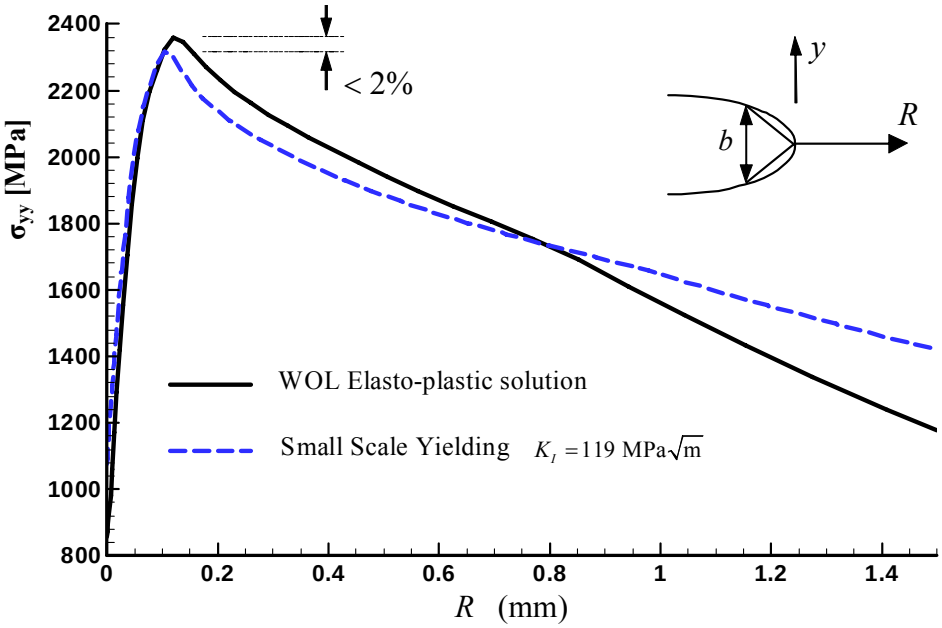

Figure 15 Comparison of the crack tip opening stress , σ_{yy}, on the plane of symmetry ahead of the crack in the WOL specimen with the small scale yielding solution and with the elastic-plastic solution utilizing flow properties representative of the SA372 grade J (717 MPa) steel. The simulation for the WOL specimen assumes the specimen is loaded to a crack opening displacement V_{FF} =1.26 mm and the crack position is at a/W = 0.81.

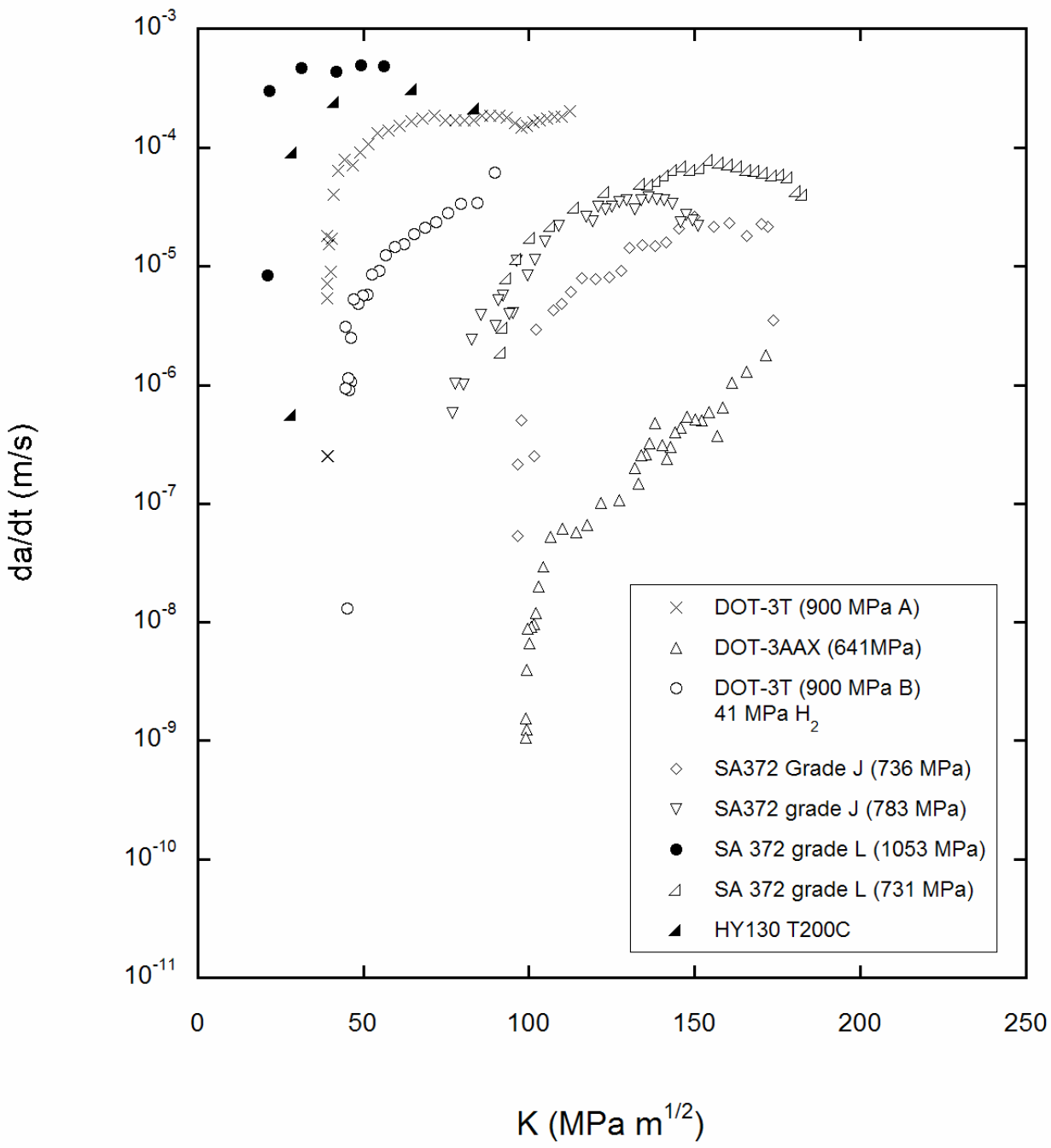

Figure 16 Crack growth rate (da/dt) versus K curves for representative specimens of each of the alloys tested.

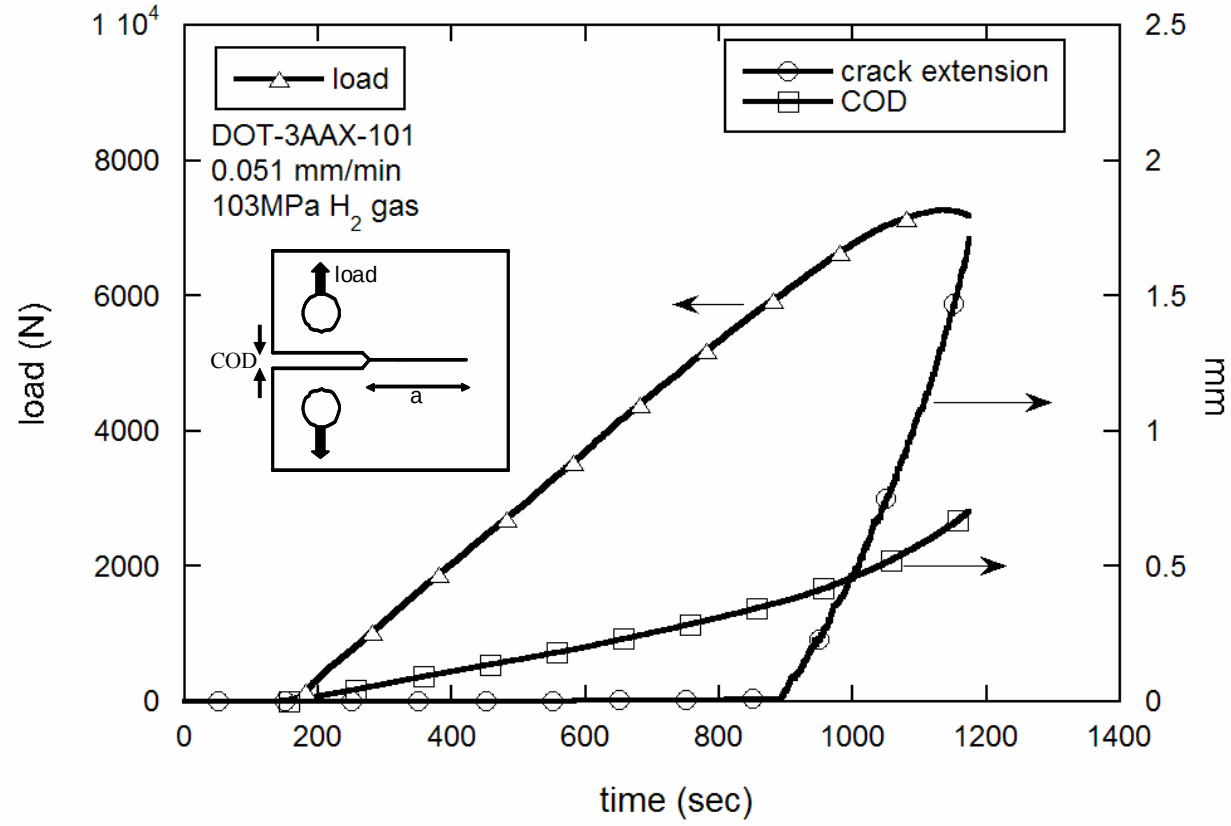

Figure 17 The relationship between load, crack opening displacement and crack extension for the rising displacement experiments is demonstrated by this plot of the data recorded from specimen DOT-3AAX-102.

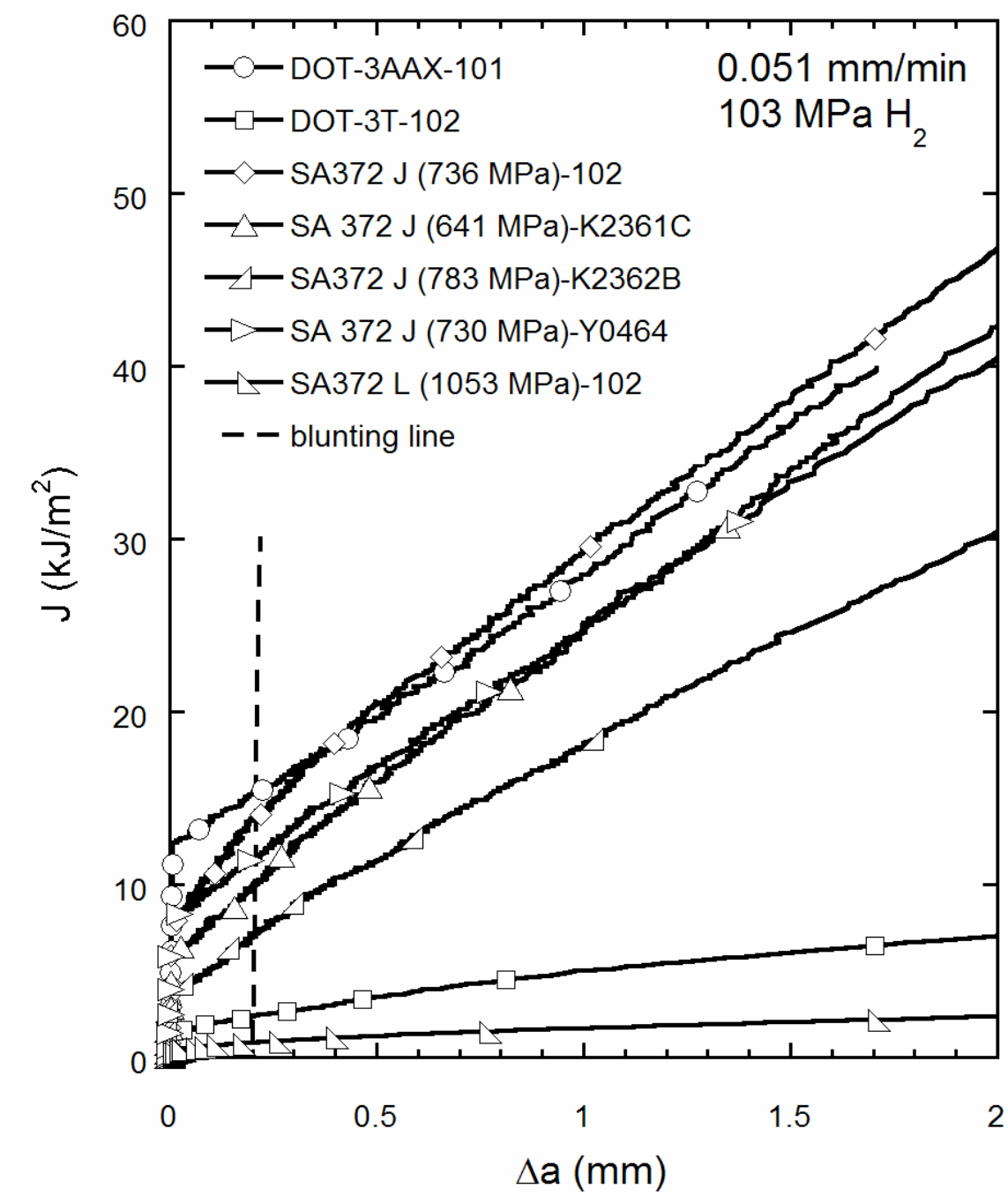

Figure 18 Crack growth resistance curves (R-curves) for representative specimens from each of the alloys tested.

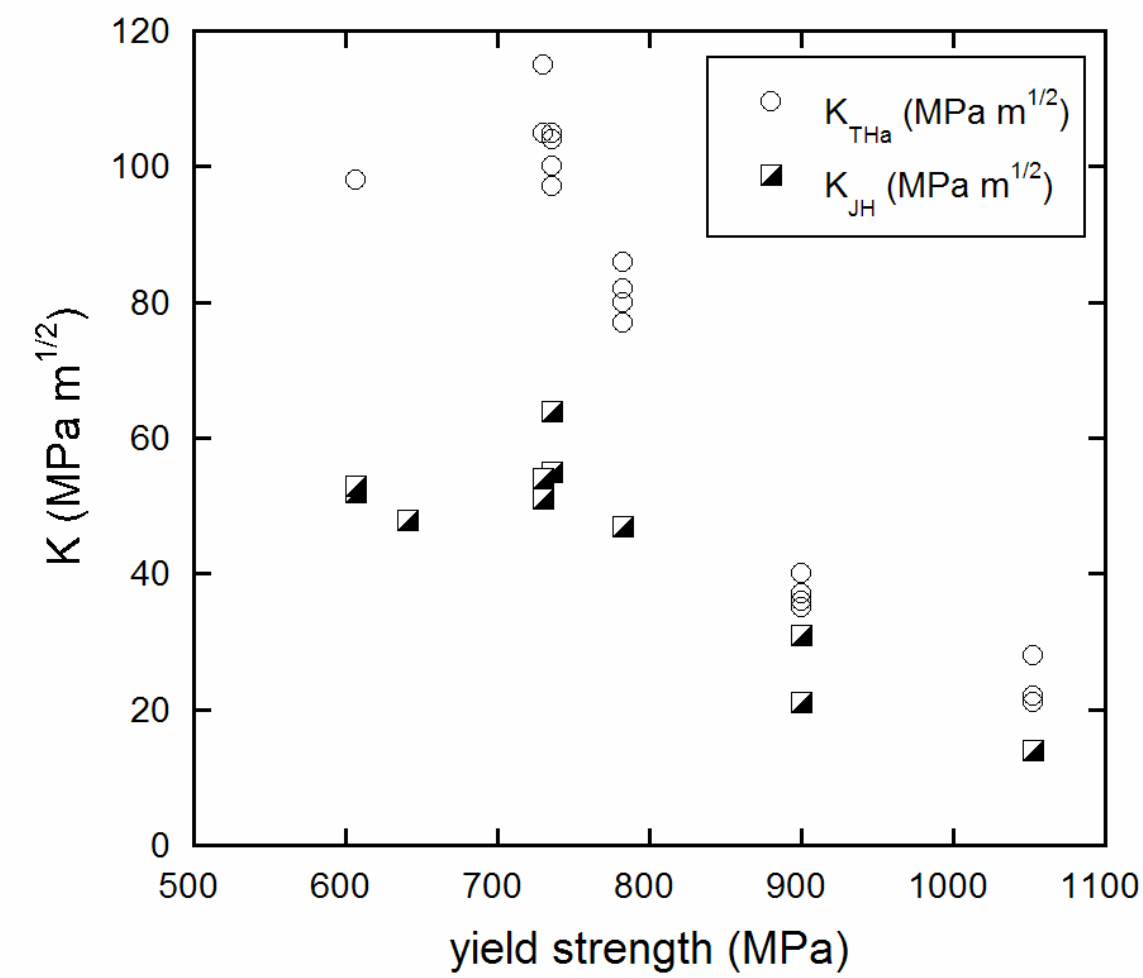

Figure 19 Crack arrest thresholds from constant displacement tests (K_{THa}) and crack initiation thresholds from rising displacement tests (K_{JH}) plotted as a function of yield strength.

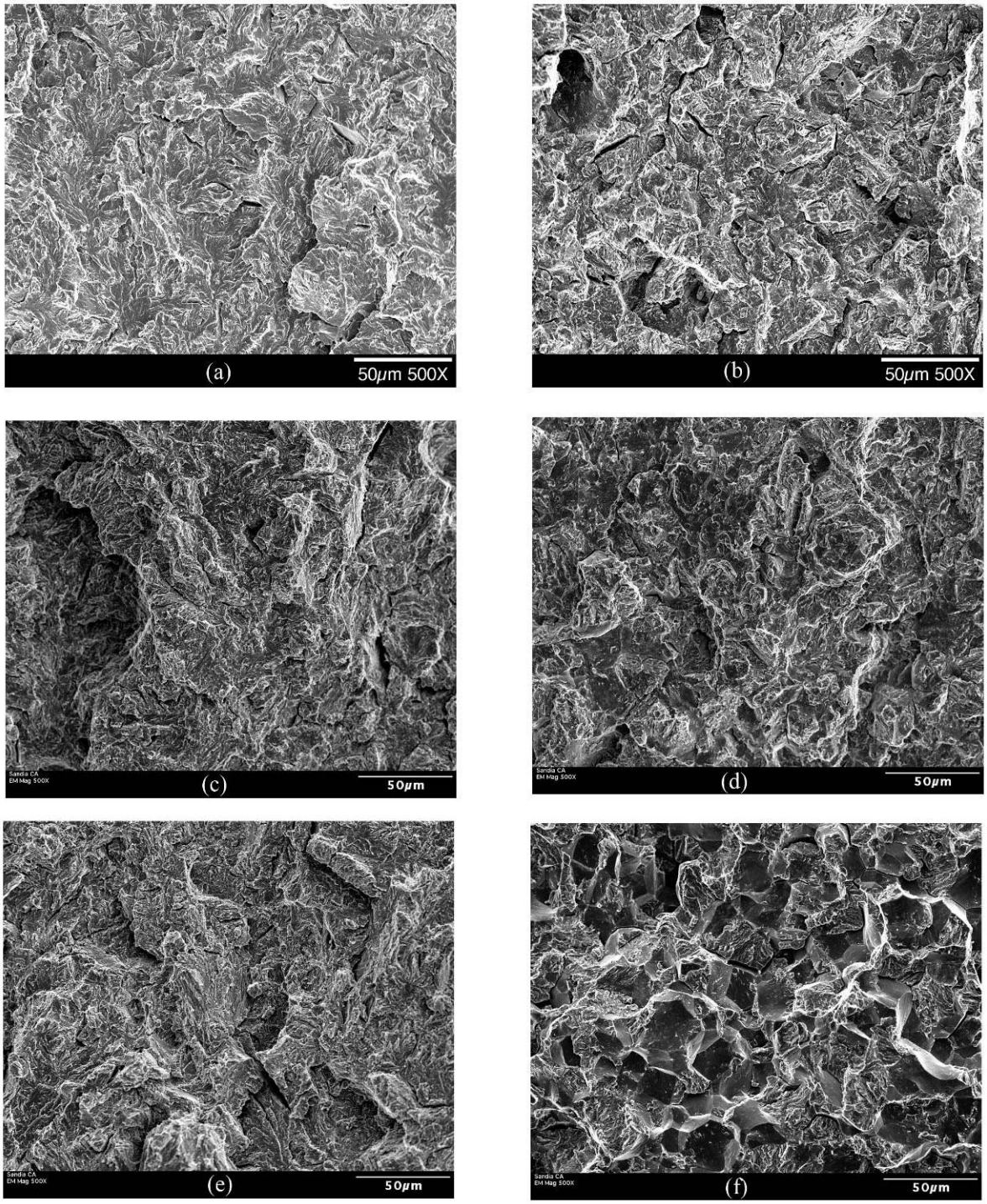

Figure 20 Secondary electron fracture surface images showing a region near crack arrest from (a) DOT-3AAX-1, (b) DOT-3T-2, (c) SA372 grade L -1 (731 MPa), (d) SA372 grade L-1 (1053 MPa), (e) SA 372 grade J-K236-2C, and (f) HY130-200C01.

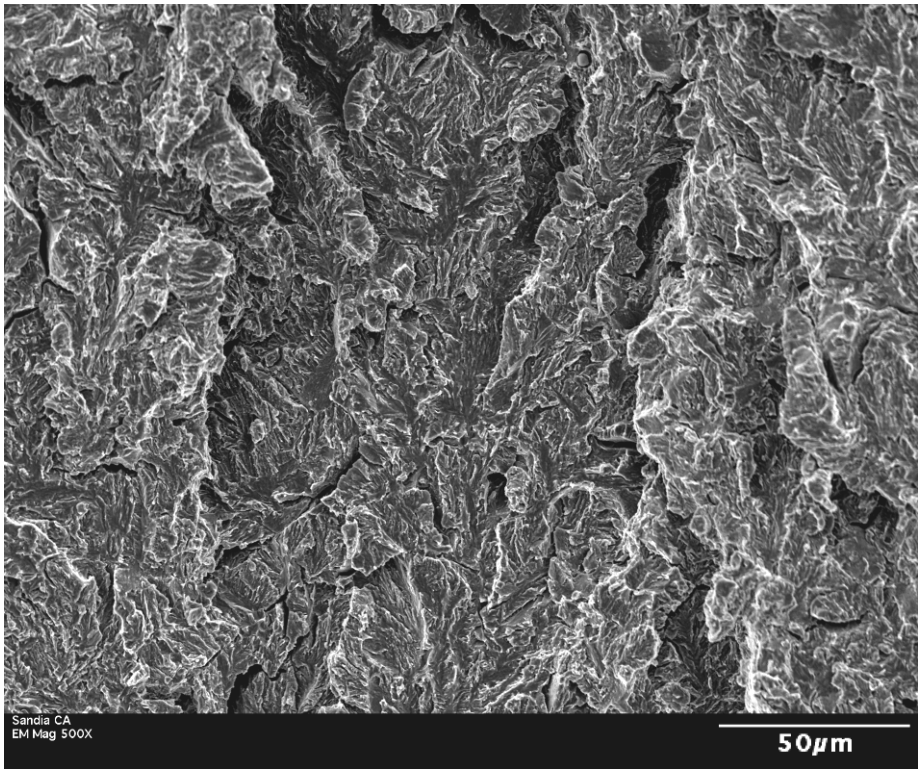

(a)

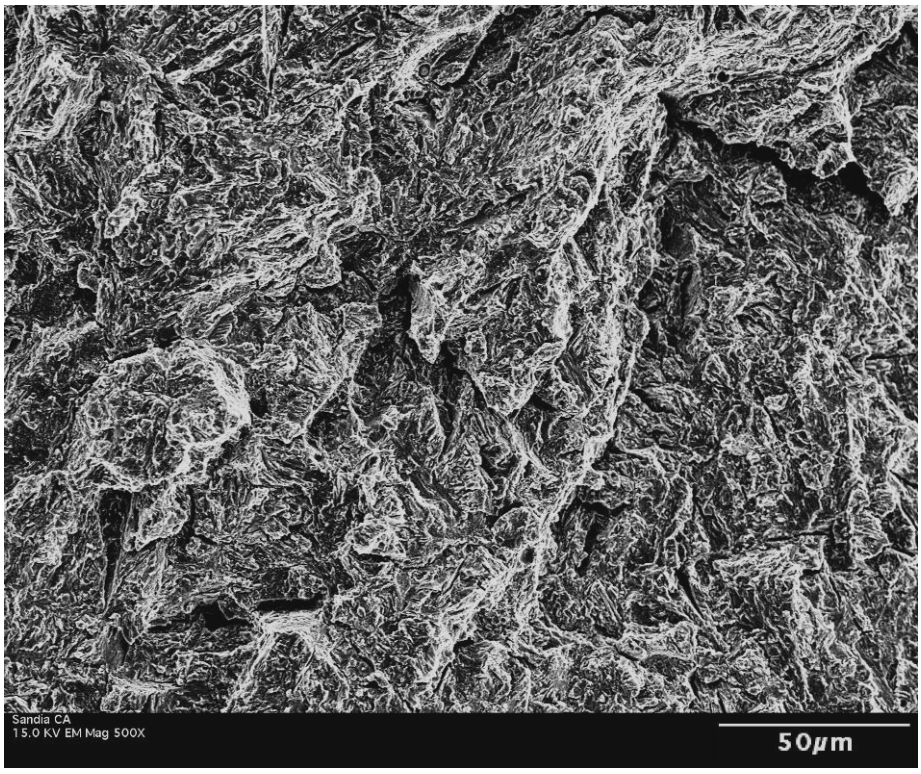

(b)

Figure 21 Secondary electron images of fracture surface taken near initiation from rising-displacement threshold specimens (a) DOT-3AAX-101 and (b) SA372 grade J-Y046-3.

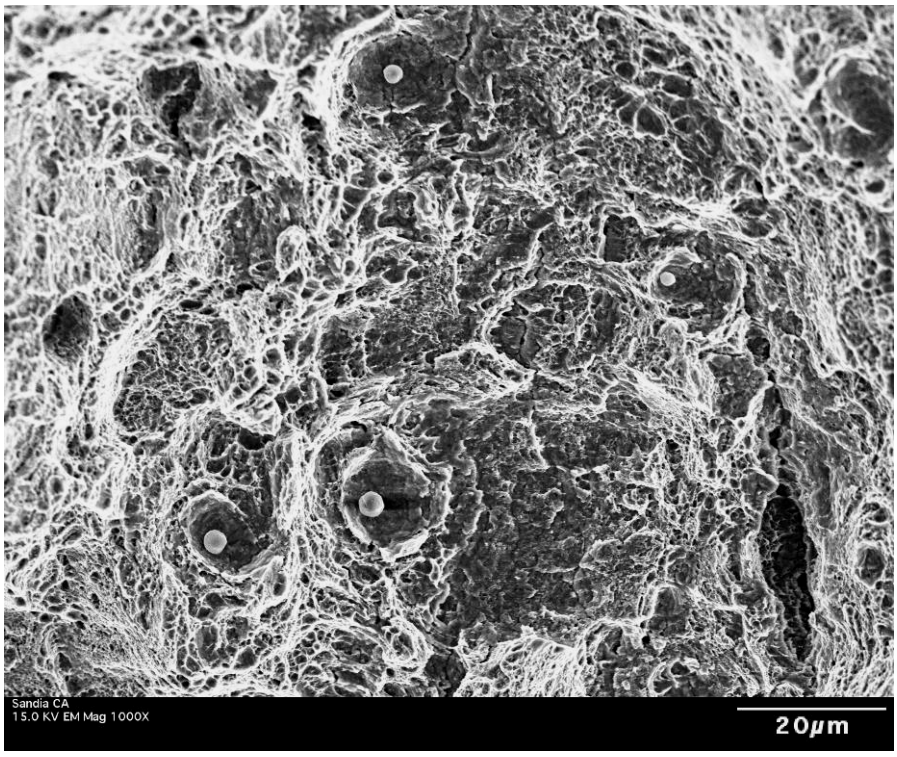

(a)

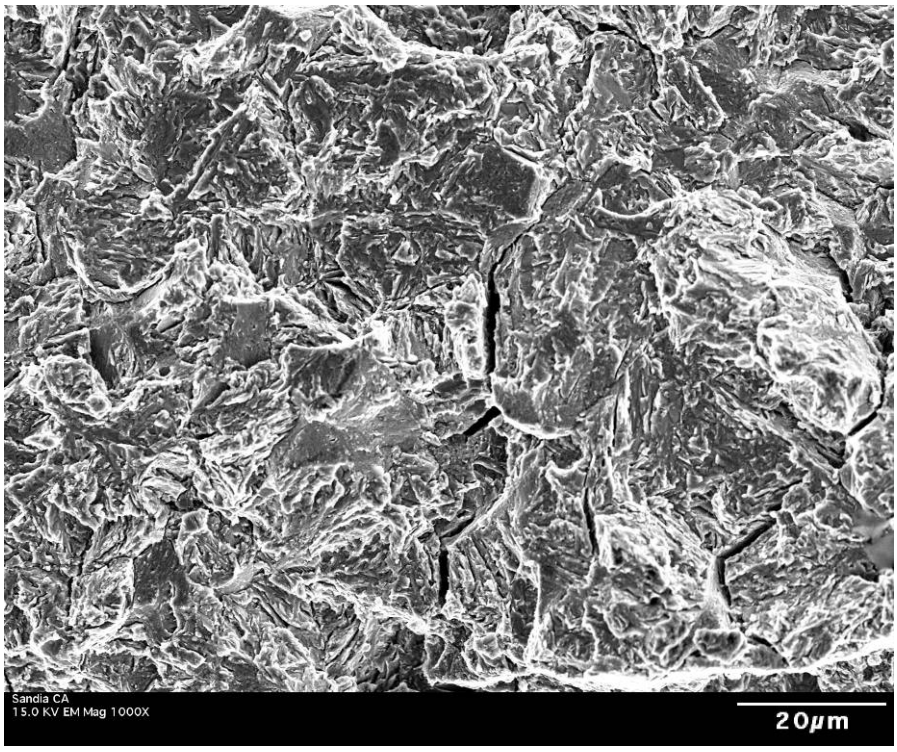

(b)

Figure 22 Fracture surfaces from DOT-3T CT specimens tested under rising displacement in (a) laboratory air and (b) 103 MPa gaseous hydrogen.

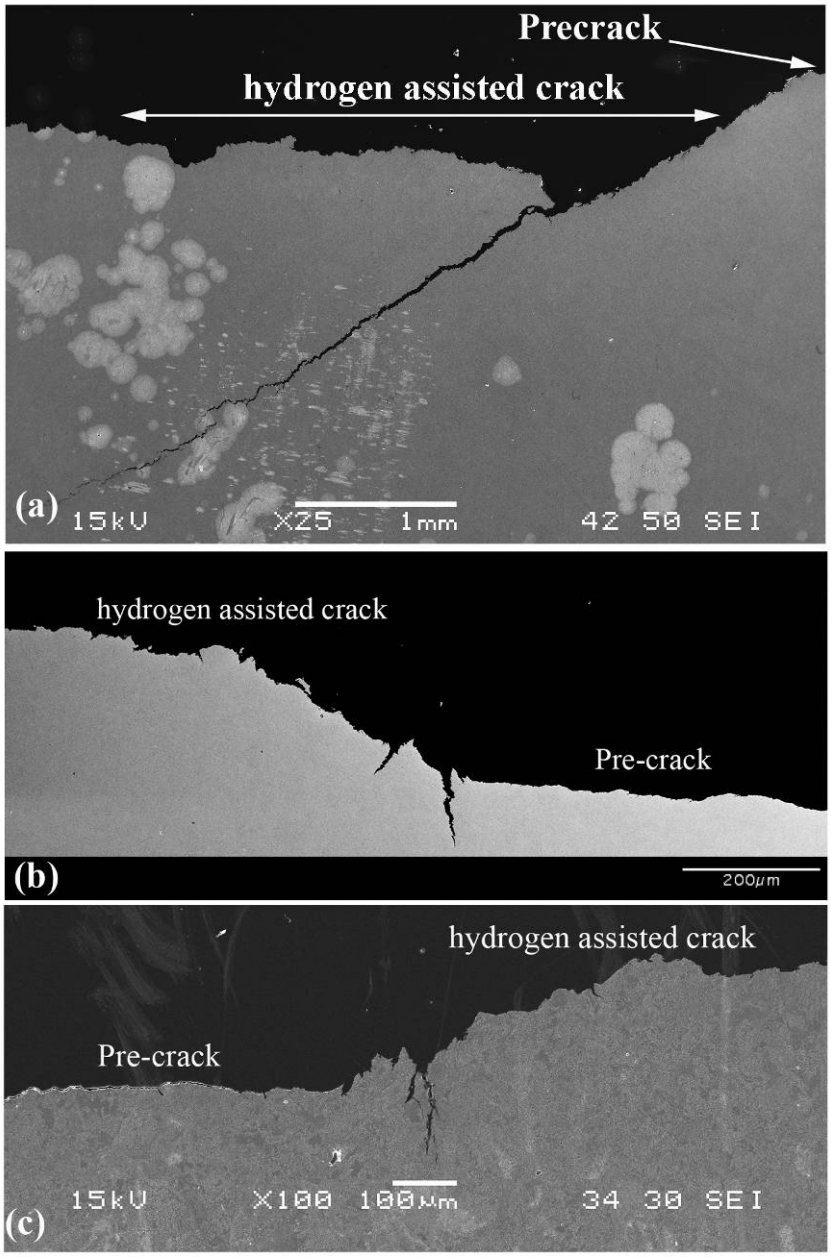

Figure 23 Secondary electron images from cross sections of (a) DOT-3T-1, (b) SA372 grade J-2, and (c) DOT-3AAX-4 showing crack bifurcations which occurred between the end of the fatigue pre-crack and the hydrogen assisted cracking region.

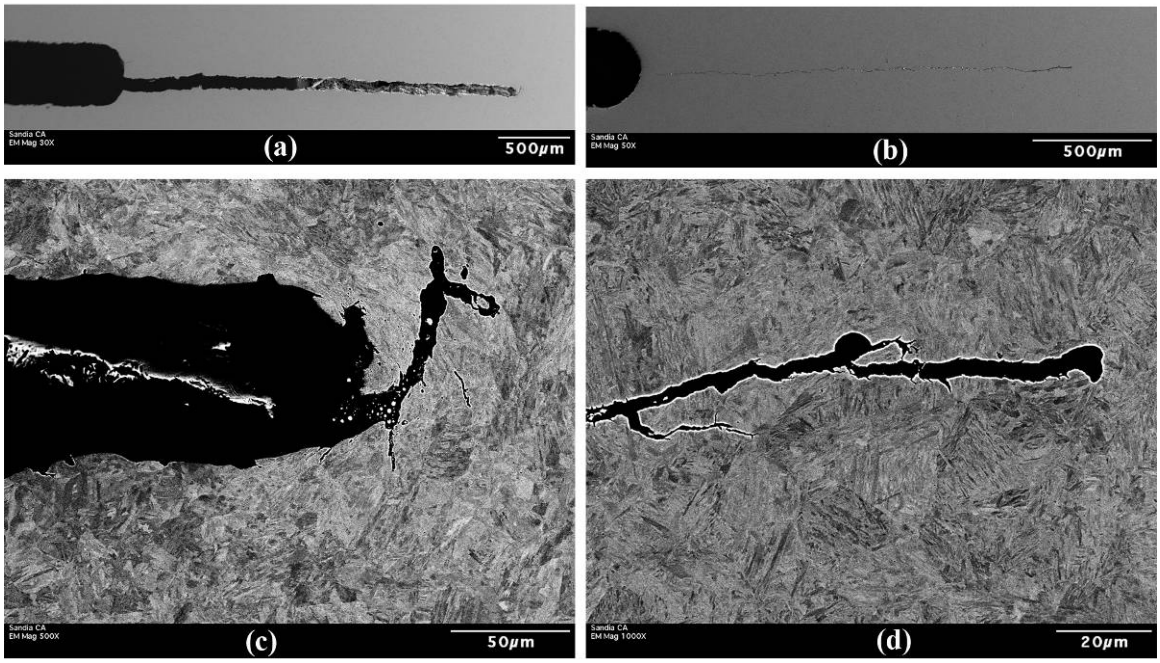

Figure 24 Cross sections images from SA 372 grade J-K236 1A (K_{app}=200 MPa $m^{1/2}$) (a) and (c) and from DOT-3T-8 (K_{app}=58 MPa $m^{1/2}$) (b) and (d). Secondary electron images (a) and (b) show the pre-crack emanating from the machined starter notch. Backscatter images at high magnification (c) and (d) show the blunted pre-crack tip.

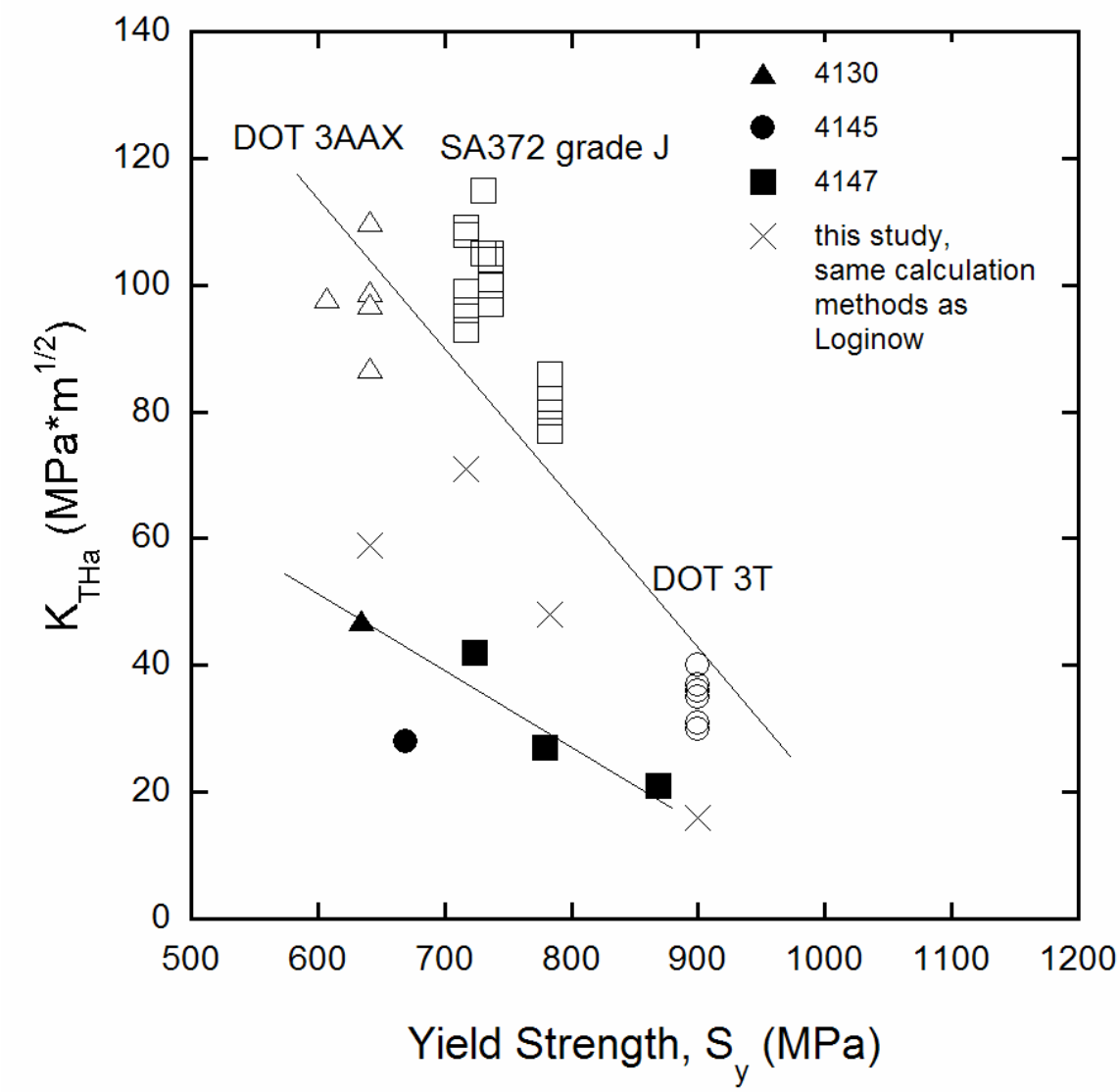

Figure 25 Comparison of K_{THa} generated in this study (open symbols) with data generated by Loginow and Phelps (ref. [13], solid symbols). Data points marked by X represent measurements from specimens tested in this study, but calculated using the K-solution and methods used in ref. [13].

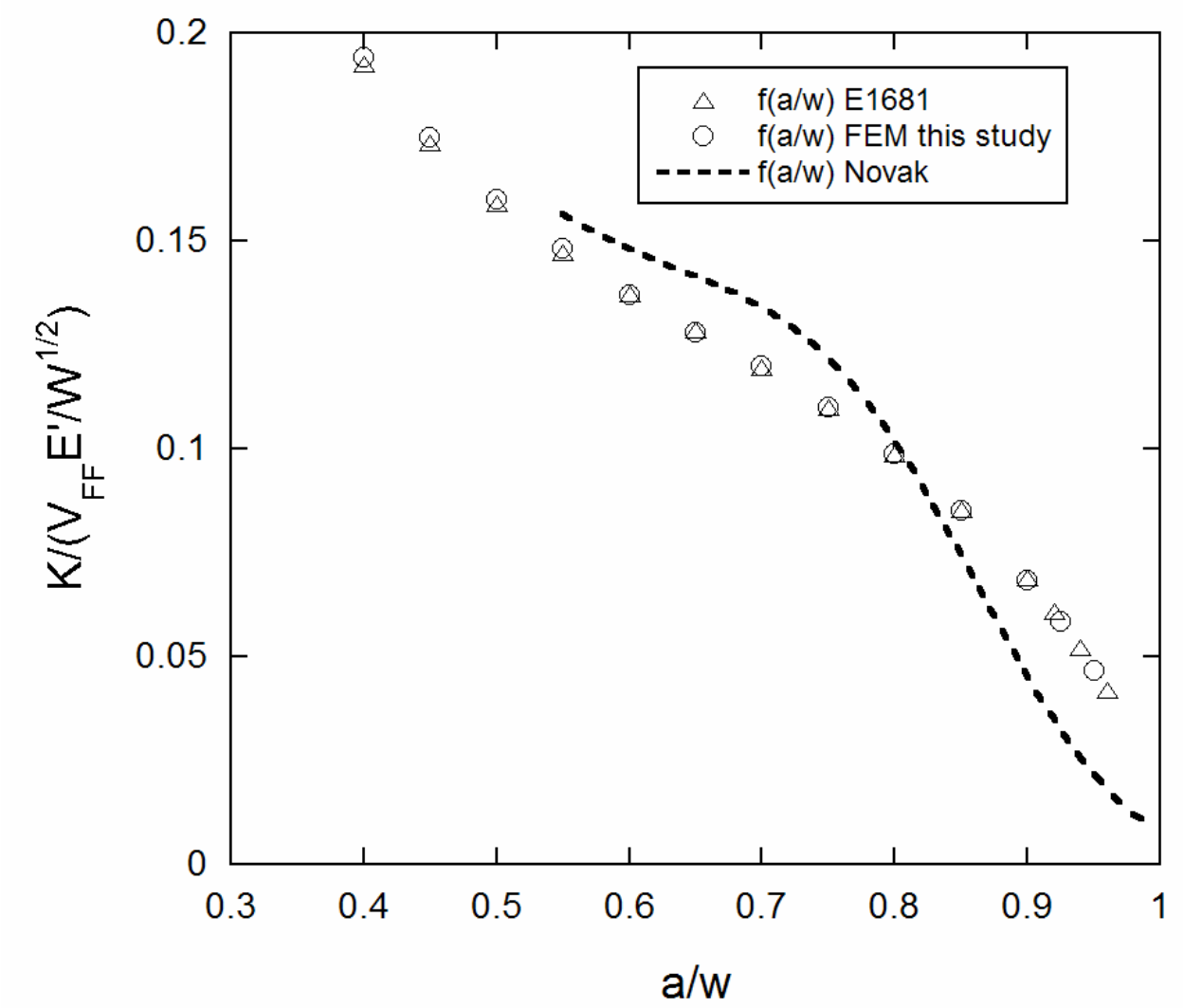

Figure 26 Normalized K solutions versus normalized crack length showing difference between the K solution given in ASTM E1681 (equation (1)) and that proposed by Novak [37]. Finite element simulations confirm the accuracy of the solution given in E1681.

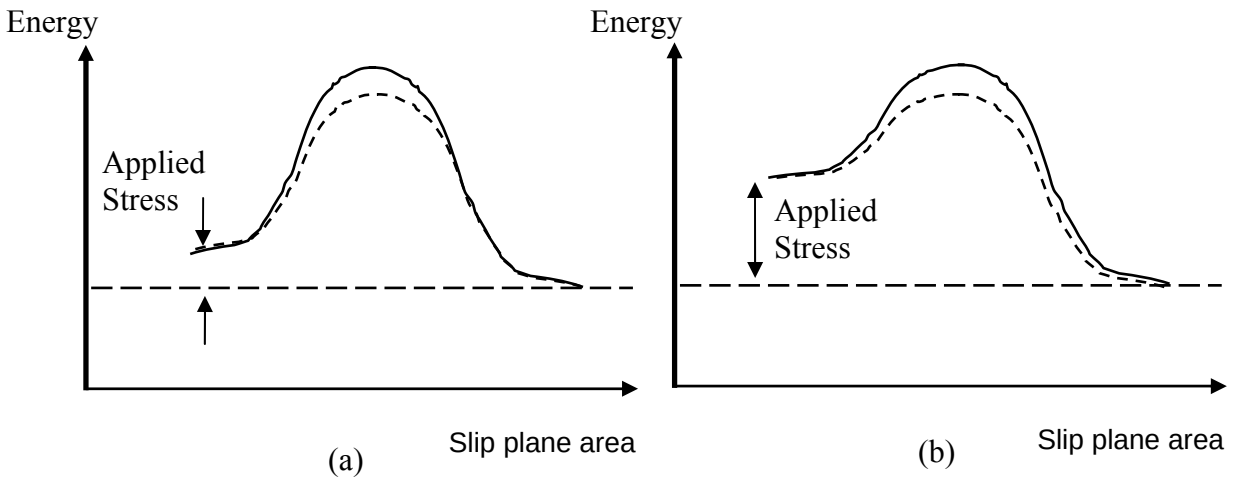

Figure 27 Representation of the activation barrier to dislocation glide. The solid line represents the barrier in the absence of hydrogen. In the presence of hydrogen the activation barrier is reduced, as represented by the dashed curve. In the presence of low applied stress (a) thermal energy must provide a greater contribution to overcome the barrier and dislocation glide past the barrier will be less probable relative to the case with a larger applied stress (b).

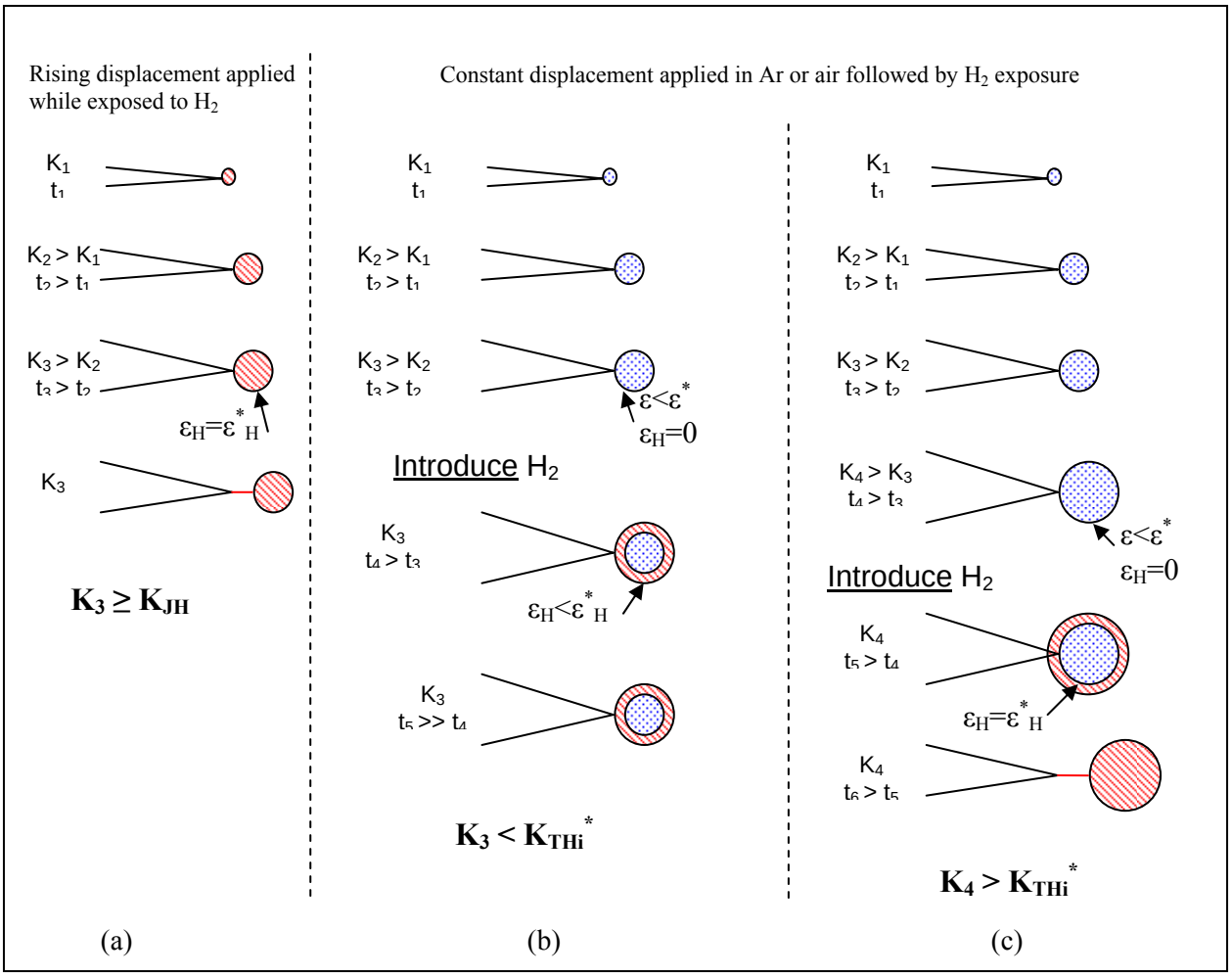

Figure 28 The process by which increasing crack opening displacement leads to the development of the crack tip plastic zone, microcracks and ultimately, crack propagation differs when load is applied in hydrogen environments (a) relative to when load is applied in an inert environment and hydrogen exposure follows (b) and (c).

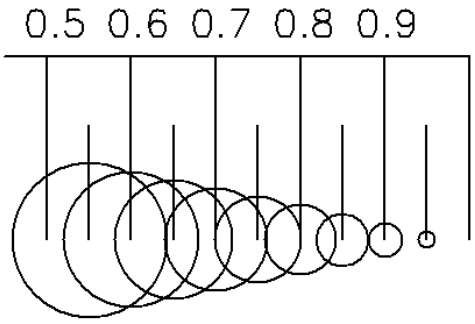

(a)

Yield Strength = 641 MPa
COD=1.57mm K_{app} = 200 MPa $m^{1/2}$

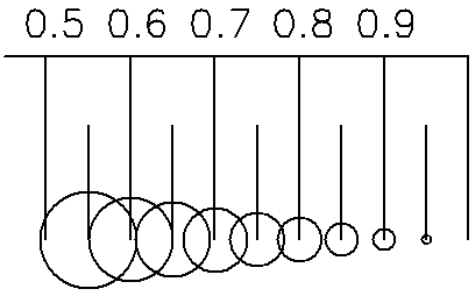

(b)

Yield Strength = 641 MPa
COD=1.24mm K_{app} = 160 MPa $m^{1/2}$

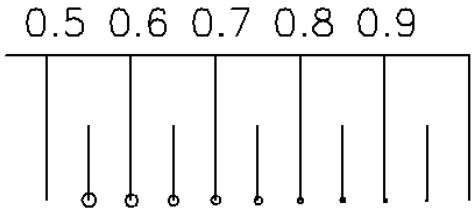

(c)

Yield Strength = 900 MPa
COD=0.65 mm K_{app} = 84 MPa $m^{1/2}$

Figure 29 Schematic representation of the crack tip plastic zone size in the WOL specimen at various crack positions. (a) and (b) approximate the conditions for DOT-3AAX specimens 1 and 4, while (c) represents DOT-3T specimen 2.

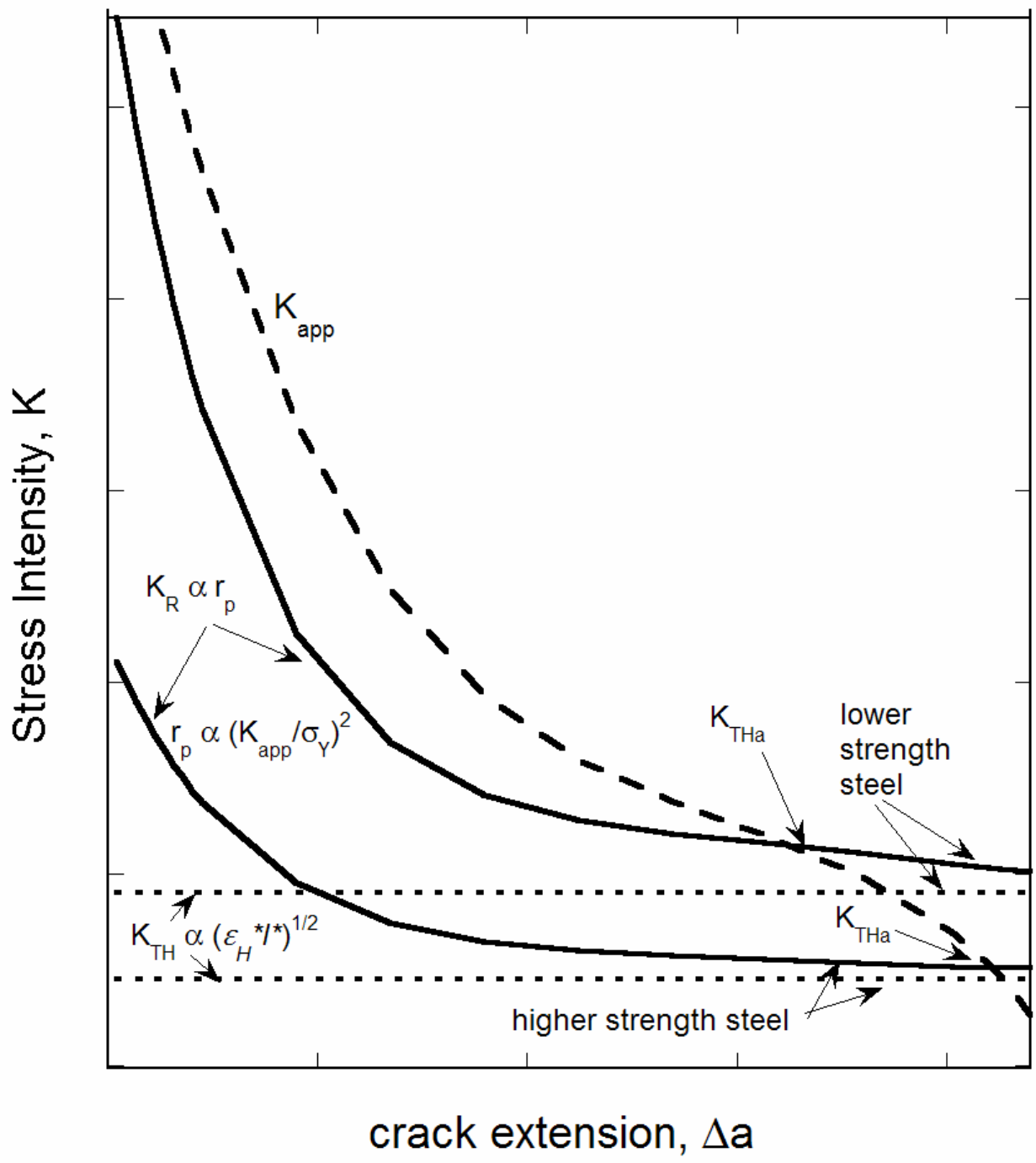

Figure 30 K_{app}, K_R and true fracture threshold (K_{TH}) as a function of crack extension.

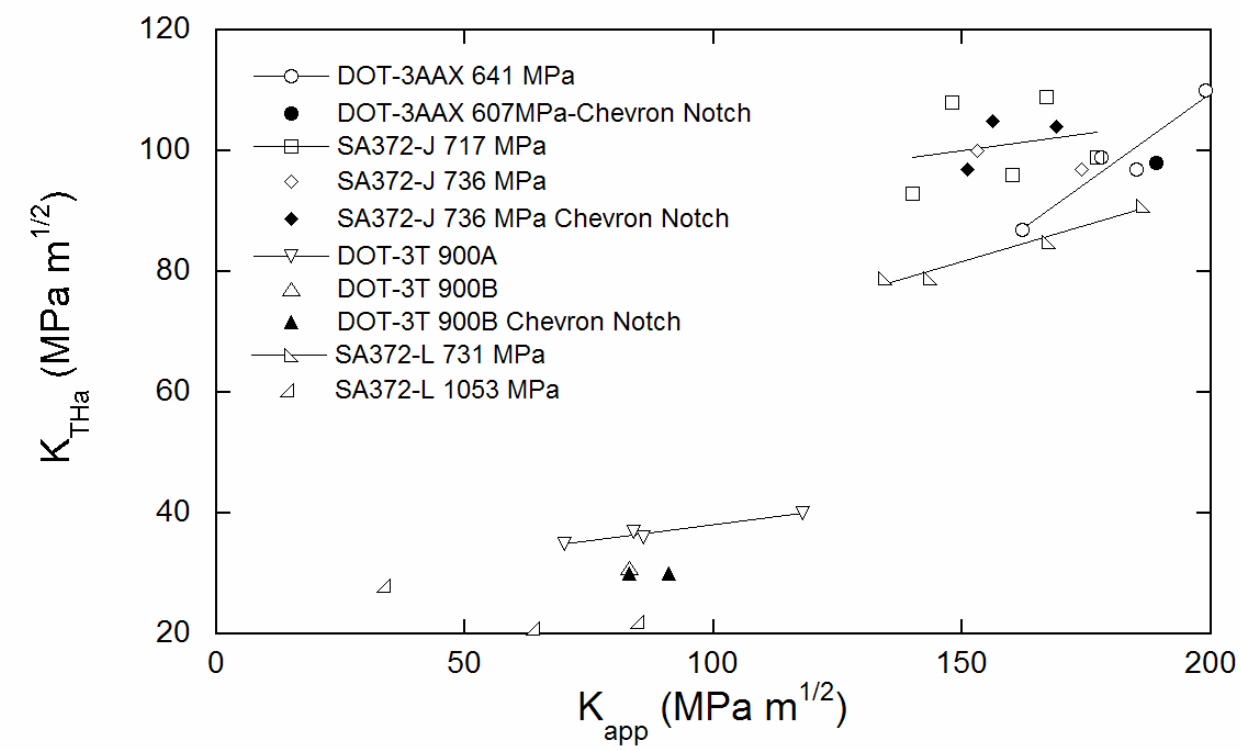

Figure 31 A trend between K_{THa} and K_{app} exists such that K_{THa} tends to increase as K_{app} is increased. Lines fit through select data sets illustrate this trend.

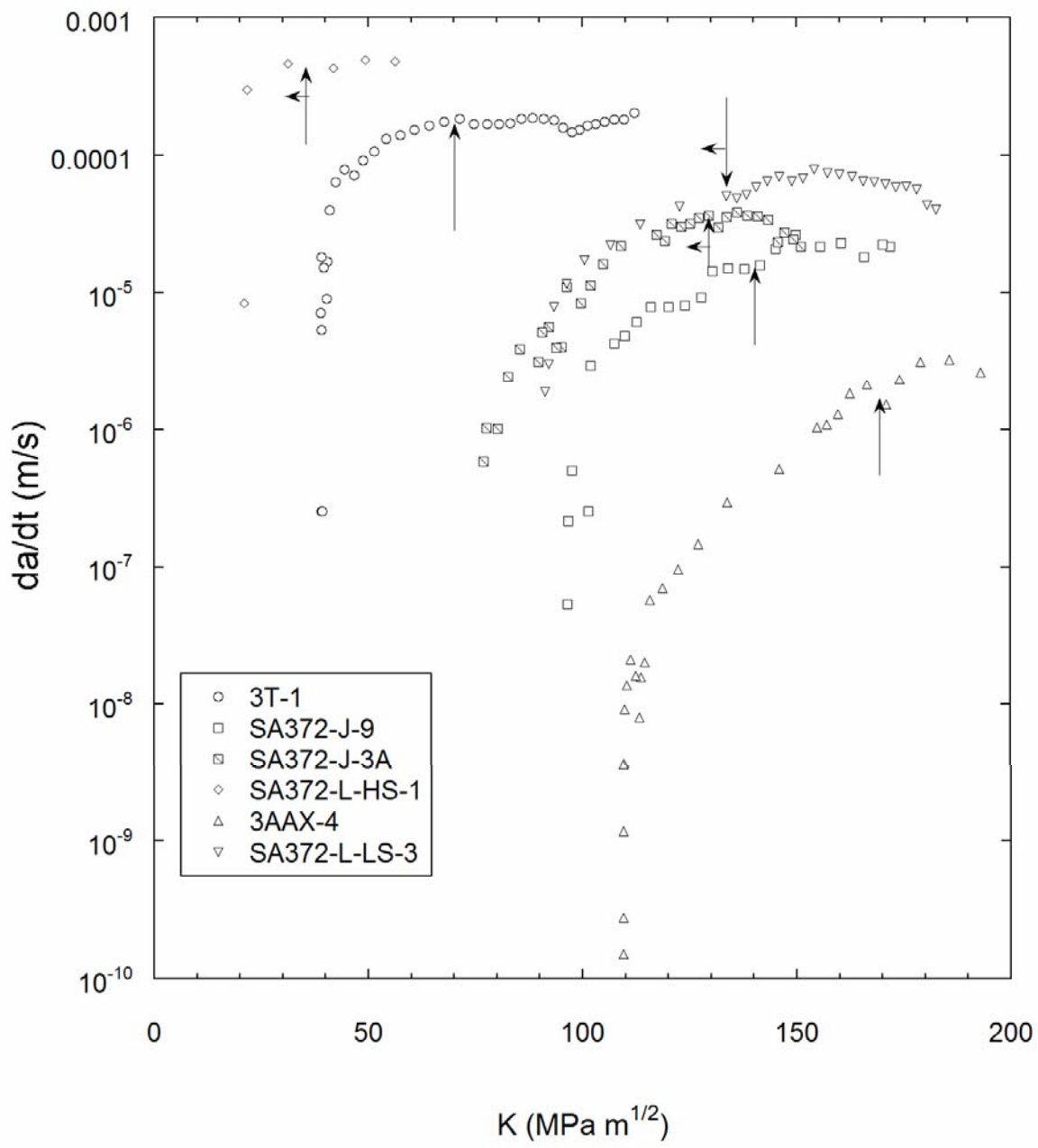

Figure 32 Crack growth rate plots for steel specimens loaded to the highest value of K_{app} showing that, in all cases, there appears to be a region of K-independent stage II crack growth. Arrows represent the values of K_{THi}^{*} determined for each steel which correspond closely with the onset of K-independent stage II behavior.

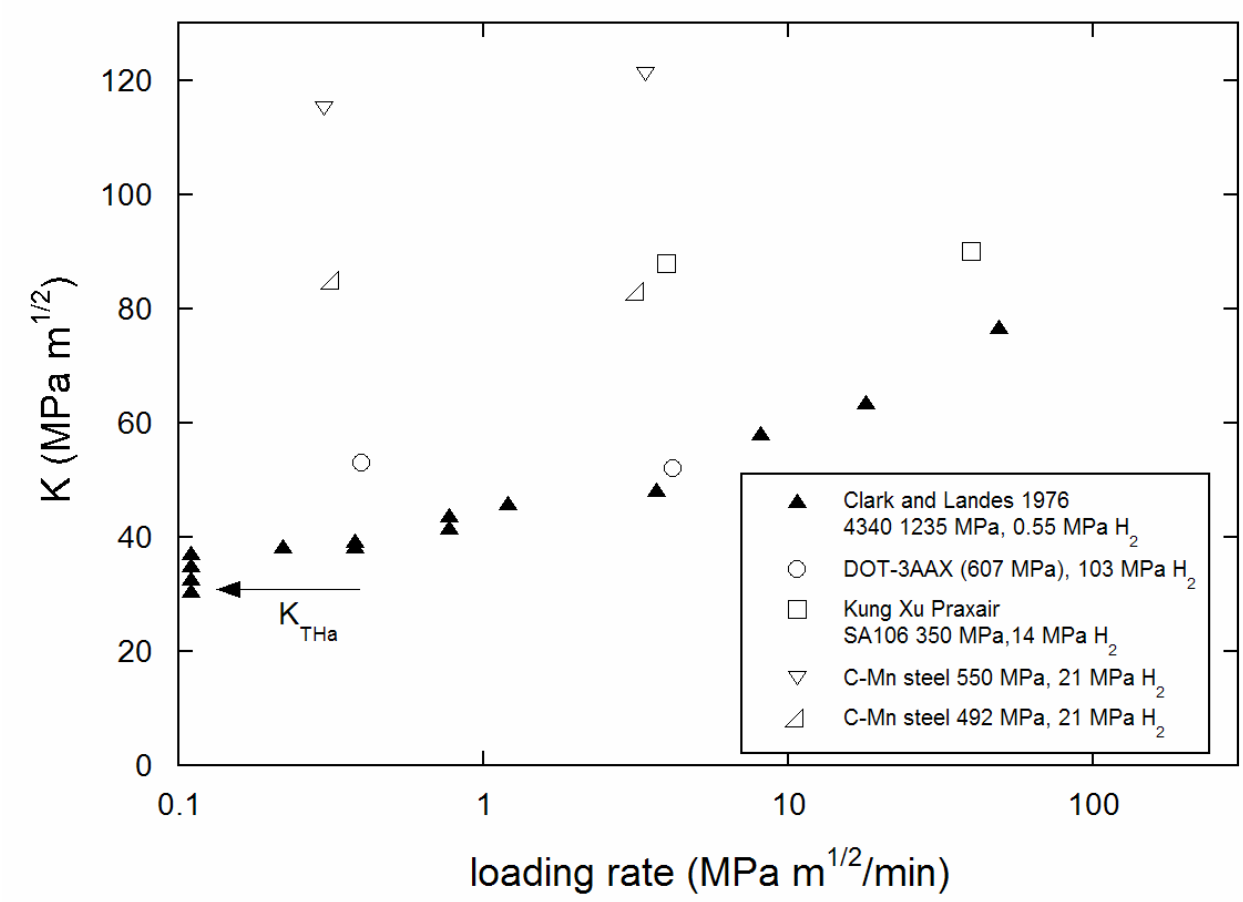

Figure 33 Plots of K versus loading rate for rising displacement tests show that K can increase with loading rate at large values of loading rate. At loading rates below about 10 MPa $m^{1/2}$/min little or no effect of loading rate has been observed for specimens tested at higher H_2 gas pressure, however at lower hydrogen pressure (0.55 MPa H_2) thresholds exhibit a dependence on loading rate above about 0.2 MPa $m^{1/2}$/min. Data from refs [16,106,107].

APPENDIX A: FEM RESULTS FOR BOLT AND CLEVIS LOADING OF WOL SPECIMEN

Finite element models of the WOL specimen were constructed to evaluate several mechanical aspects of this specimen. The solutions for stress intensity factor, K, and compliance, C, given in equations (1) and (4), respectively, were verified by finite element modeling. The specimen was modeled in two different ways to consider both bolt loading as well as loading with a clevis. Pre-cracking of these specimens and initial compliance measurements were made by inserting the specimen into a servo-hydraulic load-frame such that a threaded stud was attached to the top of the specimen and the bottom of the specimen was pinned through a clevis (Figure 3). Comparisons of normalized compliance, BE'V/P, for the two loading methods are shown in Figure A1. Again, E′ is E for plane stress and $E/(1-\nu^2)$ for plane strain. Although the specimens are sufficiently thick to merit a plane strain description of the crack tip fields, we find that the far-field loads and resulting compliance are better aligned with a plane stress description. Results from the FEM simulations modeling the bolt loaded geometry are in good agreement with equation (4). At crack-lengths around a/W=0.5, typical of pre-crack positions, the compliance solution assuming clevis loading is slightly higher than that which assumes bolt loading. The difference may stem from the fact that a large region of the beam is displaced in the clevis loading, in contrast to the point-loaded bolt geometry. The clevis promotes an increased shear loading on the upper beam which results in lower reaction loads P and greater front-face displacements V_{FF}. If compliance methods are used to monitor crack length during pre-cracking, compliance solutions which assume bolt loading conditions (such as equation (4)) will overestimate the actual crack length by as much as 3.4%. The polynomial fit of a/W as a function of the Z normalization for the clevis loaded geometry in the following functional form

$$a/W=C_1Z^4+ C_2Z^3+ C_3Z^2+ C_4Z+ C_5 \qquad (A1)$$

$$Z=1/(V_{FF}E'B/P)^{1/2}$$

yielded the following values for the coefficients: $C_1=$ 756.8074, $C_2=$ -196.7180, $C_3=$ 15.5142, $C_4=$ -4.4614, and $C_5=$ 0.9998. This relationship for crack length as a function of measured

specimen compliance was determined for the range of $0.4 < a/W < 0.95$. This relationship may be used to predict crack length during WOL specimen pre-cracking if a clevis configuration similar to that shown in Figure 3 is utilized.

The K solutions determined for the two loading conditions are plotted in Figure A2. At shorter crack lengths, the clevis loaded specimen will experience a smaller stress intensity factor at the crack tip relative to a bolt loaded specimen with the same front face displacement. The two solutions converge at crack lengths greater than a/W~0.8. At smaller crack lengths the details of shearing short beams (via the clevis) do affect the applied stress intensity factor. However, as the beams become longer, the method of applied displacement becomes less important and the solutions coincide. During pre-cracking, assuming the specimen is loaded using the clevis arrangement at crack-lengths near a/W=0.5, the actual stress intensity factor will be about 6% lower than that calculated using Equation (1).

The output data from the WOL simulations for both the bolt-loaded and clevis loaded WOL geometries are provided in Tables A1 and A2.

Table A1 Raw output from FEM simulations on WOL specimens from which fits for K and compliance versus a/W were generated. Loading conditions simulate bolt loading. (See Figure 7)

a/W	K (ksi $in^{1/2}$) (plane strain)	K (ksi $in^{1/2}$) (plane stress)	$V_{FF}/2$ (in) (plane strain)	$V_{FF}/2$ (in) (plane stress)	Reaction Load (lbs) (plane strain)	Reaction Load (lbs) (plane stress)
0.4	21240	19640	2.48E-03	2.52E-03	3907	3614
0.45	19460	17940	2.52E-03	2.55E-03	3204	2955
0.5	17950	16510	2.55E-03	2.57E-03	2610	2402
0.55	16680	15310	2.56E-03	2.59E-03	2102	1930
0.6	15570	14270	2.57E-03	2.59E-03	1660	1522
0.65	14570	13330	2.58E-03	2.59E-03	1274	1166
0.7	13580	12400	2.58E-03	2.59E-03	936.6	856.4
0.75	12480	11390	2.57E-03	2.58E-03	647.2	591.1
0.8	11180	10190	2.57E-03	2.57E-03	408.1	372.5
0.85	9593	8737	2.56E-03	2.56E-03	222.9	203.3
0.9	7648	6961	2.54E-03	2.54E-03	94.87	86.54
0.925	6508	5921	2.53E-03	2.54E-03	51.97	47.43
0.95	5203	4734	2.53E-03	2.53E-03	22.45	20.49

Table A2 Raw output from FEM simulations on WOL specimens from which fits for K and compliance versus a/W were generated. Loading conditions simulate clevis loading. (See Figure 8)

a/W	K (ksi $in^{1/2}$) (plane stress)	$V_{FF,1}$ (in) (plane stress)	$V_{FF,2}$ (in) (plane stress)	Reaction Load (lbs) (plane stress)
0.45	18850	1.8487E-03	-3.3572E-03	3096
0.5	17480	1.9068E-03	-3.3241E-03	2535
0.55	16310	1.9558E-03	-3.2845E-03	2051
0.6	15290	1.9975E-03	-3.2406E-03	1627
0.65	14360	2.0332E-03	-3.1935E-03	1254
0.7	13420	2.0637E-03	-3.1442E-03	925.9
0.75	12380	2.0891E-03	-3.0942E-03	642
0.8	11130	2.1091E-03	-3.0458E-03	406.6
0.85	9565	2.1234E-03	-2.9995E-03	222.6
0.9	7637	2.1319E-03	-2.9573E-03	95.05

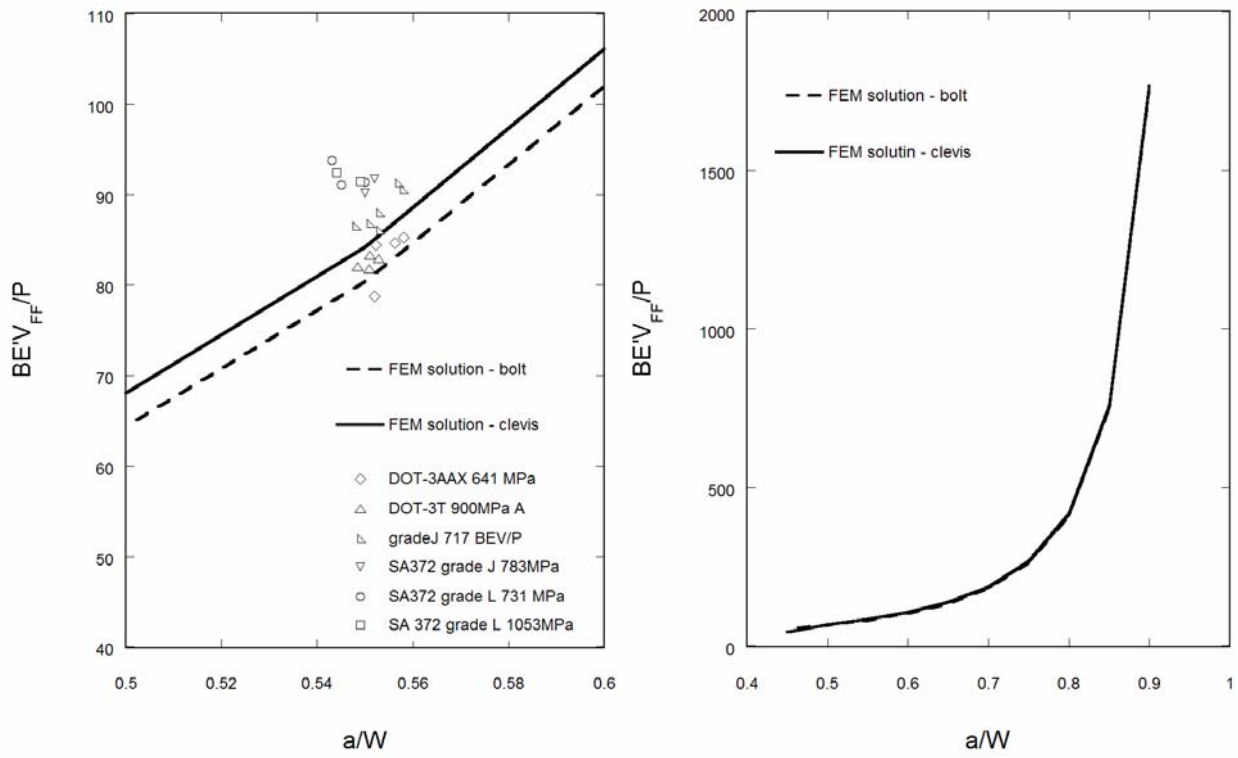

Figure A1. FEM results show the relationship between normalized specimen compliance ($BE'V_{FF}/P$) and the normalized crack length (a/W). For typical pre-crack lengths around a/W=0.5 (a), the specimen will appear slightly more compliant when measured using a clevis setup in a load frame relative to the bolt loaded configuration, but the difference overall between the two configurations is small (b). Included in (a) are measurements of compliance after pre-cracking for several specimens, showing that the measurements correlate best with the compliance solution which accounts for the clevis. Measurements from specimens with curved faces (e.g. DOT-3T and DOT-3AAX) are a bit lower suggesting that the curvature decreases the compliance slightly.

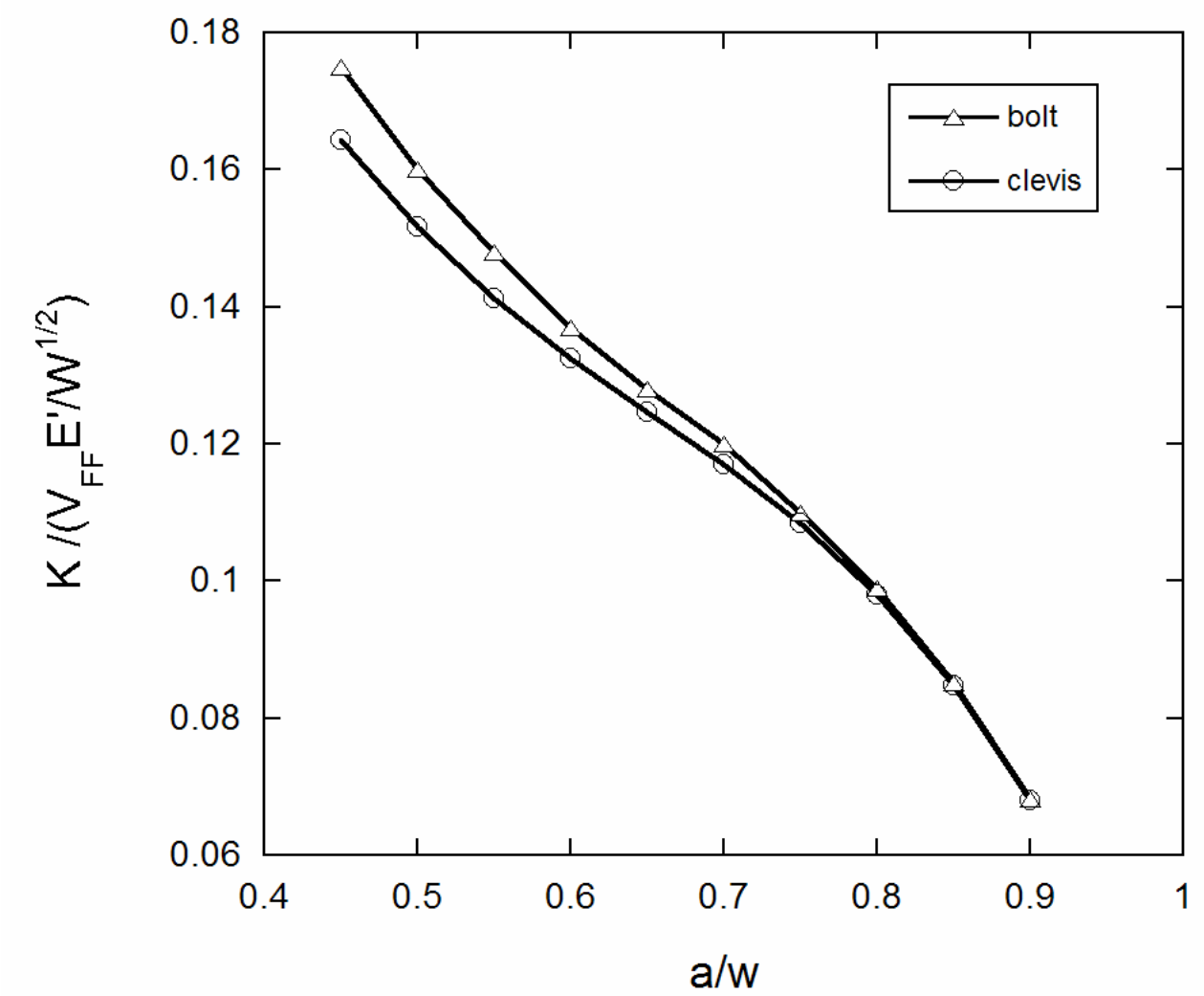

Figure A2. Finite element results for normalized stress intensity factor (K) versus normalized cracklength (a/w) showing the effect of bolt loading and clevis loading configurations.

APPENDIX B: PRE-CRACKING CHEVRON NOTCHED WOL SPECIMEN

The method used to estimate the crack position during fatigue pre-cracking of the chevron notched specimens is demonstrated in Figure B1. The chevron notch serves to increase the compliance of the specimen at short crack lengths, so available compliance solutions assuming a standard specimen with a straight notch were not appropriate. Rather than generating a new solution for the chevron notched specimen, a simple estimate was used and found to produce a good estimate of the crack-length from compliance measurements. The compliance was measured before pre-cracking began. This single data point was then added to the expected compliance values for crack lengths beyond the end of the chevron and a new curve was fit. This new curve fit yields a relationship between compliance and crack-length which was used to guide the pre-cracking procedures. As was the case for all of the specimens in this report, K_{app} values reported in Table 2 were determined after the specimen had been broken in half and the pre-crack length was physically measured.

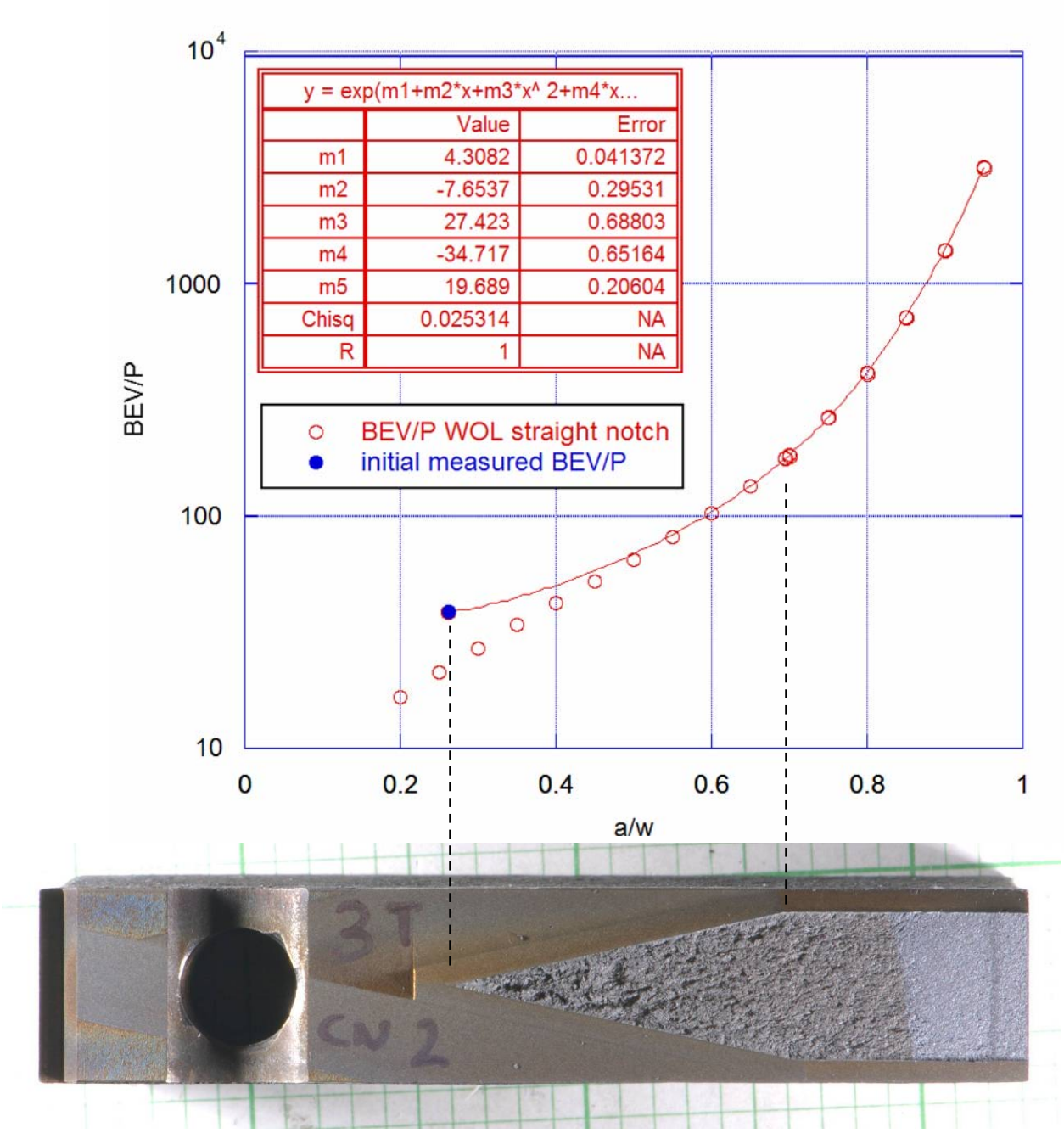

Figure B1 Estimation of pre-crack length in the chevron notched WOL specimen was accomplished by first measuring the compliance of the as-machined specimen. A curve was then fit through this measured point and through the expected compliance values beyond the chevron.

APPENDIX C: ALTERNATE WOL GEOMETRY: EXTENDED, TAPERED SPECIMEN.

The intended purpose of the specimens presented in this appendix was to increase the length of the uncracked ligament in order to allow for the application of large stress intensity factors, but not have the crack arrest near the back face of the specimen. The alternate geometry of an extended, tapered WOL specimen is shown in Figures C1 and C2. Finite element methods similar to those described in section 2.4.1 were used to study the mechanics of this specimen (Figure C3). Solutions for both K and compliance were generated as a function of crack length (a/W) and front-face displacement (Figures C4 and C5). As demonstrated in Figure C6, the tapered geometry causes K to decrease more rapidly with crack length, compared to the standard WOL geometry and therefore allows a larger range of K (between K_{app} and K_{THa}) to be explored. In addition, the taper postpones the transition to bending which occurs in DCB specimens at long crack lengths and leads to the unexpected increase in K as the crack approaches the back face of the specimen, as observed in Figure C6. Early experimental efforts with double cantilever beam (DCB) specimens resulted in crack deflection in the DOT-3T material (Figure C7) and permanent deformation with no crack extension in the DOT-3AAX (Figure C8). The extended WOL specimen geometry modification was intended to combine aspects of both the DCB and the conventional WOL specimen. Two specimens were machined from DOT-3AAX (607MPa), loaded to K_{app} = 169 and 199 MPa $m^{1/2}$ (2.8 and 3.25 mm front face displacement with initial crack lengths, a/W, ~0.45) in the glovebox and tested in 103 MPa H_2 gas. Neither specimen exhibited crack extension after 2600 hours of hydrogen exposure. After the test was terminated the specimens were unloaded and it was observed that a significant portion of the applied displacement was not recovered upon unloading. FEM elastic-plastic analysis (Figure C9) suggested that plastic strain on the top and bottom surfaces likely caused general yielding of the specimen such that the expected value of K_{app} was not experienced at the crack tip. Although this specimen geometry was abandoned at this point in favor of the chevron notched geometry described in the main body of this report, it may be a useful tool for situations using a higher strength material and/or small applied displacements.

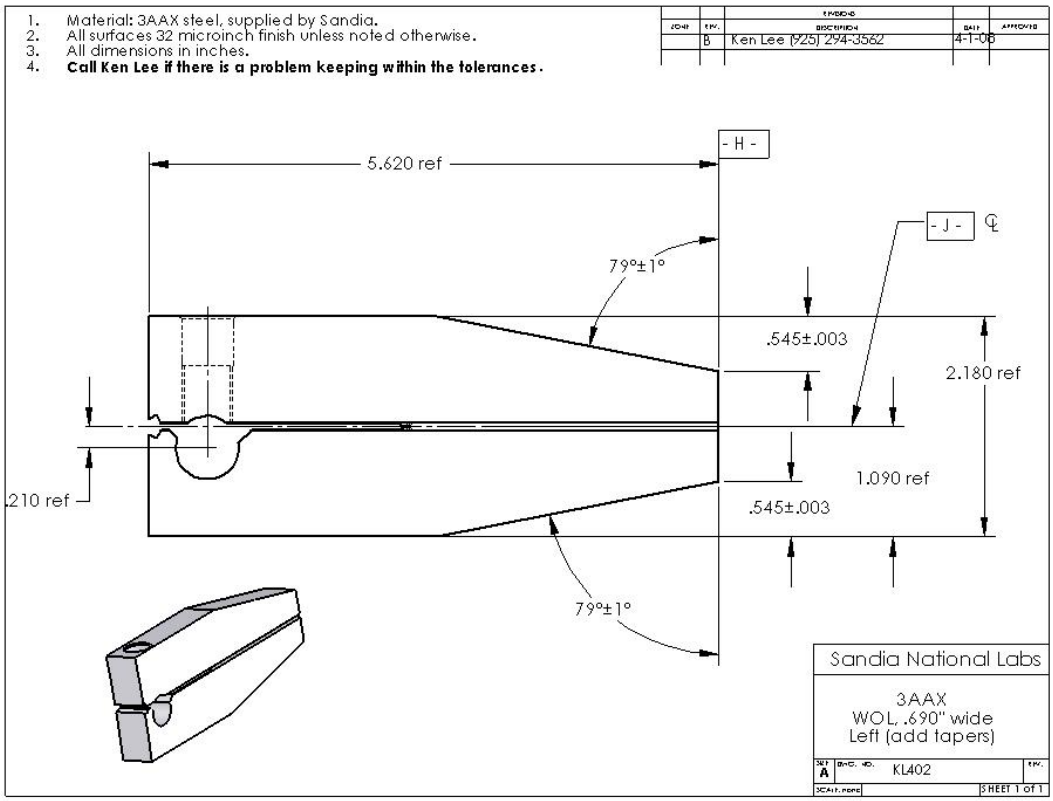

Figure C1 Geometry of the extended, tapered WOL modification. Dimensions not noted are nominally the same as those in the standard geometry.

Figure C2 Photograph of the extended, tapered WOL specimen with loading bolt.

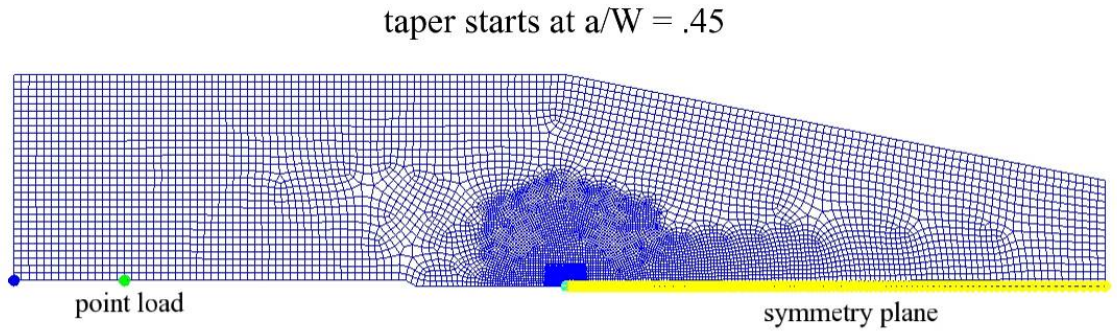

Figure C3 Finite element mesh of the tapered, elongated WOL specimen. FEM results for this specimen were generated using the same procedures as described in section 2.4.1.

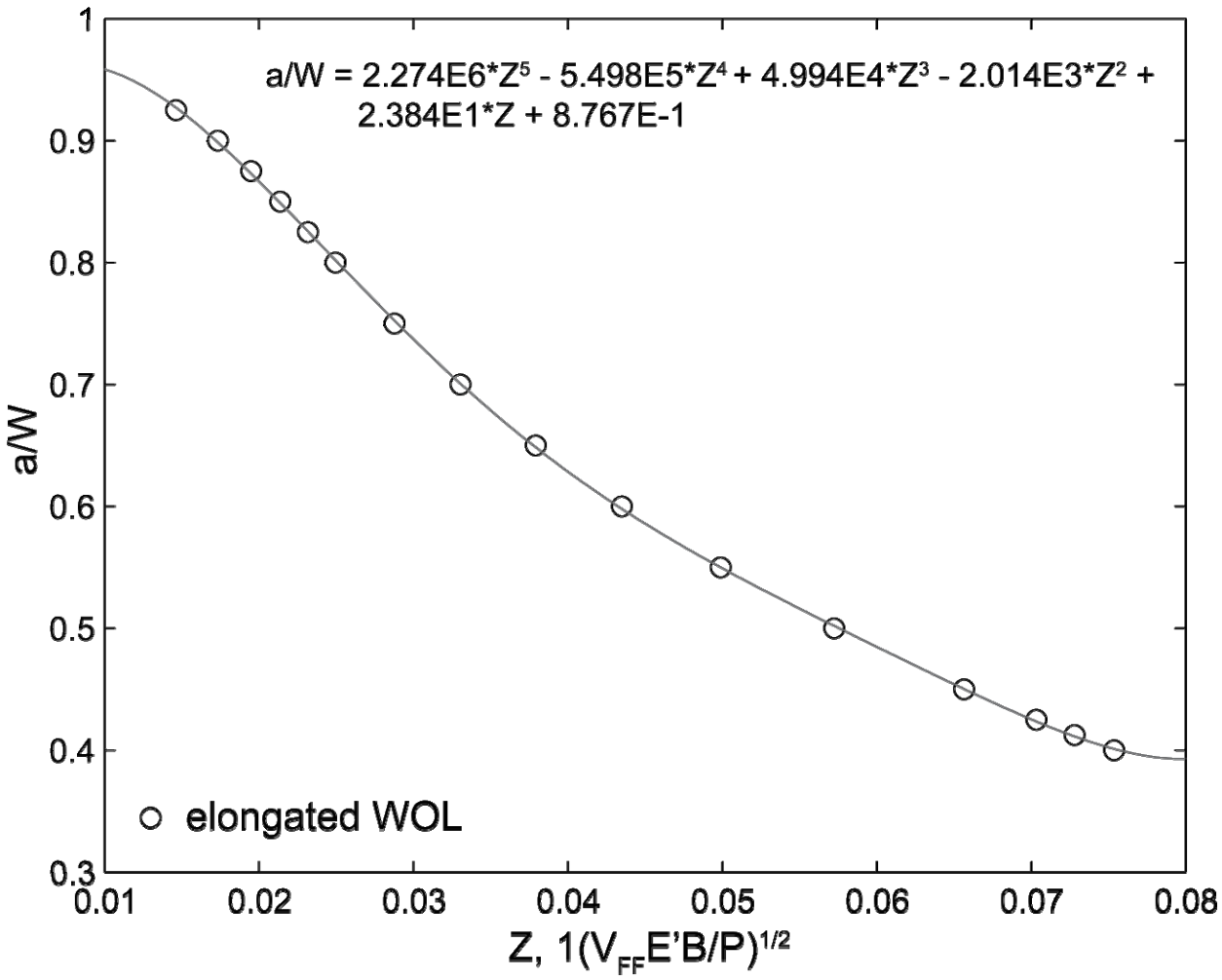

Figure C4 Curve fit to determine crack length (a/W) from measured compliance of the tapered, elongated WOL specimen.

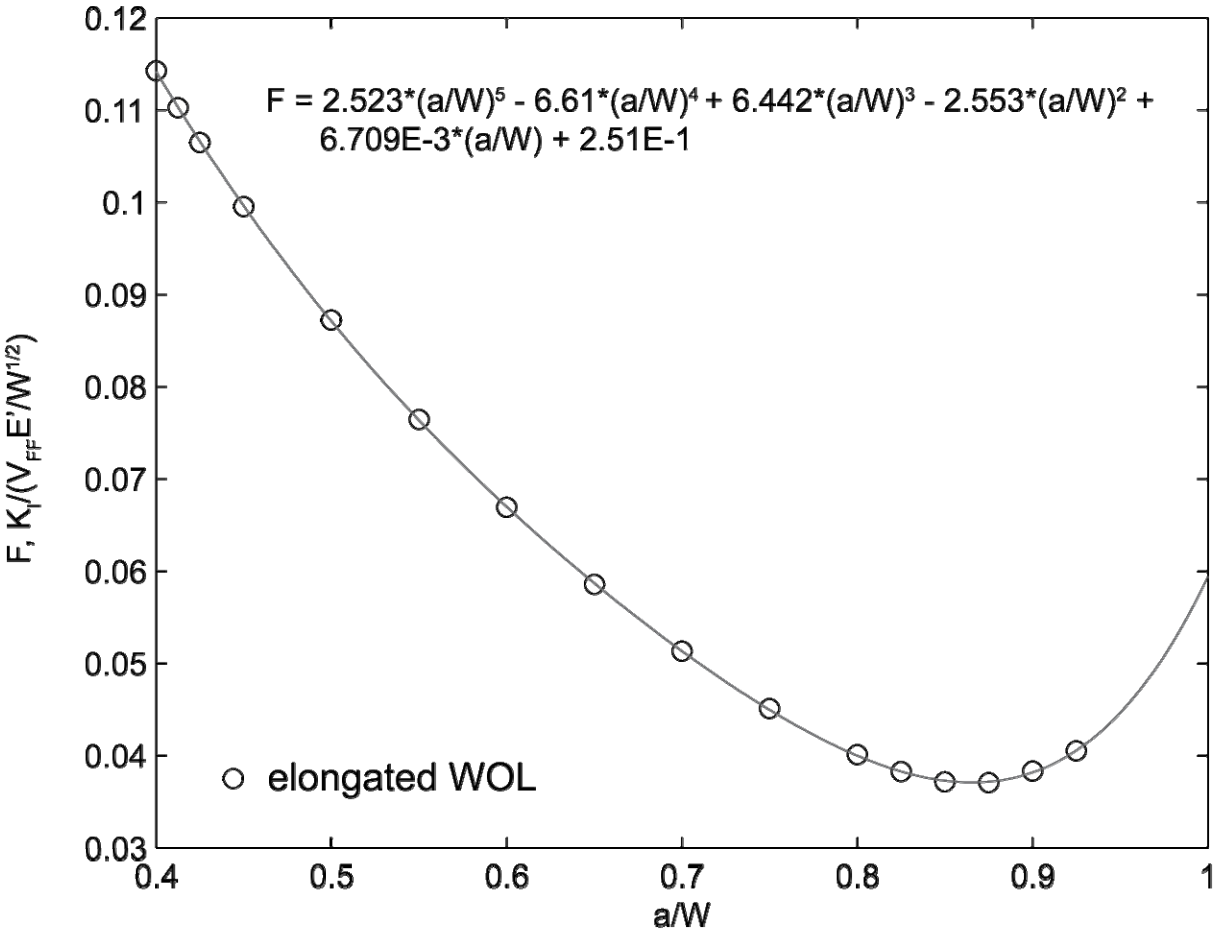

Figure C5 Curve fit to determine K from measured crack length and front-face displacement of the tapered, elongated WOL specimen.

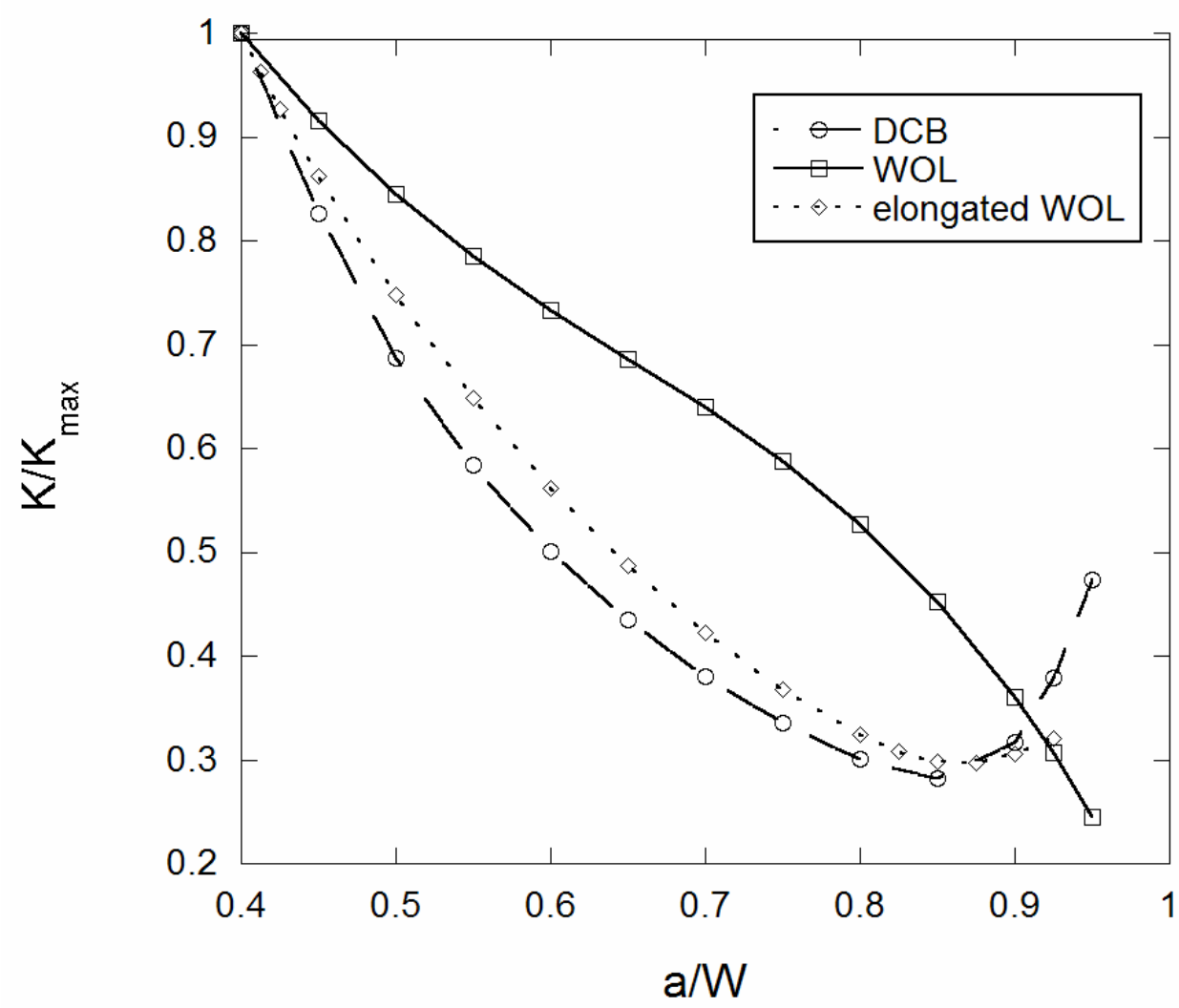

Figure C6 The relationship between K and crack length for the elongated and tapered WOL specimen compared with the standard WOL and DCB geometries. Similar to the DCB, a larger decrease in K is possible in the elongated WOL relative to the standard WOL for crack lengths which remain shorter than a/W=0.85.

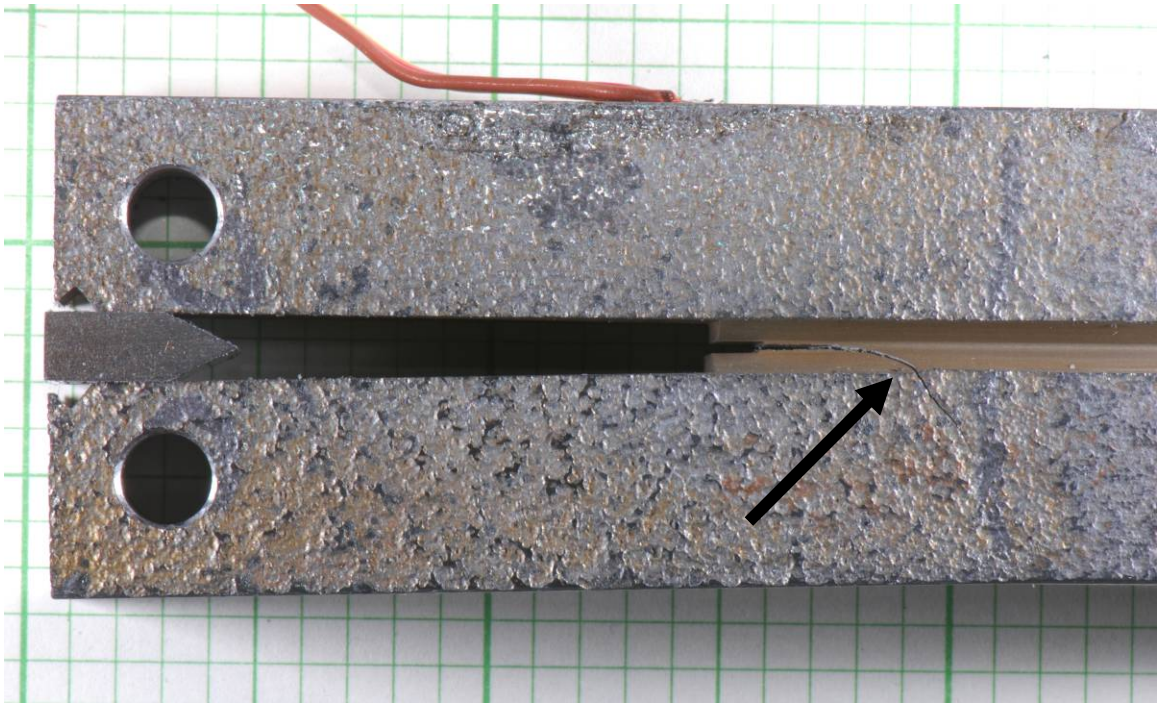

Figure C7 This photograph shows the deflected crack in a DOT-3T DCB specimen after exposure to 103 MPa hydrogen.

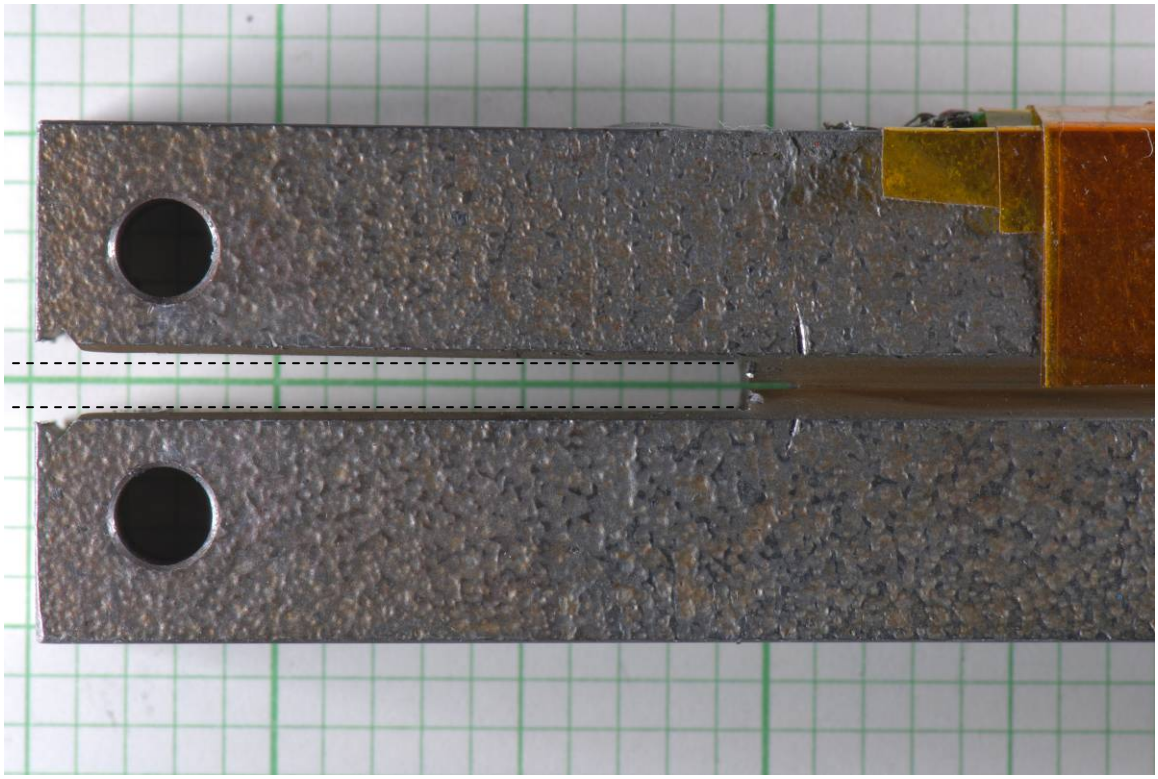

Figure C8 Residual deformation can be seen in the DOT-3AAX DCB specimen after removal of the loading wedge. No crack extension occurred after exposure to 103 MPa hydrogen.

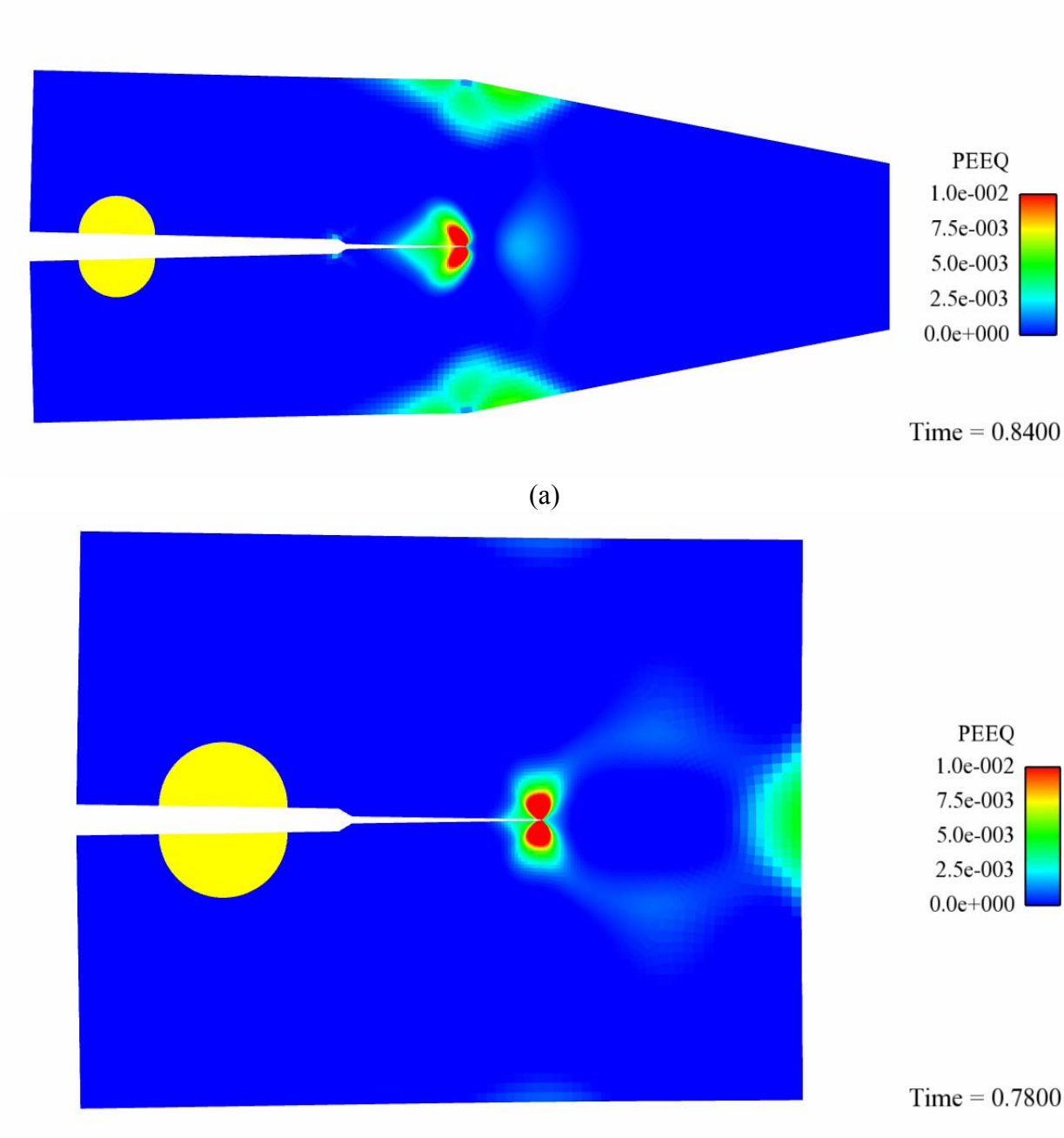

Figure C9 Elastic-plastic FEM analysis using material properties of the DOT-3AAX (641 MPa) reveal plastic strains on the top surface of the specimen at the point where the taper begins and demonstrates the limits of the elongated, tapered specimen geometry (a). Higher yield strength material and/or smaller applied displacements may allow this specimen geometry to function properly. The standard WOL, loaded to similar values of K_{app} does not experience plastic strain on the top surface (b).

DISTRIBUTION

1	MS0899	Technical Library	9536 (electronic copy)


Sandia National Laboratories